The Effect of Polycations on the Formation of Magnetite Nanoparticles

vorgelegte Dissertation
zur Erlangung des akademischen Grades
"doctor rerum naturalium"
(Dr. rer. nat.)
In der Wissenschaftsdisziplin "Physikalische Chemie"

eingereicht an der
Mathematisch-Naturwissenschaftlichen Fakultät
Institut für Chemie
der Universität Potsdam

von

Lucas Kuhrts

Potsdam, den 02.10.2019

Vorsitzender Prüfungskommission: Prof. Dr. Andreas Taubert
Mitglied Prüfungskommission: PD Dr. Damien Faivre
Mitglied Prüfungskommission: Prof. Dr. Ilko Bald
1. Gutachter: Prof. Dr. Dr.h.c. Peter Fratzl
2. Gutachter: Dr. Sylvain Prévost
3. Gutachter: Prof. Dr. Liane Benning

Tag der wissenschaftlichen Aussprache:

Acknowledgements

I want to thank Dr. Damien Faivre and Prof. Dr. Peter Fratzl for giving me the chance to work in the inspiring environment that the Department of Biomaterials at the Max Planck Institute provides. I have enjoyed and grown on the freedom to conduct my research, while always finding a person to discuss ideas critically.

Not only for his support during my thesis but for his consistent willingness to teach me new things in the past and hopefully in the future, I want to thank Dr. Sylvain Prévost sincerely.

I want also to thank Prof. Dr. Liane Benning, who agreed to be a reviewer of this manuscript.

A large part of this thesis is based on a SAXS beamtime at ESRF's ID02 instrument. This experiment was only possible with the great support of Dr. Peter Boesecke and Jacques Gorini and, of course, through the tireless maintenance of ID02 through Dr. Theyencheri Narayanan. Further, I want to thank all scientist working at the PSCM. Thanks to Dr. Jens Baumgartner, Dr. Mathias Egglseder and Dr. Sylvain Prévost for the support and the fun times we had during the beamtime.

For great scientific discussion, I want to thank Dr. Emanuel Schneck and Dr. Ernesto Scoppola. For his time for consultation and his ability to motivate and reignite scientific creativity, I genuinely thank Dr. Daniel Chevrier.

For their help on the electron microscope and their drive to focus my research, I want to thank Dr. Nadezda Tarakina and Dr. Elena Macías-Sánches and Dr. Tobias Heil for exciting discussions concerning the fine details of electron microscopy. Thank you Rona Pitschke and Heike Runge for the introduction to the old TEM.

Traveling to Veszprém, I had the chance to work with the people from the Nanolab. I want to express my sincere gratitude for the warm welcome and for the time they spent with me to Prof. Dr. Mihály Pósfai, Péter Pekker, and Zsombor Molnár. I hope to get the chance to visit again.

Special thanks to my great colleagues and friends Nils Horbelt, Friedrich Reppe, Oliver Späker, Dr. Franziska Jehle and Charlett Wenig and all the other biomaterialists for making Golm a place worth traveling to.

A huge thanks goes to all of my friends! You have equally given and taken the strength of going to work on Mondays!

For their love and support I thank Prune and my parents. Thank you!

Abstract

Nanoparticles of magnetite (Fe3O4) are envisioned to find used in diverse applications, ranging from magnetic data storage, inks, ferrofluids as well as in magnetic resonance imaging, drug delivery, and hyperthermia cancer treatment. Their magnetic properties strongly depend on their size and morphology, two properties that can be synthetically controlled. Achieving appropriate control under soft chemical conditions has so far remained a challenging endeavor. One proven way of exerting this desired control has been using a biomimetic approach that emulates the proteome of magnetotactic bacteria by adding poly-L-arginine in the co- precipitation of ferrous and ferric chloride. The objective of the work presented here is to understand the impact of this polycation on the formation mechanism of magnetite and, through rational design, to enhance the control we can exert on magnetite nanoparticle size and morphology. We developed a SAXS setup to temporally and structurally resolve the formation of magnetite in the presence of poly-L-arginine in situ. Using analytical scattering models, we were able to separate the scattering contribution of a low-density 5 nm iron structure from the contribution of the growing nanoparticles. We identified that the low-density iron structure is a metastable precursor to the magnetite particles and that it is electrostatically stabilized by poly-L-arginine. In a process analogous to biomineralization, the presence of the charged macromolecule thus shifts the reaction mechanism from a thermodynamically controlled one to a kinetically controlled one. We identify this shift in reactions mechanism as the cornerstone of the proposed mechanism and as the crucial step in the paradigm of this extraordinary nanoparticle morphology and size control. Based on SAXS data, theoretical considerations suggest that an observed morphological transition between spherical, solid, and sub-structured mesocrystalline magnetite nanoparticles is induced through a pH-driven change in the wettability of the nanoparticle surface. With these results, we further demonstrate that SAXS can be an invaluable tool for investigating nanoparticle formation.

We were able to change particle morphology from spherically solid particles to sub-structured mesocrystals merely by changing the precipitation pH. Improving the synthesis sustainability by substituting poly-L-arginine with renewable, polysaccharide-based polycations produced at the metric-ton scale, we demonstrated that the ability to alter the reaction mechanism of magnetite can be generically attributed to the presence of polycations. Through meticulous analysis and the understanding of the formation mechanism, we were able to exert precise control over particle size and morphology, by adapting crucial synthesis parameters. We were thus able to grow mesocrystals up to 200 nm and solid nanocrystals of 100 nm by adding virtually any strong polycation. We further found a way to produce stable single domain magnetite at only slightly increased alkalinity, as magnetotactic bacteria do it.

Thus through the understanding of the biological system, the consecutive biomimetic synthesis of magnetite and the following understanding of the mechanism involved in the *in vitro* synthesis, we managed to improve the synthetic control over the co-precipitation of magnetite, coming close biomineralization of magnetite in magnetotactic bacteria. Polyanions, in both natural as well as in synthetic systems, have been in the spotlight of recent research, yet our work shows the pivotal influence polycations have on the nucleation of magnetite. This work will contribute significantly to our ability to tailor magnetite nanoparticle size and morphology; in addition, we presume it will provide us with a model system for studying biomineralization of magnetite in vitro, putting the spotlight on the important influence of polycations, which have not had the scientific attention they deserve.

Contents

Chapter 1

Introduction

Nanoscience focuses on the manipulation of matter on atomic length scales to impart materials with characteristics and properties that exceed those of the corresponding bulk materials, as well as those of the single atoms or molecules. Due to the inherently strong size-property relation, the control over sizes has a pivotal impact on the applicability of these nanostructures. Nanoparticles of magnetite (Fe_3O_4), a ferrimagnetic iron oxide with an inverse spinel structure and one of the naturally most abundant magnetic materials, may find applications ranging from water purification agents[1] for phosphate removal[2], magnetic data storage[3], catalyst recovery[4–6] and as ferrofluids[7,8]. It is, moreover, foreseen to be used in medical applications, including hyperthermia cancer treatment[9,10], as MRI contrast agent[11,12] and for targeted drug delivery.[13–15]

Confined to nanoscopic sizes magnetite can exist in a superparamagnetic state below a particle size of ≈20 nm[16,17], above which it attains a permanent magnetic dipole, rendering the material a stable single domain ferrimagnet due to the anti-parallel alignments of the unequal atomic magnetic moments of Fe^{2+} and Fe^{3+}[18]. Above a size of 80 nm magnetic domains start to form to counteract an increasing magnetostatic force.[19] Research strives to improve synthesis conditions to improve control over size, size distribution, and morphology to tailor magnetite's properties to the desired applications. However, a majority of the synthesis protocols that have successfully achieved this goal rely on elevated temperature, high pressure or organic solvents including hydrothermal co-precipitation[20–22], reductive[23,24] or oxidative process[25,26] and magnetite nanoparticles prepared in oil/water-emulsion nano-reactors[27,28]. More exotic synthesis routes relying on the formation of oxidizing species, include sonochemical[29–31], γ-ray[32] and microwave-assisted[33,34] processes. The most successful route to control size and size distribution is based on the thermal decomposition of iron-containing organic complexes.[35–37]

1.1 Tools to Control Nanoparticle Size

Classical nucleation theory supplies us with tools to control nanoparticle size through the manipulation of free energy barriers of phase separation as well as through the control of thermodynamic equilibrium via the alteration of surface properties of a newly formed phase.

The formation of such a new phase is realized through the stochastic association of atoms or molecules via thermally driven density fluctuations. These fluctuations are structurally comparable to a solute and can either grow via the accretion of atoms (or molecules) to form stable seeds or dissolve through the detachment of such. The underlying thermodynamics of this process thus determines the fate of seeds and the free energy of the seeds under isothermic and isobaric conditions is governed by the difference in the chemical potential, $\Delta\mu$, of the separated phase and its surroundings, which can be quantified by the product of the thermal energy and the supersaturation, S.

$$\Delta\mu = -k_B T \ln S \tag{1.1.1}$$

k_B is the Boltzmann constant and T the absolute temperature. The supersaturation is the dimensionless ratio of the activities of species, a_i, in solution and its equilibrium molar concentration with respect to the dissolution of its solid counterpart, $a_{i,sp}$, known as the solubility product, $\mathrm{K_S}$,

$$S = \frac{\prod_i a_i^{\nu_i}}{\prod_i a_{i,sp}^{\nu_i}} = \frac{\prod_i a_i^{\nu_i}}{\prod_i K_{S,i}} \tag{1.1.2}$$

where ν_i are the respective stoichiometric coefficients. For a just saturated solution we find a supersaturation of one. With the accretion of an atom to an i-mer i+1 we find a gain in bulk free energy, $\Delta G_{bulk}(i)$, of the newly formed phase equal to the product of the change in chemical potential of the newly formed i+1-mer and the change in surface with the $\mathrm{i^{th}}$ atom added.

$$\Delta G(i) = \Delta\mu(i) + \gamma\delta A(i) \tag{1.1.3}$$

While the bulk free energy drives nucleation and thus the formation of a new phase, the inherent increase in surface, δA, and the respective increase in the interfacial energy, $\delta A(i)\gamma$ counteracts the formation of a new phase. We can thus define the total free energy of the nucleation process as the sum of nucleation driving negative volume contribution, $V\Delta G_{bulk}$ and a nucleation antagonizing work required to form a new interface, $A\gamma$. Approximating the growing seed particles as homogeneous spheres the energetic balance between surface and volume contribution can be written as:

$$\Delta G = \frac{4}{3}\pi R^3 \Delta G_{bulk} + 4\pi r^2 \gamma \tag{1.1.4}$$

While the work of the formation of a new interface is proportional to the square of the radius

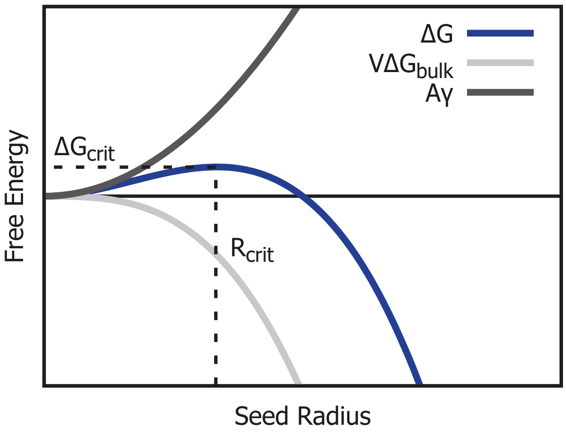

Figure 1.1: Free energy of a nucleus a function particle size as predicted by classical nucleation theory.

of the particle, the gain in free bulk energy increases with the volume of the particle and thus by the cube of its radius. The total free energy of nucleation thus has a local maximum, the activation barrier, at $\Delta G_{crit} = 16/3\pi\gamma^3\Delta G_{bulk}^{-2}$ and a corresponding critical radius, R$_c$, of the density fluctuation after which it is rendered to be thermodynamically stable at $R_c = -2\gamma/\Delta G_{bulk}$. Referencing Equation (1.1.1) and Equation (1.1.3) we find a proportionality between the free energy and a change in chemical potential and thus an anti proportionality between the supersaturation and the critical energy barrier,ΔG_{crit}. The dependence of the free energy and the corresponding volume and surface terms is schematically shown in Figure 1.1.

Thus one option to exert size control is to induce an extreme supersaturation, to separate the nucleation event from the growth event.[38,39] Another frequently used tool is the use of additives that, through adsorption to the nanoparticle/solvent interface, alter the surface energy. Through preferential adsorption to certain crystal facets, the addition of surface-active molecules is a widely used tool to produce different particle morphologies or anisotropic nanoparticles.[40–43] Further, acidic, polyanionic macromolecules like polyacrylic acid[44–46] or polyaspartic acid[47] have been heavily used to alter magnetite nanoparticle properties.

1.2 Biomineralization

Control beyond thermodynamically controlled accretion of ions from solution is the key to produce more sophisticated and complex crystals. A distinctive example is the formation of mineralized material in living systems, called biomineralization. Here, the mass flux for crystal formation is achieved using amorphous precursor phases that can be crystallized into virtually any shape as demonstrated in the case of coccolithophores.[48,49] Biomineralizations distinguishing characteristic is the ability of the nucleation of crystals precisely defined in morphology and shape from heterogeneous environments at ambient temperatures and pH values close to neutrality. This control is accomplished by nucleation via stabilized amorphous precursor phases shifting the reaction profile from a thermodynamically to a kinetically controlled pathway.[50,51]

The exertion of kinetic controlled is achieved by alteration of the activation barriers of the sequential transformation of metastable precursor phases to the final crystal as it is suggested in Figure 1.2. Descending this structural cascade, we find an increase in density, while hydration, solubility, and free energy decrease. The activation energies of the corresponding solid-state transformation can be heavily influenced by the presence of ionic and/or molecular additives. This manipulation of activation energies has been demonstrated *in vivo*[52] and *in vitro*[53]. Studying and imitating biomineralization processes thus promises to establish new protocols to control nanoparticle formation.

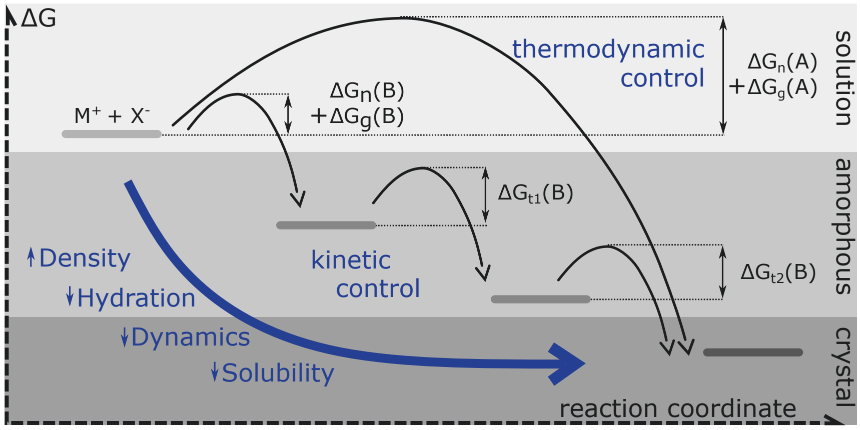

Figure 1.2: The cascade of consecutive solid phase transition predicted by the Oswald step rule. This kinetically controlled process is favored, when amorphous precursor particles, with a low solubility compared to the thermodynamically most dense phase, exist. Here $\Delta G_n(A)$ and $\Delta G_g(A)$ is the free energy for nucleation (n) and growth (g) for pathway A. Energies for pathway B are indicated accordingly. $\Delta G_t(A)$ describes the free energy solid-state phase transition.

1.3 Magnetite Biomineralization

Magnetite is biomineralized by various organisms exploiting its magnetitic and mechanical properties. For magnetoreception purposes it us used by salmon[50], honeybees[54,55], migratory birds like homeing pigeons[55,56]. Chitons, a marine mollusks, use it for its high hardness as mechanical reinforcement and even in the human brain biomineralized magnetite has been reported to exist.[57] However, the most abundant biomineralized magnetite is found in terrestrial magnetotactic bacteria[58], that biomineralize large magnetite nanoparticles with a remanent magnetic dipole in discrete vesicles -called magnetosomes- functioning as small biomineralization reactors. To study the biomineralization of magnetite in more detail, Baumgartner et al.[59] inferred the evolution of iron phases involved in the nucleation process from cryo XANES measurements on iron-depleted *Magnetosperillum Magnetotacticum* (MS-1). They found that magnetite is formed via a phosphate-rich ferric hydroxide, consistent with prokaryotic ferritins, that are thought to have a ferrihydrite core[60], and consecutively via nanometric ferric(oxyhydr)oxide. This pathway is consistent with non-classical sequential nucleation mechanism via amorphous intermediates, as proposed above. Congruently others have identified acidic macromolecules to be involved in the biomineralization of magnetite.[61,62]

1.3.1 Magnetite Biomimetics

For size-controlled synthesis under mild physico-chemical conditions, it is desirable to elucidate the magnetotactic bacteria's ability to produce discrete, stable single-domain magnetite particles with remarkable control over size and morphology under mild chemical conditions (only slightly increased alkalinity) at ambient temperature and pressure.

in vitro synthesis of magnetite in the presence of magnetosome membrane specific (Mms) proteins has been used to control magnetite nanoparticle morphologies[63,64]. A more abstract approach trying to infer generic motives from these proteins and apply them in a biomimetic synthesis of magnetite was done by Baumgartner et al.

They used a phage display, exposing 2.7 x 10^9 random permutation of a 12-mer peptide sequence to a nanocrystalline magnetite powder. Sequences that bound to the magnetite surface were presumed to potentially interact in the nucleation of magnetite. A general design principle drawn from this experiment was that majorly positively charged proteins would promote, and mainly negatively charged proteins would inhibit magnetite nucleation. Encouraged by these results, Baumgartner et al. used a positively charged polypeptide with a remarkably high isoelectric point, poly-L-arginine, in a co-precipitation reaction of ferrous and ferric chloride.

Electron microscopy images of the resulting magnetite nanoparticles, which will be in the focus of this work, are shown in Figure 1.3. Due to their size and the inherent remanent, anisotropic magnetic dipole moment, they form chains (Figure 1.3 a)). At higher magnification (Figure 1.3 b) - c)) we find that the nanoparticles are sub-structured and seem to be built up from 10 nm sized sub-unit building blocks forming the final 40 nm nanoparticle.[65] Due to their single crystal-like coherent diffraction, seen in the FFT of the inset of Figure 1.3, they were classified as mesocrystalline.[66]

Along with the single crystal-like diffraction, their magnetic properties are congruent with those of a single domain solid magnetite nanoparticle, which was confirmed in bulk magnetic measurements and even for single particles using off-axis electron holography.

However, mechanistically it is difficult to envision how preformed 10 nm sized sub-units may assemble into a coherent crystallographic register while attaining their spherical and centrosymmetric shape. The mechanism proposed by Reichel et al.[65] envisions an aggregation via oriented at-

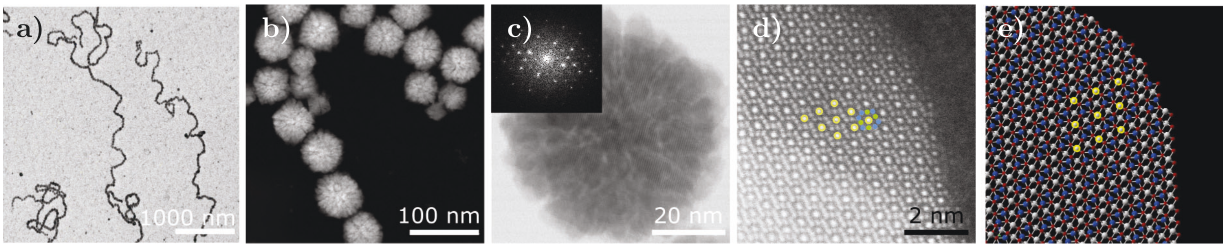

Figure 1.3: a) gives an overview of magnetite nanoparticles precipitated in the presence of poly-L-arginine at pH 11. Chain formation due to dipolar, magnetic interaction is apparent. A magnified view of the particles using HAADF STEM b) and bright field STEM c) shows the sub-structured morphology, while particles remain single crystalline, as visible in the FFT in the bottom left inset of c). Going to atomic resolution we can see the structure of magnetite along the [110] zone axis. Octahedral sites are marked in grey with the distinction of full (yellow rings) and half occupation (green spheres). Tetrahedrally coordinated iron is marked blue, in accordance to the simulated magnetite structure in e). STEM measurements were performed by Dr. Tobias Heil.

tachment driven by magnetic exchange coupling between the subunits, while poly-L-arginine would function as an electrostatic scaffold.

1.4 Objective and Scope of this Work

Baumgartner et al. have demonstrated that the understanding of magnetite biomineralization can drive the biomimetic development of novel nanoparticles. Emulating this approach, we now strive to understand the developed biomimetic system and thus the effect that poly-L-arginine has on the nucleation and growth of magnetite.
The foundation of the mechanistic understanding will be provided by the spatiotemporal investigation of structures involved in the formation of poly-L-arginine/magnetite using *in situ* small angle X-ray scattering. Applying the knowledge contained in the elucidation of this mechanism, we strive to exert even higher control on the size and morphology of magnetite nanoparticles precipitated in the presence of polycations.

- The synthesis of magnetite in the presence of poly-L-arginine requires low feeding rates of iron solution into an alkaline dilute polymer solution. Thus, the iron concentration is below 1 ppm within the first minutes of the synthesis. To unravel the formation mechanism, we rely on structural data on the early structures present in the synthesis. To analyze these structures in their native environment, it was necessary to perform measurements on a 3rd generation high brilliance synchrotron. The SAXS beamline ID02 at ESRF was, therefore, the instrument of choice. Studying by *in situ* SAXS the influence of i) the molecular weight and ii) the concentration of poly-L-arginine, iii) the impact of temperature and iv) the influence of precipitation pH on the structural evolution of particles, enables us to predict a comprehensive formation mechanism.

- The addition of poly-L-arginine in the co-precipitation of ferrous and ferric iron at pH 11 results in remarkable, mesocrystalline nanostructures. Changing synthesis parameters, we aim at exploring the feasibility to further ameliorate and alter the properties of the produced magnetite nanoparticles.
- While the synthesis setup already does not require elevated temperatures or high pressure and works in an aqueous environment, we aim to further increase its sustainability by substituting poly-L-arginine by renewable and cheaper polymers.
- Through the understanding of the formation mechanism of the underlying *in vitro* biomimetic system, we aim to develop a synthesis route to produce –similar to magnetotactic bacteria– discrete stable single domain magnetite nanoparticles at ambient conditions and only slightly elevated alkalinity.

Chapter 2

Theoretical Background

2.1 Magnetite Co-precipitation

In this work we study the effect of poly-L-arginine on the formation of magnetite. Magnetite is formed via co-precipitation of ferrous and ferric chloride in aqueous alkaline solution. The hydrolysis reaction can be expressed as:

$$2\,\mathrm{FeCl}_{3(\mathrm{aq.})} + \mathrm{FeCl}_{2(\mathrm{aq.})} + 8\,\mathrm{NaOH}_{(\mathrm{aq.})} \longrightarrow \mathrm{Fe}_3\mathrm{O}_{4(\mathrm{s})} + 4\,\mathrm{H}_2\mathrm{O} + 8\,\mathrm{NaCl}_{(\mathrm{aq.})}$$

Several mechanisms for this reaction have been proposed, including the direct formation from soluble ferrous and ferric species, via the transformation from chloride green rust or the transformation of ferrihydrite through dissolution or re-precipitation.[16,67–71]
A comprehensive study on the formation of magnetite nanoparticles produced under the same conditions as in this work was done by Baumgartner et al.[72]. They have presented an in depth analysis of the structural evolution of magnetite nanoparticles and the underlying thermodynamics of possible nucleation pathways. The kinetics of magnetite nucleation was modeled with a linear ($\alpha = 1$) reaction limited growth $R^{\alpha}(t) - R^{\alpha}_{(t=0)} = kt$ from finite size seeds, $R_{(t=0)}$, where k is the kinetic rate constant and t the time. The growth of the nanoparticles was studied as a function of pH and an inverse proportionality of the rate constant with pH was identified. This rate is proportional to the probability of a seed to grow beyond its critical radius crossing the free energy barrier ($k \propto \exp(-\Delta G_c/k_B T)$). When the pH is lowered, so is the magnetite/water surface tension due to a deprotonation induced charging of the interface. Following Equation (4.3.1) this lowering in surface tension results in a lower free energy barrier. Thus smaller seeds will be formed faster when the synthesis pH is increased. Thus, from a unit volume iron solution we will obtain more and smaller seed particles at increased pH, decreasing the radial growth rate of each individual particles,

as summarized in Figure 2.1.

This growth model was further investigated by Baumgartner et al.[72] using cryo-TEM to image the magnetite nanoparticles and the proposed precursor phases in their quasi-native state. We summarize the proposed formation steps of magnetite in absence of additives in Figure 2.2 and want to proceed with the discussion based on this scheme. The final magnetite nanoparticles d) nucleate and grow from an aggregate of 2 nm sized primary particles c). This solid state transformation to magnetite may proceed via an amorphous intermediate or directly yield the thermodynamically more stable crystalline phase. A distinction between these two pathways was made based on the free energy of the involved primary particles. For metastable primary particles, with respect to the solution, an amorphous intermediate would be expected, while no intermediate amorphous phase is foreseen when the primary particles can be considered stable. Thus, in order to evaluate the stability of the involved primary particles, Baumgartner et al. turned their attention towards the formation of the primary particles proposing that they most likely originate from a gel-like, ferrihydrite a) in accordance with previous reports.[71] The ferrihydrite phase proposed and the small size of 2 nm explain the stability of those particles. Thus no intermediate amorphous phase is thought to be present in the nucleation of magnetite from ferrous and ferric chloride at alkaline conditions.

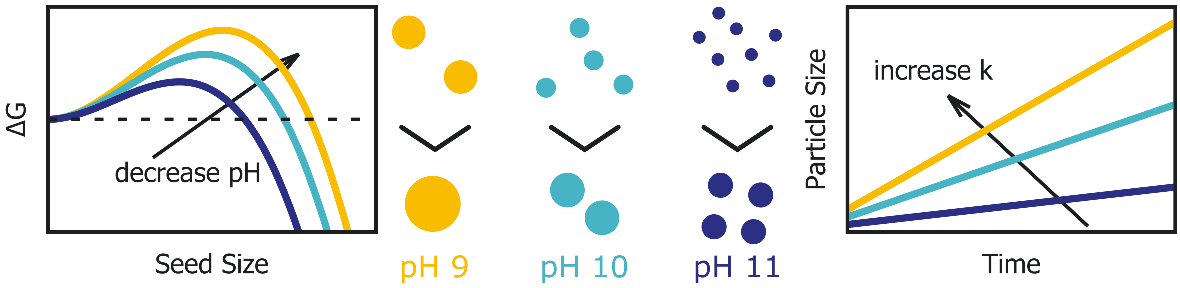

Figure 2.1: Free energy as a function of pH. With increasing pH the activation energy and the critical size for stable seeds decreases. We thus form from a unit volume iron solution more but smaller particles at higher pH. Looking at a single particle, which is supposed to grow by the consumption of other particles, a decrease in the reaction rate per time unit is suggested.

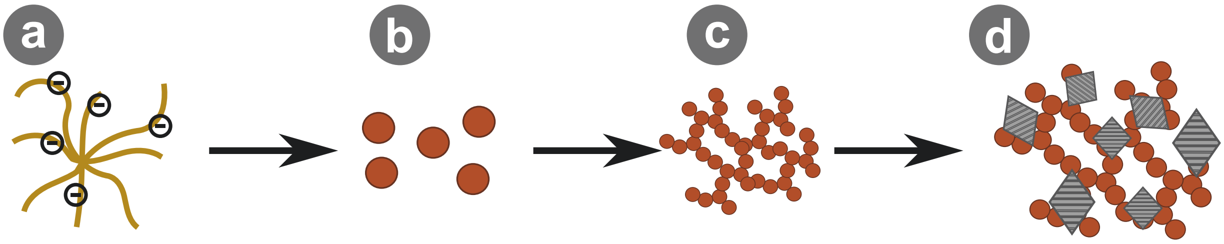

Figure 2.2: Proposed mechanism of the formation of magnetite by the co-precipitation of ferrous and ferric chloride at alkaline conditions. During the first minutes a low density fractal structure forms, which is predicted to be ferrihydrite a). From this precursor phase 2 nm primary particles b) form that aggregate to form a fractal networks with sizes above 100 nm c). From this network crystalline magnetite nucleates.

Chapter 3

Materials & Methods

3.1 Co-precipitation Setup

Magnetite was synthesized following the co-precipitation route according to established protocols.[59,67] In brief, reactions were performed in a commercially available titration setup consisting of a titration device (Metrohm AG, Titrando 888, 5 mL volumetric cylinder), coupled to a pH electrode (Metrohm Biotrode) keeping a constant pH controlled via the software interface supplied by Metrohm (Tiamo, Version 2.3). The pH electrode was calibrated regularly using commercially available buffer solutions at pH 4, 7 and 10. The iron solution was added using a dosing unit (Metrohm, Dosimat 805, 1 ml volumetric cylinder) via microloader tips (Eppendorf, Hamburg, Germany, No. 5242 956.003) that were also used as inlets for the NaOH solution. Reactions were performed in anoxic conditions under a humidified nitrogen stream in a 50 ml reaction vessel (Metrohm, No. 6.1418.110) with a thermostat jacket, which was kept at a constant temperature of 25±0.1°C using a thermostat (Lauda-Königshofen, Lauda M3). We want to emphasize here, that ensuring anoxic conditions is essential to obtain magnetite. Even at a slightly elevated oxygen partial pressure, goethite is formed. Homogenization of the reaction solution was achieved through constant stirring with a non-magnetic overhead 802 rod stirrer (No. 2.802.0020). All glassware was regularly etched and cleaned with fuming hydrochloric acid (Roth, 37 %, Rotipuran). A scheme of the experimental setup is shown in Figure 6 a).

3.1.1 Experimental

Iron solutions were prepared from ferrous and ferric chloride with a total concentration of 0.1 M at a stoichiometroic ratio of 1:2 and added at a rate of 1 $\mu\mathrm{l\,min}^{-1}$ to a 10 ml 0.1 $\mathrm{mg\,ml}^{-1}$ alkaline solution of poly-L-arginine. The solution pH was set prior to the start of the synthesis to the desired value and kept constant by addition of 0.1 mol NaOH solution.
All chemicals were used as purchased without further purification. Ferrous chloride tetrahydrate (Merck, EMSURE ACS, >99 %), ferric chloride hexahydrite (Acros Organics, >99 %) and NaOH (1 M, Merck) solutions were used for the co-precipitation of magnetite. Poly-L-arginine with an average molecular weight of 5–15 kDa (Sigma Aldrich, P4663), 15–75 kDa (Sigma Aldrich, P7762), >70 kDa (Sigma Aldrich, P3892) and 29 kDa (Alamanda Polymers, PLR150) were used as additives. Precise low molecular weight poly-L-arginine samples were ordered and synthesized on demand by PepScan with 2,4,8,16 and 32 monomer repeating units.

3.2 X-Ray Scattering

X-ray scattering is an ideal tool to study colloidal systems from micron sized particles down to atomic length scale with intrinsically high statistics as information is averaged over the whole illuminated sample volume. An incoming planar wave, resulting from a collimated, coherent X-ray beam, hits the samples. Scattering occurs due to the interaction of the electromagnetic radiation with the N electrons of an atom in the sample (Thomson scattering) so that the coherently scattered intensity, I_{coh}, by an atom can be written as

$$I_{coh} = r_e^2 \sum_1^N f_e^2(\theta, \lambda) = r_e^2 f^2(\theta, \lambda) \tag{3.2.1}$$

with r_e being the classical electron radius and $f_e(\theta, \lambda)$ the electronic scattering factor, which, summed over the number of electrons in an atom, becomes the atomic scattering factor $f(\theta, \lambda)$. The collective coherent amplitude, $F(q)$, scattered by an assembly of atoms j, with their atomic positions $\vec{R_j}$ confined by the structure of the sample, is thus defined as the sum over the product of the amplitude, $f(\theta, \lambda)$, and the relative phase shift, $e^{i\vec{q}\vec{R_j}}$, emerging from the j$^{\text{th}}$ atom:

$$F(q) = \sum_j^N f_j(\theta, \lambda) \cdot e^{i\vec{q}\vec{R_j}} \tag{3.2.2}$$

This equation suggests that the size and shape of an object, and thus the distribution of electron density, are the parameters defining the angular dependent scattering intensity, if the incident energy is sufficiently far away from an atomic absorption edge. The localization of the electron density can

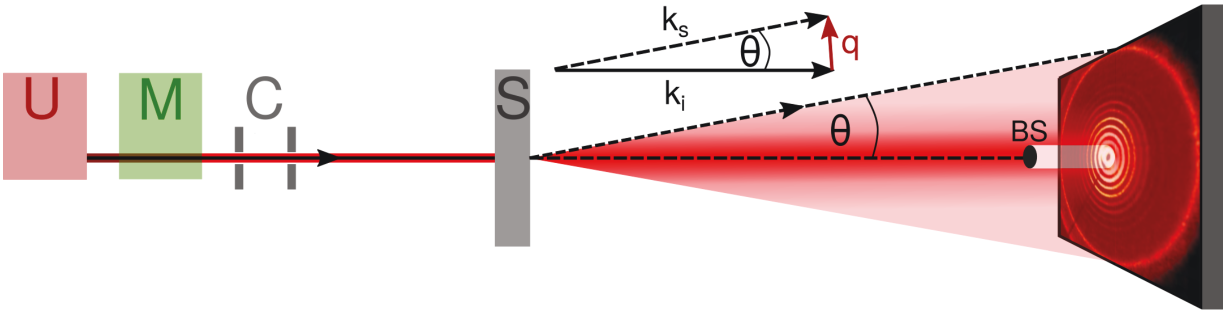

Figure 3.1: Schematic setup of a synchrotron scattering experiment. Highly brilliant X-rays are produced in the undulators (U), the energy dispersion is reduced by the monochromator (M) and beam convergence and shape controlled with adjustable scatterless slits in the collimation system (C). After impinging on the sample as $\mathrm{k_i}$ the majority of the X-rays are transmitted without interacting with the sample and absorbed by the beamstop (BS). All structural information of the sample is contained in the scattered X-ray intensity as a function of momentum transfer $\vec{q} = \vec{k_s} - \vec{k_i}$ and detected on a 2D detector (D).

be summarized in the scattering length density function $\beta(x, y, z)$ which is related to $f(\theta, \lambda)$ as an infinitesimal small volume acting as a point scatterer at a given location R:

$$f(\theta, \lambda) = \beta(R) dV \tag{3.2.3}$$

Assuming the scattering length density function to be continuous, Equation (3.2.2) thus becomes

$$I_s = |F(q)|^2 = \left| \iiint_V \beta(R) \cdot e^{iqR}\, d^3R \right|^2 \tag{3.2.4}$$

with the detected scattered intensity, $\mathrm{I_s}$, being the square of the modulus of the scattering amplitude. Mathematically the scattering detected is thus the Fourier transformation of the scattering length density function. Within the assumption that the scattering process is elastic and thus the incoming wave-vector has the same magnitude as the outgoing wave-vector ($||\vec{k_i}|| = ||\vec{k_s}|| = 2\pi/\lambda$) we can construct the momentum transfer vector, $\vec{q}$, whose magnitude $||\vec{q}||$ is proportional to the scattering angle θ (only in absence of inelastic effects) via:

$$||\vec{q}|| = ||\vec{k_s} - \vec{k_i}|| = \frac{4\pi}{\lambda} \cdot \sin(\theta) \tag{3.2.5}$$

3.2.1 X-ray Powder Diffraction (XRPD)

Crystals are long range periodic arrangements of atoms forming the crystal lattice. Confined to the atomic scaffold we have thus a periodic electron density and consequently a periodic scattering length density function. The Fourier transform of this function will only be non-zero when q lies on the reciprocal lattice, which manifests itself in the construction of the Ewald sphere. Diffraction occurs when this sphere of radius $1/\lambda$ cuts, along with the origin, a reciprocal lattice point. Prediction

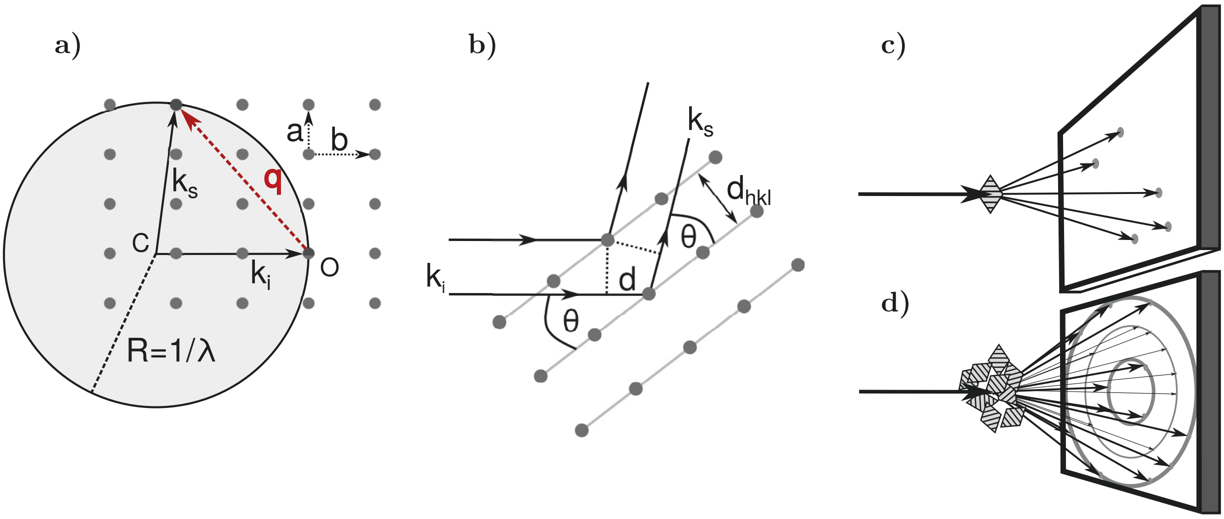

Figure 3.2: a) shows the construction of the Ewald sphere with a radius of $1/\lambda$ for constructive interference when the sphere cuts a point on the inverse crystal lattice. This relation is more intuitively understandable using Bragg's law of diffraction and the respective geometric construction b). While a single crystal, fulfilling Bragg condition will give a point diffraction pattern c), Debye-Scherrer rings are detected when the scattering arises from a powder of randomly oriented crystallites.

about crystal orientation and diffraction and thus crystal symmetry can be made based on this construction. An intuitive understanding of this has been made in Bragg's formulation of X-ray diffraction. It is a geometric derivation, seen in Figure 3.2 for the constructive interference of waves impinging at the angle θ and scattered at an angle θ from atomic planes that are spatially separated by d_{hkl}, with h, k and l being the Miller indices locating the atomic planes. If the wave's path difference $2d$ is an integer multiple, n, of the wavelength of the incident light, the Bragg condition

$$2d_{hkl}\sin(\theta) = n\lambda \tag{3.2.6}$$

for constructive interference is fulfilled. With respect to the magnitude q of the momentum transfer vector $\vec{q}$, Bragg reflections occur at

$$q = \frac{2\pi n}{d_{hkl}} \tag{3.2.7}$$

which is in turn Bragg's condition projected onto the Ewald sphere. Thus, when the Bragg condition is fulfilled, a single crystal will scatter the incoming electromagnetic radiation into discrete angles, as seen in Figure 3.2 c). When X-rays are scattered from a random assembly of a multitude of small crystals, also known as a powder, many single crystallites fulfill the Bragg condition due to their random orientation, so that a ring pattern is obtained on the detector as in Figure 3.2 d). When the intensity at the detector is azimuthally integrated the diffraction intensity as a function of scattering angle/momentum transfer with peaks at $q = 2\pi/d_{hkl}$ is obtained. As described by the

Laue equation, a decreasing particle size will result in the broadening of diffraction peak due to a reduction of the coherence volume. This peak broadening can be used to calculate crystallite sizes (L), neglecting possible strain-induced broadening of the diffraction peak and taking into account the instrumental broadening (beam convergence, wavelength spread) using the Scherrer equation[73,74]:

$$B(2\theta) = \frac{K\lambda}{L\cos(\theta)} \tag{3.2.8}$$

with the peak broadening in 2θ, B, and the Scherrer constant K, which we set to 0.9, typical for crystal systems with cubic symmetry and spherical shape.

3.2.2 Experimental XRPD

Magnetite particles were studied using synchrotron X-ray diffraction (XRD) at the μ-spot beamline at BESSY II in Berlin.[75] For the sample preparation aliquots of 1 mL were taken right after the synthesis and centrifuged for 10 min at 10 000 rpm. The centrifuged particles were re-dispersed in 5 µL of Milli-Q water and dried on Kapton film (Breitlander GmbH) clamped into a custom made brass sample holder.[76] The incident X-ray energy was set to 15 keV (λ=0.82656 Å) by a Si(111) double crystal monochromator and a spot size of 100 µm was chosen using a pin hole collimation. Diffractograms were acquired using an EigerX 9 M (Dectris Ltd.) with 75x75 μm^2 pixel size. Data reduction was performed using DPDAK[77] including determination of detector tilt and sample to detector distance using a standard sample of α Quarz (NIST). Instrumental peak broadening has been incorporated into DPDAK and calculated considering beam divergence and shape, monochromator dependent wavelength spread as well as the detectors point spread function. Background subtraction of empty Kapton was performed in 2D prior to azimuthal integration.

3.2.3 Small Angle X-ray Scattering (SAXS)

Equation (3.2.4) indicates that the scattered intensity as a function of scattering angle is proportional to the Fourier transform of the scattering length density distribution function $\beta(\lambda\theta)$ of an assembly of scatterers. One of the most fundamental properties of the Fourier transform is the reverse relationship between length scales in real and reciprocal space. Thus, for an object with three dimensions d_x, d_y, d_z the Fourier transform will exhibit minima at $q_x \approx 2\pi/d_x, q_y \approx 2\pi/d_y, q_z \approx 2\pi/d_z$. There is thus an inverse relationship between the momentum transfer vector, q, defined in 3.2.7 and the dimensionality of the investigated object. Investigation of larger objects, that can extend into the micrometer range, thus benefit from long flight paths post sample to resolve small scattering angles. Small angle X-ray scattering is thus an ideal tool to study large objects with a low structural resolution.[78]

3.2.4 Differential Scattering Cross Section and Absolute Scale

In an ideal SAXS experiment the measured intensity as a function of scattering angle should quantify the purely elastic interaction of the incoming beam with the sample. This quantity contains all relevant structural information of the sample and is known as the differential coherent elastic scattering cross-section $d\sigma/d\Omega$. Given an incident number of photons, N_i, of which a fraction N_s is scattered as defined by the vector k_s and detected at the detector by a finite size pixel covering a solid angle $\Delta\Omega$, the number of detected photons is given by:

$$N_s = N_i T \frac{\epsilon}{V} \frac{d\sigma}{d\Omega} k_s \Delta\Omega \tag{3.2.9}$$

Taking into account the transmission, T, and correcting for detectors defects such as non-linearity, the differential scattering cross–section normalized by the scattering volume, V, is equal to the ratio of scattered and incoming photons. This results in the differential scattering cross section per unit volume, which quantifies the scattering probability within the sample in units of inverse lengths:

$$I_s = \frac{1}{V} \frac{d\sigma}{d\Omega} = \frac{d\Sigma}{d\Omega} \tag{3.2.10}$$

3.2.5 Analytical SAXS Model

For simplicity, let us consider N non-interacting particles, that do not correlate spatially. The scattering arising from these particles contained in a unit volume, only depends on the particles morphology, size and scattering contrast. The angle dependent scattering intensity of the ensemble of these particles can thus be described as the product of the particles form factor, P(q), and the number density,Φ, of the particles.

$$I(q) = \Phi P(q) \tag{3.2.11}$$

The number density is simply the number of particles per total volume, from which the scattering arises. The scattering detected is the square of the modulus of the form factor amplitude, which we introduced in Equation (3.2.4) in Section 3.2. Thus the scattering intensity is the square of the modulus of the Fourier transform of the scattering length density distribution functions (SLD(r)):

$$I(q) = \Phi P(q) = \Phi |F(q)|^2 = \left| \iiint_V SLD(R) \cdot e^{iqR} d^3R \right|^2 \tag{3.2.12}$$

For different species j of scattering particles that do not correlate in space the form factor intensities are purely additive

$$I(q) = \sum_{1}^{j} \Phi_j P_j(q) \tag{3.2.13}$$

In the case of high dilution the approximation of non-correlation indeed holds and the scattering contribution of each species can thus be easily separated. This is an integral part in the analysis of the presented data, as two scattering contributions are expected based on the mechanism of the formation of magnetite in absence of additives. Growing magnetite particles, however, after crossing the stable single domain size threshold the magnetite particles retain an magnetic dipole, so that assumption of no particle interaction does not hold anymore. A spacial correlation needs to be taken into account using a structure factor S(q) between the magnetic particles $\mathrm{P(q)_m}$, not neglecting the non-magnetic particles, P(q)

$$I(q) = \Phi_m P_m(q) \cdot S(q) + \Phi_{nm} P_{nm} \tag{3.2.14}$$

3.2.6 Experimental SAXS

In situ SAXS was measured at the high brilliance beamline ID02[79] at ESRF – The European Synchrotron. For SAXS experiments the X–ray energy was set to 12.5 keV where the highest photon flux is obtained. The detector was always chosen as the CCD Rayonix MX-170HS, which offers the largest solid angle from all 3 detectors available on the beamline. Three different sample-to-detector distances were used (1 m, 6 m and 30 m). With this setup a q–range of $2{\cdot}10^{-3}$ $\mathrm{nm^{-1}}$ to 5 $\mathrm{nm^{-1}}$ was covered. For the *in situ* measurements of particle formation the synthesis setup, described in 3.1, was transported to the beamline. A 1 mm diameter glass tube was used as an intake pipe that was connected using Teflon tubing (inner diameter 1 mm) via a quarz capillary of exactly 2.0 mm inner diameter (Hildenberg open quartz capillaries, 50 μm wall thickness) using a step motor peristaltic pump (WMC). The dead volume between the beginning of the glass tubing and the end of the quartz capillary was calculated to be 70 µL. To be sure that old sample was sufficiently removed from the quartz capillary 80 µL of aliquot was taken from the reaction with different time intervals (20 times every 30 s, 20 times every 60 s, 20 times every 300 s). Absolute intensity was calculated from capillary subtracted water scattering. The measured water scattering intensity was divided by the theoretically expected scattering level, obtained from water's isothermal compressibility. To obtain absolute intensity, this correction factor was applied to all SAXS curves. The first file of each dataset was used as background and subtracted from all consecutive frames. 4 days of beamtime were awarded with the experiment ID ma3787. Images and a scheme of the setup at the beamline are in the Appendix Figure 6.

3.3 Electron Microscopy

3.3.1 Transmission Electron Microscopy (TEM)

The wavelength, λ, of electrons is bound to their momentum, p, by the de Broglie relation,

$$\lambda = h/p = h/m_e v \tag{3.3.1}$$

with the electron mass $\mathrm{m_e}$, the velocity v and the Planck constant h. Being emitted from a hot filament or a field emission gun the electrons wavelength can thus be easily set by accelerating the electron within a potential field that can be reach up to several hundred kV giving the electron a potential energy (E_v) of:

$$E_v = \frac{m_e v^2}{2} \tag{3.3.2}$$

The strength of the potential drop is determined by the accelerating voltage of the TEM, which thus determines directly the wavelength of the electron.

$$\lambda = \frac{h}{\sqrt{(2 m_e E_v)}} \tag{3.3.3}$$

Neglecting relativistic effects, the wavelength of an electron can thus be reduced to the picometer range. Aberrations in the electrostatic and magnetic lenses, however limit the effective resolution in conventional TEMs to Ångströms.[80]

To obtain TEM micrographs, the sample is illuminated with a spread, parallel electron beam and images are obtained post transmission of the specimen. Contrast arises due the difference of electron density in the image plane through scattering of the incident electron wave within the sample resulting in a change of amplitude and phase of the scattered electron wave. There is thus a fundamental distinction between *amplitude* and *phase contrast*, which generally both contribute to the contrast in the formed image. Amplitude contrast is induced through absorption or scattering of the incident electron wave in the electric field of the atoms and is proportional to the mass and thickness of the specimen. Another mechanism for amplitude contrast is the coherent diffraction of electrons by crystalline materials into angles that fulfill the Bragg condition, which are excluded from image formation by the objective aperture in the back focal plane. Selecting a diffracted or the direct beam with this aperture lets us thus select pure bright field or dark field images respectively. Phase contrast arises in the image plane due to the interference of at least two electron "beams", that have undergone a potential field induced phase shift passing through the sample. It it especially prevalent in high resolution (HR)TEM and is strongly sensitive to the thickness, orientation and atomic scattering factor within the specimen.

3.3.2 Scanning Transmission Electron Microscopy (STEM)

Making use of the inherent connection between contrast and scattering angle, only electrons that are scattered at a certain angle are used in the image formation in STEM. Here, the sample is scanned with a strongly focused and thus heavily convergent electron beam, which is transmitted and detected by single pixel, annular detectors post specimen. The resolution of the image is therefore determined by the spot size of the electron beam (0.005–0.2 nm) and the size and number of pixels of the scanned area. The image is formed from the intensity in each pixel, which is proportional to the number of electrons scattered into a certain angle onto the annular detector.

So called high angle annular dark-field (HAADF) STEM only uses electrons that were forward scattered at high angles, and in the limit of uniform thickness of the sample, the contrast is proportional to the atomic number (z-contrast). As a result high thickness and high atomic number regions appear bright, while low thickness, low atomic number regions remain dark in the final image.

There is a number of advantages that come with this technique compared to conventional TEM. A post signal processing is digitally possible so that black levels and detector gain can be adjusted during image acquisition. Due to the inherent spatial resolution that comes with the scanning mode, elemental information can be obtained. This can be done ante-transmission using energy dispersive x-rays that are emitted from the sample (EDX) or post transmission using electron energy loss spectroscopy (EELS) that can even be used to obtain magnetic information of the specimen (EMCD). Due to the exclusion of any phase contrast, STEM can be used to obtain high resolution electron tomography images. This would not be possible in normal TEM, as, due to phase contrast, the contrast of a crystal would change with tilt angle.

3.3.3 STEM Tomography

STEM tomography can be used to obtain a three dimensional reconstruction of the particle under investigation. Here, the particle is viewed from different directions in a single tilt series. From the images taken at different angles a volume rendered structure of a particle can be obtained. Due to the construction of a TEM and the fact that at angles larger than 75° parts of the TEM grid often are in the electron beam path, tomographic tilt series in TEM are limited to angles ±75°. A 180° tilt series that would be necessary for an ideal reconstruction can thus not be obtained, which can introduce artifacts in the particle reconstruction.

3.3.4 Experimental TEM

To observe particles in TEM an aliquot of 1 ml was taken right after the synthesis, centrifuged for 10 min at 10k rpm and re-dispersed in Milli-Q water of appropriate pH. 5 µL of the re-dispersed particles were adsorbed from aqueous suspension for 15 min onto 300 mesh copper grids covered with a lacey carbon supported graphene layer. Residual solution was removed using a Kimwipe and the grids dried under nitrogen for at least 30 min prior to imaging. Overview TEM micrographs to calculate particle size distributions were recorded on a Zeiss EM 912 with Omega filter and an acceleration voltage of 120 kV. Electron were produced from a LaB_6 hot cathode at a current of 7 µA. HRTEM images were recorded on a spherical aberration corrected JEOL ARM 2100 equipped with a field emission gun (FEG) at acceleration voltages of 200 kV and 15 µA beam current. STEM and STEM tomography images were recorded on a FEI Talos equipped with a LaB_6 electron gun. Electrons were accelerated in a 200 kV potential field at a current of 10 µA.

Tomography tilt series on mesocrystals were recorded between 65° and -62° in increments of 1°. Focus and drift corrections were applied manually. 3D rendered reconstructions were obtained using the Fiji plug-in TomoJ using the Simultaneous Iterative Reconstruction Technique (SIRT) algorithm.

3.4 Vibrating Sample Magnetometry (VSM)

At nanoscopic sizes, properties of materials can be highly size- and morphology-dependent. Thus controlling the size of these nanoparticles has a pivotal impact on tuning their properties towards desired application. In the case of magnetite, size influences the magnetic properties of the nanoparticles.

The magnetic moment of a magnetic nanoparticle is the net sum of all atomic magnetic moments, illustrated in Figure 3.3 b). This magnetic dipole moment can exhibits two stable orientations of all atomic dipoles being aligned parallel or antiparallel to the magnetic easy axis. For superparamagnetic particles above the blocking temperature these two states are separated by only a small energy barrier, so that the magnetic dipole moment flips between states (Nèel relaxation). In average over time, superparamagnetic particles are thus not magnetic in absence of an external field. The larger the particle size, the more spins have to be flipped, which requires a higher energy. Crossing the size threshold of around 20 nm for magnetite at room temperature the energy for the collective spin flip becomes too high, so that the particle retains a permanent magnetic dipole moment confined to a single stable magnetic domain. Due to the magnetic moment a charge separation is induced, accumulating on the surface of the particles, inducing a demagnetizing field. The associated energy is called the magnetostatic energy, which increases with increasing domain size. The magnetostatic energy can be halved when the magnetization is split into two anti-parallel domains. Thus, when

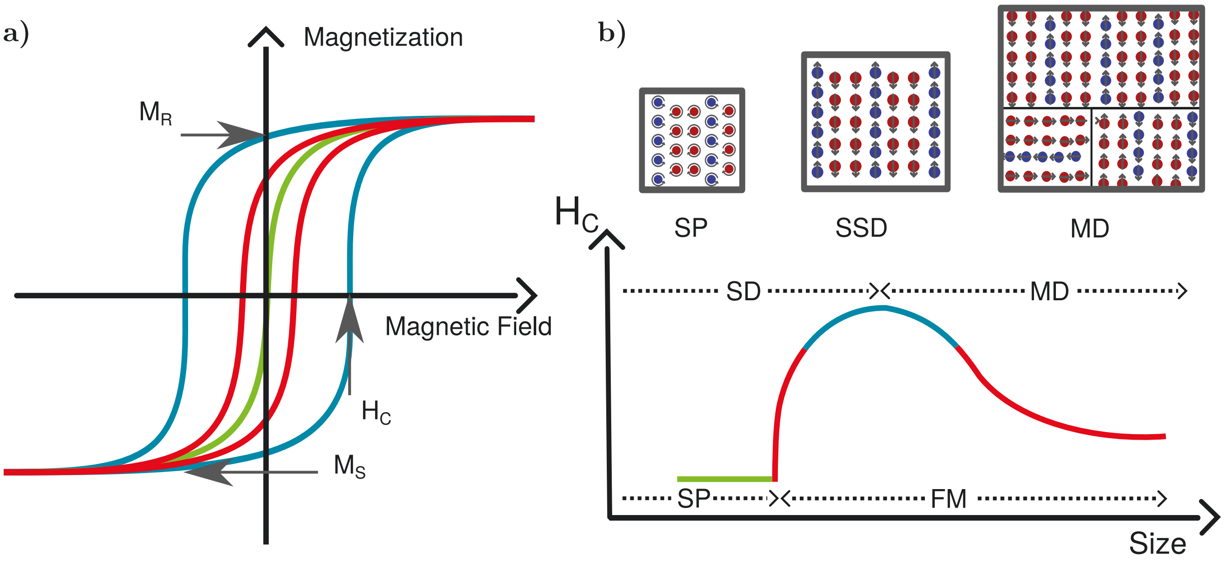

Figure 3.3: a) shows a schematic magnetic hysteresis curves that exhibit, among others, three characteristic points by which magnetic materials can be classified. The remanent magnetization at zero magnetic field (R_M), the saturation magnetization at maximum applied magnetic field (M_S) and the coercive force or coercivity (H_C) that is needed to demagnetize a prior magnetized material. b) In dependence of size magnetite exhibits three magnetic states that can be classified by their coercivity (if the temperature is above the blocking temperature and below the Curie temperature and the time of observation is longer then the Nèel relaxation time). In the superparamagnetic state (SP, green curve), where spins are in average over time aligned parallel and antiparallel to the magnetic easy axis, the material exhibits no coercivity. The maximum coercivity appears within the stable single domain (SSD, blue curve) range, while for larger particle sizes coercivity decreases as particles subdivide into multiple magnetic domains (MD, red curve).

the grain size of a SSD particle is further increased, bi-domain and further multi domain particles will form.

We use a vibrating sample magnetometer to measure the magnetization of immobilized particles as a function of applied external magnetic field as schematically shown in Figure 3.3. The external magnetic field is increased until a maximum magnetization (M_R) is reached. Here all spins are aligned parallel to the field. Incrementally reducing the field to zero, particles may maintain a magnetic moment, the so-called remanence (M_R). The field strength required to completely demagnetize the material is called the coercive force or coercivity (H_C). The coercivity of magnetite particles is an indication for the magnetic state, as indicated in Figure 3.3 b). While superparamagnetic particles show no coercivity, it is increased to a maximum for stable single domain particles, showing a relative remanence of M_R/M_S of 0.5. With further growth and subdivision into magnetic domains the coercivity decreases for multidomain particles.

3.4.1 Experimental

Hystereses loops were measured at room temperature and at a series of low temperatures using a Princeton Measurements Corporation (PMC) vibrating sample magnetometer that was outfitted with a cryostat for the low temperature measurements. Loops were determined using variable field steps over the hysteresis loop, with 0.5 mT steps in fields $< \pm100$ mT, 1 mT steps between ±100–200 mT, and 10 mT steps at fields above ±200 mT; measurement averaging time was 100 ms. Particles were concentrated with a magnet and 30 μL of solution was absorbed on a piece of cotton. Due to the low amount of particles, the weight of the sample could not be determined and the magnetic moment therefore not normalized by the samples mass. Thus, the measured strength of the magnetic moment will reflect both, composition and amount of particles.

Chapter 4

Effect of pH

Summary The co-precipitation of ferrous and ferric iron yields smaller particles when the alkalinity of the precipitation medium is increased. This effect was explained through a lowering of the oxide/water surface tension induced by the deprotonation of the surface hydroxyl groups, favoring a more strongly divided system. Adding poly-L-arginine, acting as a polycation, we show that by increasing the pH, the dimensions of magnetite increase and a single to mesocrystal morphological transformation is induced. Using synchrotron X-ray diffraction and transmission electron microscopy, we show that magnetite nanoparticles with narrow size distributions and average diameters of 10±2 nm for pH 9, 20±2 nm for pH 10, and up to 40±4 nm for pH 11 can be synthesized. We thus selectively produce superparamagnetic and stable single domain particles merely by controlling the pH as indicated by vibrating sample magnetometry. Remarkably, while an increase in pH brings about a thermodynamically driven decrease in size for magnetite without additives, this dependency on pH is inverted when poly-L-arginine is present.

4.1 Introduction

Classically, the size of magnetite in the co-precipitation of ferrous and ferric iron has been tuned by varying the pH and the ionic strength of the precipitation medium.[67,81] Following this synthesis route, particle sizes will typically range between 2 and 12 nm with a rather broad size distribution when prepared at different pH and ionic strengths. Recently, Baumgartner et al.[82] demonstrated that for a non-closed system with unlimited iron supply, crystal domains in magnetite clusters can be grown indefinitely. All of the presented systems suffer from a strong aggregation of the formed nanoparticles, which are thus not colloidally stable. With the biomimetic approach by Baumgartner[83] of introducing poly-L-arginine in the co-precipitation of magnetite it was possible to obtain colloidally stable magnetite nanoparticles with a diameter of 40 nm. Congruent to the investigations done on pure magnetite we engaged in the study of the effect of pH on the size of the nanoparticles in the presence of poly-L-arginine.

4.2 Results

The synthesis parameter were used according to 3.1 following the setup by Baumgartner et al.[83]. The precipitation pH for different synthesis was set to 9, 10, and 11 respectively. After 2 hours of the addition of iron solution an aliquot of 1 mL was taken, magnetically precipitated and washed thrice in Milli-Q water. We employ TEM and XRPD on dried aliquots to determine particle size and size distribution, structural purity of the formed iron phase. VSM was used to study the magnetic properties of the synthesized nanoparticles.

4.2.1 Size Determination Using TEM and XRPD

A qualitative impression of the synthesized particles was obtained using bright-field TEM. Representative, low magnification images of particles prepared at pH 9, 10 and 11 are given in Figure 4.1. Two main observations are evident. i) The size of the nanoparticles increases with increasing pH and ii) a morphological transition between pH 10 and pH 11 occurs from spherical, dense nanoparticles at pH 10, to a flower-like, sub-structured mesocrystal at pH 11.

We determined individual particle radii for at least 200 particles using ImageJ, to calculate intrinsic size distributions based on a normal density probability function shown in Figure 4.2. For particles obtained via co-precipitation at ambient temperature, we find comparably narrow size distributions of 10±2 nm for pH 9, 20±1.8 nm for pH 10, and 38±4.8 nm for pH 11. The HRTEM micrographs of

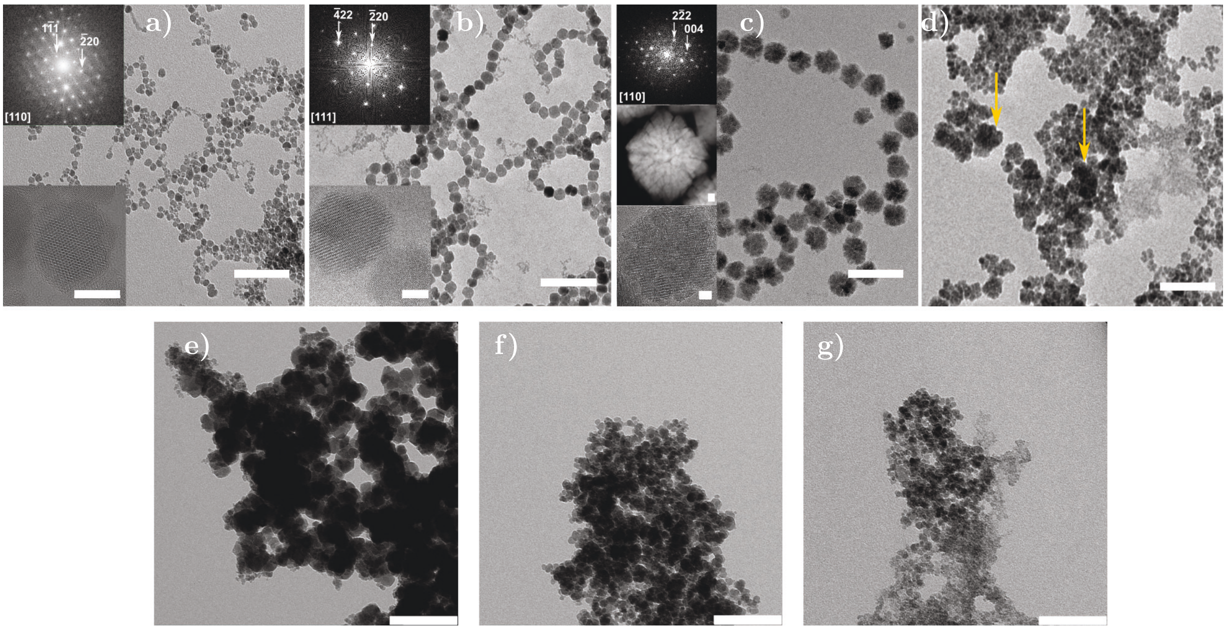

Figure 4.1: TEM micrographs of particles synthesized at pH 9, 10, 11 and 12 (top, from left to right, scale bar 100 nm) and images of particles synthesized in absence of any additives at pH 9, 10 and 11 respectively (bottom, from left to right, scale bar 100 nm). The insets (bottom) show high-resolution (HR) TEM images of one selected, single nanoparticles (scale bar 5 nm). Fast Fourier transforms (FFTs) of a single nanoparticle, shown in the top inset. Reflections have been indexed in compliance with an inverse spinel structure of magnetite. HRTEM images were recorded with the incoming beam parallel to the zone axis given as [hkl] in the FFT (bottom left of inset). The HAADF STEM image (inset, center) in (c) highlights well the mesocrystalline, sub-structured morphology of particles prepared at pH 11. While particles precipitated at pH 12 do not show a distinct particle population, few mesocrystalline appearing particles are present, as indicated by the arrows.

an individual particle in combination with FFTs revealed that all particles are single crystals with their zone axis, given in parenthesis in the FFT, aligned parallel with the incoming electron beam. The FFTs of HRTEM images of single grains were indexed, showing that the synthesized particles have an inverse spinel structure with a crystal lattice spacing of magnetite.

Concomitant with the size increase from pH 10 to pH 11 the change in morphology from single crystal to mesocrystal was observed. The sub-structured morphology is especially well visible in the HAADF STEM micrograph in the inset in Figure 4.1 c). Particles prepared at pH 12, however, did not follow this continuous increase of size with pH. TEM micrographs show agglomerates of small particles that coexist with mesocrystalline appearing nanoparticles, indicated by the yellow arrows. Excluding particles prepared at pH 12, as an unsuccessfully conducted synthesis, we will focus further characterization on particles prepared between pH 9 and 11.

Colloidal stability was confirmed visually in Figure 4.2 b) shortly after the synthesis and 3 months after storage under anoxic conditions. While magnetite nanoparticles prepared in the absence of any additive precipitated shortly after their formation, particles prepared in the presence of poly-L-arginine remained stable during the three months of observation. The morphology, size, and size distribution of the particles, as seen in particle size distribution obtained from TEM measurements in Figure 4.2, are found to remain unaltered in storage up to 7 days when kept in solution under anoxic conditions. A statistically more significant size evaluation is obtained using x-ray powder diffraction (XRPD) were an averaged signal over the whole sample population is recorded. Complementary to TEM measurements, the diffraction data showed an increase in particle size as pH increased. The azimuthally integrated full XRPD diffractogram is shown in Figure 4.3, with the inset showing a high magnification excerpt of the (311) reflection. The peak broadening of this –and any other– reflection is directly related to a decrease in particle size with decreasing precipitation pH. Nanoparticle sizes were calculated from the full width at half maximum using the Scherrer equation,[73] resulting in particle diameters ranging from 10±0.5 nm for pH 9 to 14±1 nm for pH 10 and 24±2 nm for pH 11. Standard deviations were calculated from the mean particle size of triplicates, showing a high reproducibility of the synthesis. Lattice constants for the cubic system (a=b=c) were obtained from the 311 peak position and calculated to be 8.3734 Å, 8.3741 Å and 8.3768 Å for pH 9, 10, and 11, respectively, indicating that the obtained particles are indeed magnetite which has undergone slight surface oxidation[76] resulting in a decrease of the lattice constant compared to compositionally pure magnetite (8.3965 Å). The contribution to the lattice constant of surface oxidation decreases with increasing particle size, which is also observed for magnetite prepared without any additives[82].

4.2.2 Magnetic Properties

The magnetization as the response to an externally applied magnetic field of a bulk samples of immobilized particles at room temperature was recorded on a vibrating sample magnetometer. Corresponding hysteresis loops are shown in Figure 4.4. As aliquot masses were too small to normalize the maximum magnetization, we focus on the coercivity (H_C) to discriminate between superparamagnetic and ferromagnetic particles. While superparamagnetic particles show no opening of the hysteresis loop and thus no coercivity (H_C=0), ferrimagnetic materials can be characterized by the

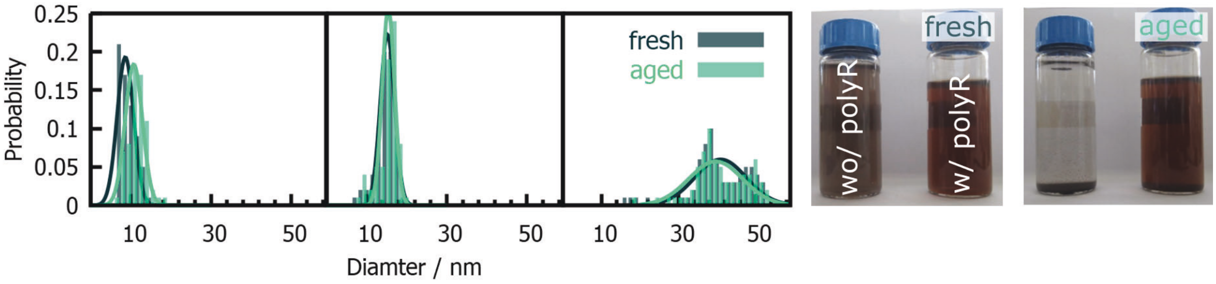

Figure 4.2: Particle size distribution measurements based on the evaluation of at least 200 nanoparticles prepared at pH 9, 10 and 11, respectively using TEM. Colloidal stability in the presence of poly-L-arginine could be confirmed visually for at least 3 months, while nanoparticles prepared in absence of any additive, precipitated shortly after the synthesis.

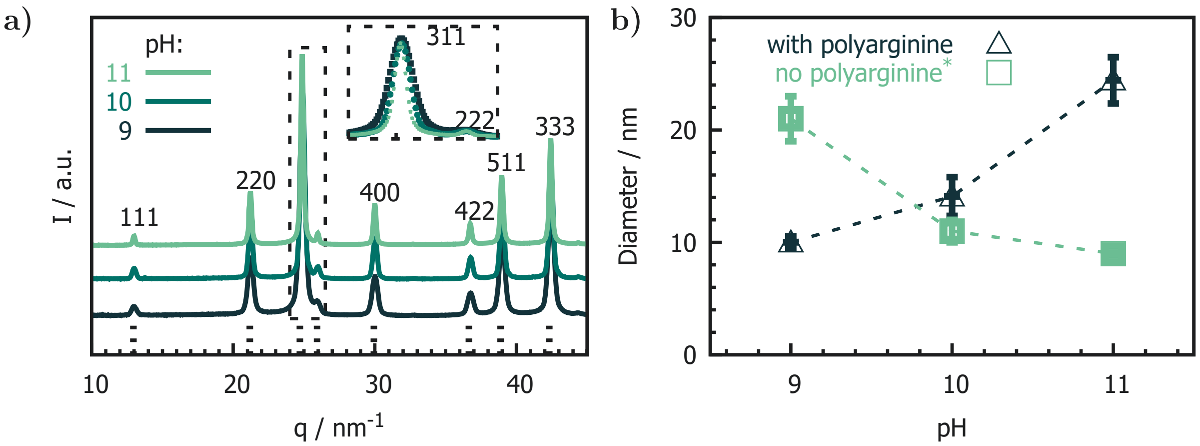

Figure 4.3: a) Azimuthally integrated XRDP measurements of particles prepared at different pH. The 311 maximum intensity reflection is shown in the inset. The broadening of the peak directly evidences the decrease in particle size with decreasing pH. From lattice parameters, calculated magnetite reflections are indicated as dotted lines and the corresponding hkl indices were attributed to each peak. Average particle sizes as obtained from the Scherrer equation are shown in b). Error bars were calculated from triplicates assuming a Gaussian distribution. Particles sizes obtained in the absence of poly-L-arginine in dependence of pH were taken from literature[72] and plotted as a reference.

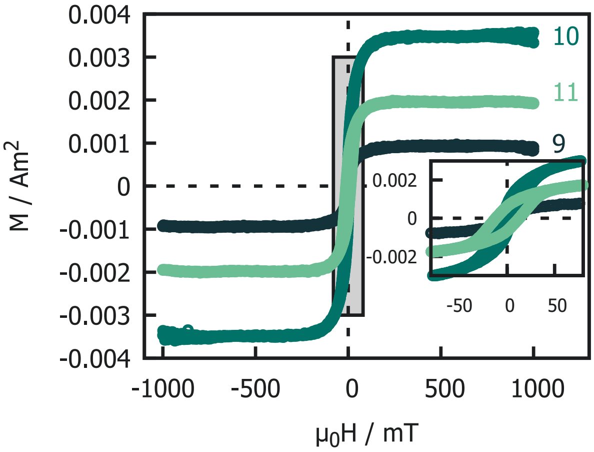

Figure 4.4: Measurement of the magnetization of immobilized particles induced by an externally applied magnetic field recorded on a vibrating sample magnetometer. The opening of the magnetic hysteresis loops for particles prepared at pH 10 and 11 are well visible in the magnified view (inset) indicative of a remanent magnetic dipole moment, which, in the case of magnetite, designates the appearance of ferrimagnetism. Particles prepared at pH 9 show no hysteresis and thus no coercivity at the given temperature and can thus be regarded as superparamagnetic. Coercivities of 6 mT and 12 mT for particles prepared at pH 10 and 11 were determined from the field strength to completely demagnetize the particles after full magnetization.

Table 4.1: Mean particles sizes at different pH analyzed by TEM (D_{TEM}) and XRPD (D_{XRPD}). Particles size distributions from TEM were calculated from single particles in an ensemble of at least 200 particles, while for XRPD mean particle sizes were calculated from mean sizes of triplicates. Vibrating sample magnetometry show the change from superparamagnetic to stable single domain behavior with the appearance of a coercive force ($\mathbf{H}_C$). The lattice parameter (**a**), increases with increasing pH. The ratio of the remanent magnetization (M_R) and the saturation magnetization (M_R) as a function of size will have a global maximum at 0.5 at the size of the largest stable single domain particle.

pH	**D_{XRPD}** [nm]	**D_{TEM}** [nm]	**H_C** [mT]	**a** [Å]	**M_R/M_S**
9	10 ± 0.5	10 ± 2	0	8.3734(1)	*
10	14 ± 1.7	20 ± 2	6	8.3740(6)	0.23
11	24 ± 2.0	38 ± 5	12	8.3767(8)	0.39

opening of the hysteresis loop (H_C>0), when a reversed magnetic field is applied. Particles prepared at pH 10 and 11 have coercivities of 6 mT and 12 mT and a M_R/M_S ratio of 0.23 and 0.39, respectively, which is congruent with a growth of the domain size of the SSD particles[84], which is also consistent with structural results from TEM and XRPD. All relevant parameters obtained from XRPD, TEM and VSM analysis of the magnetite nanoparticles prepared at different pH are summarized in Table 4.1.

4.3 Discussion

We find an obvious discrepancy between particle sizes calculated from XRPD data compared to sizes obtained from TEM measurements. For particles prepared at pH 11 XRPD underestimates the size up to 40% compared to TEM. We can identify several reasons for this. As XRPD is only sensitive to an effective volume measured in the direction of the [311] vector along which the diffraction is coherent, results may differ from TEM where the radius is calculated from a spatially averaged area projected from a three-dimensional structure. Further, thresholding during the size determination in TEM may exclude small particles, which in XRPD contribute to a significant peak broadening, lowering calculated mean sizes. Both methods, however, demonstrate an increase in particles size as pH is increased.

Even though particles are grown beyond the SSD size threshold we were able to obtain colloidally stable particles. Additionally, particles did not show any aging effects on their size or morphology. This persistence of size and morphology may suggest that the system is in thermodynamic equilibrium. However, for the change in size and morphology, considerable energetic barriers would have to be overcome for the following reasons: i) Due to the proposed adsorption of polymer, particles are electrostatically and sterically stabilized preventing coagulation.[85–87] ii) Grain coarsening by Ostwald ripening that frequently appears for dispersed systems possessing a certain solubility is prevented due to the super low solubility of magnetite in alkaline solution (K_S=10^{-8}M)[88]. The colloidal stability of the nanoparticles is favorable for prospective application. Attractive dipolar forces -which cause aggregation, especially in SSD magnetic nanoparticles- seriously compromise the usefulness of these nanoparticles in applications, such as medical ones where aggregation and sedimentation could clog blood vessels. This problem has been overcome by stabilization with a polymer. Moreover, due to a consecutive stabilization during the growth of particles, we achieved to produce colloidally stable and non aggregated SSD magnetite particles.

Most striking, however, is the fact that we find an increase in particle size with increasing pH, while magnetite in the absence of additives formed by co-precipitation in alkaline solution, shows an inverted trend. Final particle sizes increase when alkalinity is decreased. XRPD particle sizes of magnetite prepared under the same conditions but without poly-L-arginine - as described in literature[72] - are plotted in Figure 4.3 b) together with the sizes obtained in the presence of poly-L-arginine. An inversion of the pH-dependence of the nanoparticle size is evident.

For naked magnetite, the dependence of size on the surrounding pH has been derived based on the classical nucleation theory. In 1.1.4 we have recalled that the free energy of the precipitation reaction is equal a negative free energy contribution of the formation of a new volume phase, ΔG^0_{bulk}, and the inherent positive contribution of the formation of a new interface, $\Delta G^0_{surface}$ which is equal to the product of the oxide water interfacial tension, γ, and the total surface area, A, of all n_P particles, A $= 4\pi r^2 n_P$.

$$\Delta G^0_{surface} = \gamma A \tag{4.3.1}$$

This interfacial energy arises due to the difference in chemical potential, μ, of the atoms in the interfacial region and the chemical potential of the bulk phase. For a given surface area, a decrease in interfacial tension can thus induce a decrease in free energy through the adsorption of any species i at the interface, quantified by the Gibbs adsorption isotherm:

$$\Delta\gamma = -\sum_i \Gamma_i d\mu_i \tag{4.3.2}$$

The adsorption density Γ_i is given by the number of molecules of species i adsorbed per unit area $\Gamma_i = n_i/A$. Thus any kind of specific or non-specific adsorption will induce a lowering of the surface interfacial tension and reversely any desorption an increase. For simplicity, and with the ambition to explain a pH-effect, we assume only the adsorption of protons and hydroxyl ions to influence the interfacial tension as

$$d\gamma = -(\Gamma_{H^+} d\mu_{H^+} - \Gamma_{OH^-} d\mu_{OH^-}) \tag{4.3.3}$$

via the protonation/deprotonation equilibrium of the magnetite surface hydroxyl groups.[89] Hence with an increase in pH a lowering of the magnetite surface tension is induced leading to an increase in the system's total interface following Equation (4.3.1). For particles in a closed system, an increase in total surface area corresponds to a decrease in particle size. Based on the above derivation a semi-quantitative modeling has been successfully employed to predict the decrease in magnetite particle size with an increase in pH.[90]

Following this line of thought of the relationship between particle size, surface tension, and interfacial adsorption, we aim to deduce the influence of the added polymer analogously. We envision the polymer, acting as a polycation, to electrostatically adsorb to the negatively charged magnetite surface. As in the case of counterions in solution, adsorption at the oxide/water interface induces a further lowering of the surface tension, as predicted by the Gibbs adsorption isotherm Equation (4.3.2) leading to a further decrease in particle size. Indeed, experimental data demonstrate that the diameter of magnetite nanoparticles varies, from between 4 nm at low $NaNO_3$ concentrations at a given pH to 0.8 nm for high concentrations.[89] As for ions, we may infer that adsorption of poly-L-arginine at the magnetite/water interface induces a lower surface tension that would lead to a decrease in particle size. This effect should even be more pronounced as the adsorption of a polyelectrolyte with n charges will come with a smaller entropic penalty as the adsorption of n monovalent counterions, which can be predicted purely based on a statistical placement of the n charges. Unexpectedly, for the poly-L-arginine magnetite particles, we observed the opposite effect, as they increase in size with increasing pH. This unusual pH effect precludes a simple classical evaluation of the nucleation of magnetite in the presence of poly-L-arginine. While these theories describe the formation of stable nuclei and further growth based on thermodynamic energy minimization, it is further difficult to envision how a sub-structured mesocrystal may be formed via such a mechanism.

Thus, turning our attention to earlier introduced non-classical theories seems thus to be an advisable approach. There are indeed many examples of non-classical nucleation in biological[52] and synthetic[91,92] systems exhibiting an excess surface charge, where oppositely charged additives are thought to kinetically trap transient precursor phases, altering the crystallization pathway and resulting in a wealth of sophisticated structures and morphologies of nanoparticles. For magnetotactic bacteria, it was possible to identify transient ferric hydroxide phases stabilized by charged proteins that crystallize to form magnetite via nanometric (oxyhydr)oxide intermediates[82]. Polymorph selection in precipitation of $CaCO_3$ forming either vaterite or amorphous calcium carbonate in the presence of polyaspartic acid, has been demonstrated in *in vitro* experiments[92]. Moreover, prior research has already demonstrated that adding negatively charged polysaccharides inhibits magnetite nucleation at pH values up to 13[91].

The unifying concept of the given examples, of both natural and synthetic origin, is the existence of thermodynamically less stable polymorphs such as iron (oxyhydr)oxide or amorphous calcium carbonate from which the thermodynamically more stable phases magnetite and calcite are formed[93]. Past research has shown, that interaction with charged macromolecules results in kinetic stabilization, preventing crystallization into the thermodynamically more stable (and also denser) phase.

The transition from superparamagnetic to ferrimagnetic particles is consistent with the increase in particle size measured by TEM and XRPD. The sub-structured morphology of particles obtained at pH 11 yields particles whose crystallographic orientation is constant throughout the structure. The magnetic properties, therefore are very similar to those that have been reported for synthesized magnetite or magnetosomes of magnetotactic bacteria with similar size of 34 nm.[94]
The SSD behavior of the sub-structured particles prepared at pH 11, however, requires some further discussion. Mesocrystals, generally described as an assembly of nanocrystallites spatially confined to a crystallographic superlattice, are known to couple and amplify directional physical properties of their building blocks. A marvelous example of this amplification is superparamagnetic magnetite colloidal nanocrystal clusters[95] that were synthesized in high-temperature hydrolysis of ferric chloride. Those clusters consist of small SP magnetite particles and can reach sizes up to 180 nm while being superparamagnetic. The saturation magnetization of those SP clusters, however, is increased with increasing cluster size. With the proposed formation mechanism by Reichel et al., were our mesocrystals are also thought to assemble from polymer immobilized SP nanoparticles, the observation of SSD behavior seems thus surprising and still lacks a physically meaningful explanation. With the elucidation of the formation mechanism of magnetite in the presences of poly-L-arginine in Chapter 5, we attempt to explain this surprising behavior.

4.4 Conclusion

In conclusion, we show that superparamagnetic as well as stable single domain magnetite nanoparticles can be selectively grown in the presence of poly-L-arginine simply by changing the pH of the precipitation solution. Even though the effect of pH[96,97], biological[64,98] and synthetic[44] additives on the precipitation of magnetite has been extensively studied within the recent years, the presented control over size and size distribution of the nanoparticles is exceptional. We thus combine many of the previously reported advantages in one system. These properties in combination with their long term colloidal stability, render these biomimetic functional materials ideal for applications. Unexpectedly, the size of the nanoparticles increases with increasing pH, in contrast to naked magnetite particles produced under the same conditions, which decrease in particle size when the precipitation pH is increased.

Classical notions of nucleation fail to explain this unexpected pH dependence as well as the complex, sub– structured morphology of the mesocrystals formed at pH 11. Thus, a reference to non—classical nucleation theories suggest that the magnetite/poly-L-arginine nanoparticles may crystallize from polymer-stabilized transient, low-–density iron phases. Others already considered magnetite formation via these transient iron phases, a stabilization by polymeric additives, however, was not reported.[71,99] Finding and characterizing these proposed precursor structures, that would support the proposed non-classical nucleation pathway, will thus be the focus of the next chapter.

Chapter 5

In Situ SAXS and Nucleation Mechanism

Summary In the biomimetic approach of adding poly-L-arginine in the co-precipitation of ferrous and ferric chloride we found extraordinary results, including the morphological change from single to mesocrystalline and an inverted effect of pH on the size of magnetite nanoparticles. We thus strive to get a more sophisticated glance on the envisioned mechanistic changes, which the addition of poly-L-arginine may induce. We thus developed a SAXS setup to follow the formation of the magnetite nanoparticles *in situ* spatiotemporally resolved. Using analytical form factor models, we extracted crucial structural parameters in dependence of time, from which we concluded that the addition of poly-L-arginine may shift the mechanism of the reaction from a thermodynamically to a kinetically controlled one. We were further able to explain the pH-dependent change in morphology, which is induced by a change in the wettability of the nanoparticles and an alkaline accelerated solid-state phase transition. However, in order to exert this effect, poly-L-arginine needs to have a minimum of 16 monomer units. Understanding the mechanism and realizing that the particle growth is only retarded by the presence of counterions, we modified the synthesis setup and show that magnetite nanoparticles in the presence of poly-L-arginine can be virtually indefinitely grown. The presented work elucidates the effect of poly-L-arginine on the nucleation of magnetite and highlights how a mechanistic investigation can drive the development of nanoparticle properties.

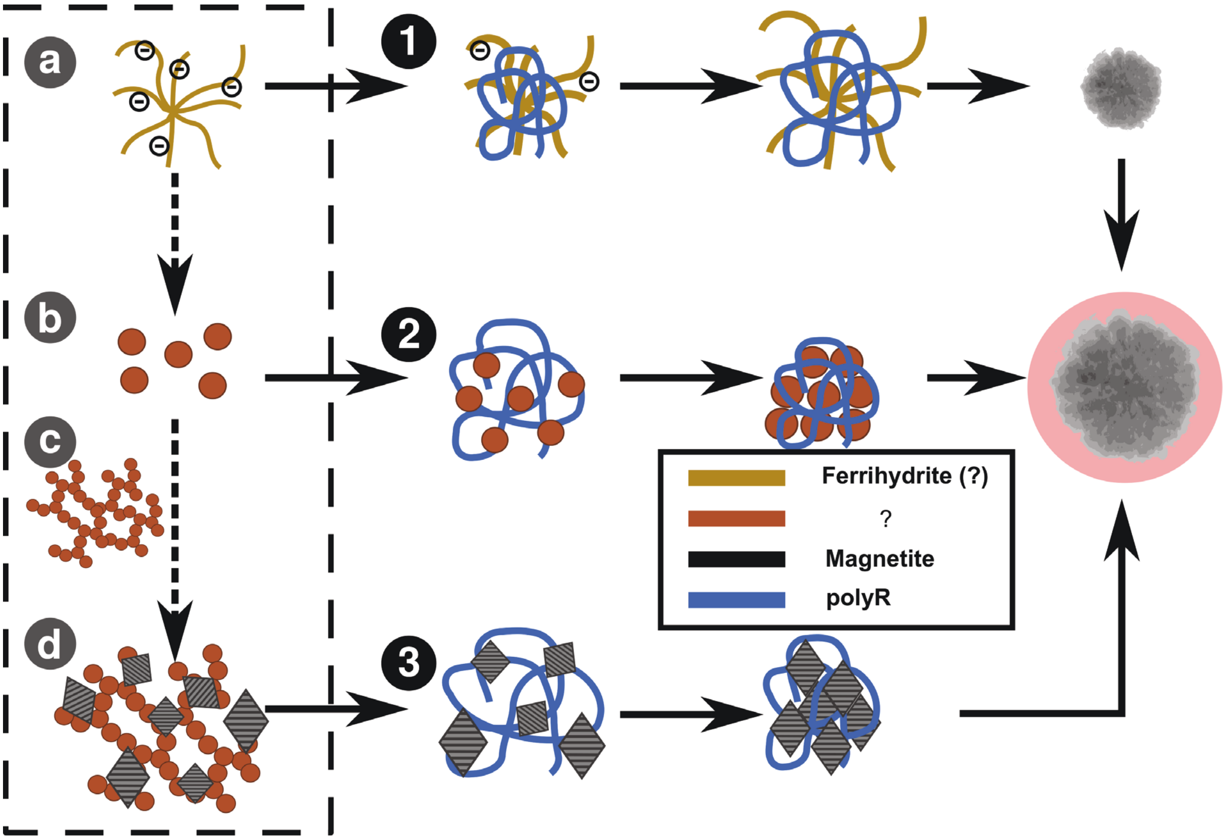

Figure 5.1: Possible formation mechanisms of magnetite in the presence of poly-L-arginine. The dotted line marks the nucleation pathway of magnetite from solutes in the absence of any additives. We can envision the polymer to interact at different stages 1)-3) with the different iron phases and intermediates proposed by Baumgarnter et al.[72], including ferrihydrite a), single particles and agglomerates of iron(oxi)hydroxide b)-c) and magnetite d)

5.1 Working Hypothesis

Referencing the mechanism of magnetite formation introduced in section Section 2.1 based on the investigation of Baumgartner et al.[72], an interaction with poly-L-arginine, acting as a positively charged polycation, can be envisioned at different points of this mechanism as indicated in Figure 5.1 1)-3). We here explicitly want to discuss the mechanism for the formation of mesocrystals and neglect the effect of pH, resulting in solid single crystals. At a later point, we will see how the proposed mechanism can be applied to explain the transition from single crystal to mesocrystal. Path 1) considers a ferrihydrite gel-like structure that is stabilized by poly-L-arginine against densification to form primary particles. The stabilized gel consecutively grows, until it collapses, to form a mesocrystal seed. Mesocrystals then grow by consuming the consecutively formed iron precursor particles. 2) poly-L-arginine can function as a scaffolding agent to electrostatically immobilize formed primary particles before they aggregate. This network of polymer and primary particles collapses, forming, in turn, an aggregate of primary particles with the incorporated polymer. Complementary to the classical mechanism, magnetite nucleates from this aggregate of primary particles while the polymer is incorporated, forming the seed for further particle growth by consumption of the polymer/primary particles network. The 3rd formation mechanism proposed by Reichel et al.[65] (inspired by the mechanism by Baumgartner), however, appears unlikely as free 10 nm sized magnetite particles are envisioned to be scaffolded by the polymer to form the final mesocrystal via oriented attachment. Non-aggregated, colloidally stable magnetite nanoparticles, however, have not been proposed to be part in the mechanism of magnetite co-precipitation. We thus propose either path 1) or 2) to be a possible mechanism in the formation of magnetite/poly-L-arginine mesocrystals. In order to elucidate which mechanism is the best fit, we employ *in situ* SAXS.

X-ray scattering is at the forefront of mechanistic nanoparticle research enabling simultaneous atomistic to micron-size resolution, while particles can be observed in their native state at operando conditions. Examples from literature show the versatility of SAXS to study nucleation phenomena. SAXS can provide milli second time-resolution[100] often when coupled to a stopped-flow apparatus[101,102]. Magnetite formation under harsh conditions using supercritical water[103] or quantum dot synthesis at high temperatures[104] have been investigated using SAXS setups. A good example of how a creative design of an experiment can drive nanoparticle research has been done by Polte et al. studying the formation of gold nanoparticles simultaneously with SAXS and XANES (X-ray absorption near edge structure) in a levitated droplet functioning as a scatter-less mini-reactor. Also iron oxide formation has already been subject to SAXS investigation.[105–107] However, even though SAXS can be considered an ideal tool to study the nucleation of nanoparticles, the ultra-low iron concentration in the early stages of our synthesis, would impose detection problems due to the inherent low scattering intensity. A high brilliance 3$^{\text{rd}}$ generation synchrotron x-ray source is thus necessary, to resolve the early structures present in the synthesis.

5.2 Qualitative SAXS Analysis

Already a qualitative comparison of the *in situ* SAXS data with the expected scattering of the structures involved in the envisioned nucleation pathways (Figure 5.1 1) and 2)) enables us to exclude the second option. In 2) within the first 15 min we observe an increase in intensity with the characteristic scattering signal of a structure of ξ=2π/q$\approx$5 nm power law transition in Figure 5.2 with a radially decreasing scattering length density. As the pure polymer does not scatter significantly above the background, we predict that the scattering must arise from condensed iron. At this point we can only speculate about the actual structures present and about the involvement of the polymer. We can imagine i) poly-L-arginine being decorated with low-molecular polynuclear complexes of up to 4 iron atoms due to electrostatic interactions.[108,109] These clusters electrostatically interact with the polymer, reducing the overall charge, and thus favoring intra-polymer

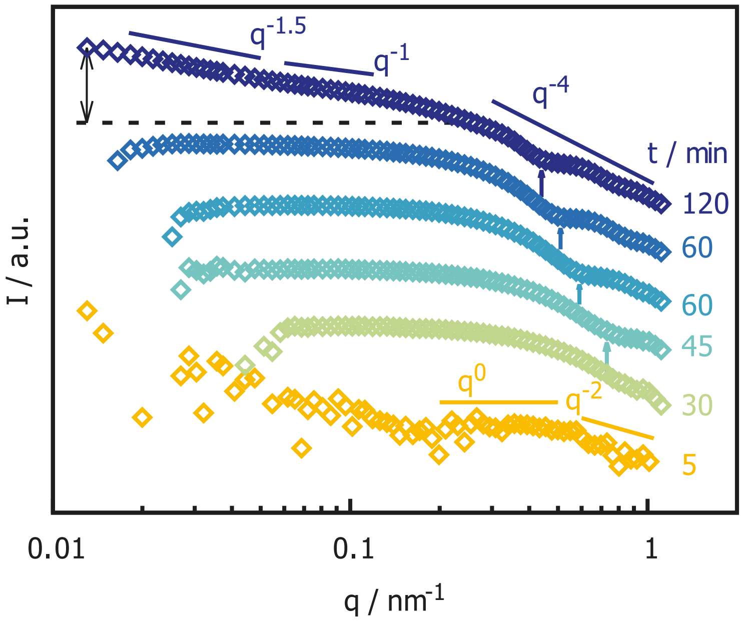

Figure 5.2: Excerpt of selected time points of azimuthally integrated *in situ* SAXS data of the coprecipitation of magnetite in the presence of poly-L-arginine at pH 11. Within the first 5 min we see a scattering contribution of iron density fluctuation with a radial density decrease following a power law of 2, indicated by the scattering power law envelope of q^{-2}. From the transition of this slope to the intensity plateau (q^0) a characteristic correlation length of $\xi = 2\pi/q \approx 8$ nm of these density fluctuations can be inferred. With time (30 min) the scattering contribution of these density fluctuations, or precursor particles, increase until solid nanoparticles appear at around 40 min. The nanoparticles grow continuously, visible in the constant shift of the form factor minimum to higher q, as indicated by the arrows. The scattering envelope of less then q^{-4} for late time points indicate that the precursor particles coexist with the solid nanoparticles, that would, by themselves, scatter as q^{-4}. After approximately 2 hours the particles become ferrimagnetic with the inherent permanent magnetic dipole moment, that induces chaining of the particles apparent in the increase in intensity at low q. These chains appear locally stiff and rod-like (q^{-1}), while the complete chain deviates from an ideal rod conformation and appears more flexible ($q^{-1.5}$). From the intensity factor between the extrapolated forward scattering of the single nanoparticle and the intensity at lowest q (indicated by the dotted line and the arrow), we can estimate the number of particles per chain to be at least 100 magnetite nanoparticles.

interaction, which manifests itself in the reduction of the Flory parameter. From the power-law (q^{α}) $\alpha \approx$-2 at high q a Flory parameter of 0.5, that of a Gaussian polymer coil, is suggested.[110] ii) The poly-L-arginine is decorated with primary particles thus collapses due to charge neutralization to a Gaussian coil as in i). In both cases, the polymer functions as a scaffold to aggregate particles. However, the gyration radius of ∼4-5 nm of these structures exceeds by a factor 5 the expected size for an aggregate of condensed iron immobilized on the 5-15 kDa polymer, which would have an expected gyration radius of 1-2 nm given an amino acid backbone with a unit length of 0.4 nm per amino acid. Further, the molecular weight of the polymer does not influence the morphology and size of the condensed structures, as we will see in section Section 5.4.3, which would be expected if the polymer was acting as a scaffold.

The appearance of form factor oscillation after 30 min (arrow Figure 5.2) indicates the presence of solid nanoparticles. The continuous shift of the form factor minimum to lower q indicates a continuous growth of the nanoparticles, either by the attachment of molecular iron or by consumption of the formed precursor particles. For solid nanoparticles, a scattering power law of q^{-4} is expected. However, at any time point after the appearance of solid nanoparticles, we find a scattering envelope of less than -4. We can thus assume a continuing scattering contribution of the precursor structures that were formed during the first 30 min and are continuously reformed due to the continuous addition of iron solution.

An increase in intensity at low q after 120 min indicates the formation of particle chains with a local stiffness, seen in the power law of q^{-1} at mid q, that seem less stiff when the window of observation is increased (low q). We can estimate the number of particles per chain from the scaling factor between the forward scattering intensities of the chains and the particles. After two hours, chains should contain on average more than 100 magnetite nanoparticles. Also, based on SAXS data, we can confidently refute the formation path in Figure 5.1 3) that has been previously presented as the underlying mechanism for the mesocrystal formation.[65] The key step was the concerted assembly of a 10 nm sized single species of magnetite, forming a unique species of 40 nm sized mesocrystals, that were not considered to continue growing but only increase in concentration. In SAXS we neither find a unique species of 10 nm, nor 40 nm particles. Further, the continuous particle growth, the effect of pH, forming meso- and solid crystals cannot be predicted based on the formerly proposed mechanism.

With this working hypothesis for the expected mechanism we engage in further analysis of the SAXS data using analytical form factor models.

5.3 Analytical SAXS Model

As introduced earlier, the mathematical description of the scattering process can be obtained by the Fourier transform of the scattering length density distribution function. Real space informa-

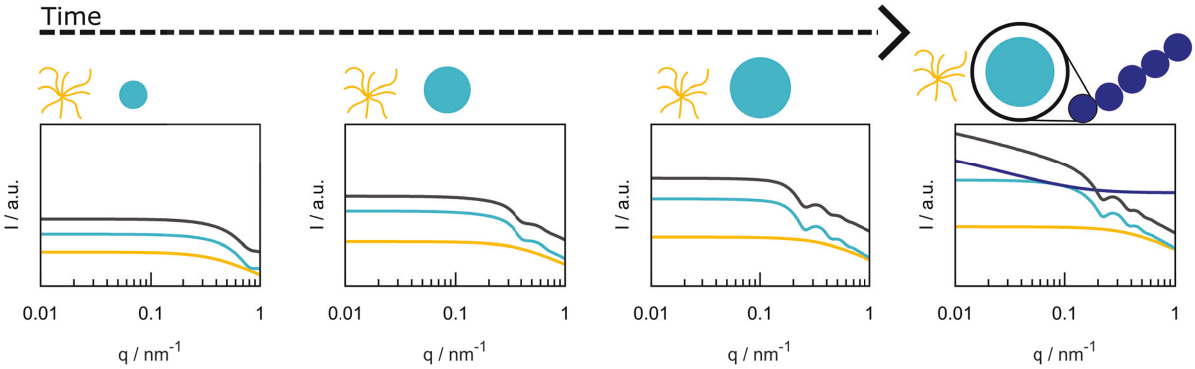

Figure 5.3: Simulated scattering curves of the iron-containing structures that we envision to be involved in the formation of magnetite nanoparticles. A low-density iron phase (yellow) initially exist and will be transformed to magnetite seed particles (light blue circles) that grow with time. After crossing the stable single domain size threshold particles will interact and form chains due to dipolar interaction resulting in a structure factor (dark blue). Scattering curves for the appropriate structures are colored according to the color of the structure, while the dark grey curve shows the combined scattering of all structures present and the depicted time point.

tion cannot be readily obtained through an inverse Fourier transform, due to the loss of phase information in the scattering process. Thus, we here rely on the numerous analytical solutions of the Fourier transform of the scattering length density distribution function proposed for different particle morphologies. For the sake of thesis space, we will abstain from an elaborate discussion of the form factor derivations and refer the interested reader to the appropriate literature. Following the proposed formation path, which is schematically shown in Figure 5.1, we model the precursor structures with a fractal (yellow structures) intensity form factor with a cut-off radius proposed by Hurd and Flower[111]. The growing nanoparticles (light blue circles) are approximated by the square of the modulus of the classical sphere form factor amplitude. Particle size distribution is modeled assuming a Schulz-Zimm probability distribution function. Chain formation (dark blue chains of particles) due to anisotropic magnetic interaction was modeled using a square well potential. All scattering models were implemented into the Matlab-based SASET program.[112] All datasets and corresponding fits are attached in the Appendix, Figure 8.

5.4 Quantitative SAXS Data Analysis

5.4.1 Influence of pH

The effect of pH on the formation of poly-L-arginine/magnetite particles is most unexpected. We have concluded section 4 with the conviction, that nucleation pathways of magnetite in the presence of poly-L-arginine cannot be classically explained by thermodynamic energy minimization based ion

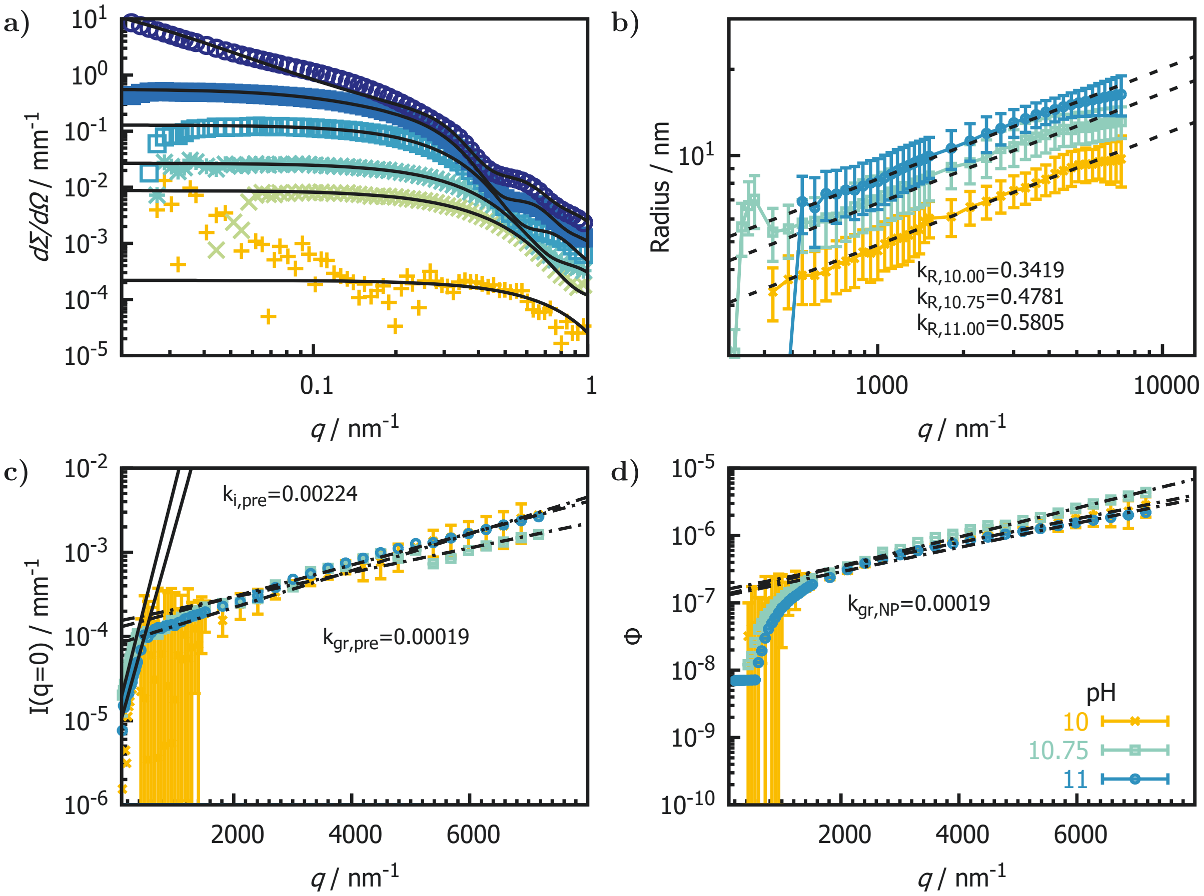

Figure 5.4: An excerpt of the SAXS data in absolute scale with corresponding fits is shown in a). We fitted the radial growth of nanoparticles with an exponential time dependence fixing the power law to 2.6. We described time-dependent evolution of nanoparticle and precursor concentration with an exponential. The concentration of the precursor particles c) exhibit an induction phase ($k_{\mathrm{i,pre}}$=0.03 mm^{-1} s^{-1}) and a second phase at which precursor particles are consumed by growing nanoparticles appearing after approximately after 300 s. ($k_{\mathrm{gr,pre}}$=0.00021 mm^{-1} s^{-1}). The volume fraction d) of nanoparticles increases at a rate of $k_{\mathrm{gr,gNP}}$=0.00021 mm^{-1} s^{-1}. For all pH the increase of concentration of the precursor particles as well as the volume fraction of the nanoparticles follow the same rate.

accretion from solution. In summary, two observations were particularly obscure: i) the inversion of the size dependence of magnetite with pH compared to particles prepared in the absence of any additive and ii) the change in morphology, finding spherical, solid magnetite single crystals below pH 11, while particles above pH 11 will be formed as substructured mesocrystals, however, exhibiting properties of single crystals.

We have thus investigated the formation of magnetite in the presence of poly-L-arginine by *in situ* SAXS at pH 10, 10.75 and 11. Representative, SAXS data at pH 11 for different time points of the synthesis are shown in Figure 5.4 a). Corresponding fits are based on the analytical scattering model proposed in Section 5.3. Due to the dominant scattering of precursor particles within the first minutes of the reaction, their structure was readily determined to have a fractal dimension of 2.2 and a gyration radius of ≈4-5 nm. A change in pH unalters the fractal dimension as well as the size of these precursor particles. Approximating the nanoparticles as spheres we thus fit as free parameters the radius Figure 5.4 b) and the volume fraction Figure 5.4 d) of the growing magnetite nanoparticles as well as the forward scattering c) of the precursor particles, which is proportional to their number density. All concentrations were normalized by the residual volume in the reactor, taking into account sample withdraw, solution evaporation –due to the nitrogen stream– and added iron and sodium hydroxide solution during the experiment. The kinetics of the size evolution of magnetite was fitted as $R^n(t) = kt$ neglecting the particle seed size, $\mathrm{R}_{\mathrm{t=0}}$. The kinetic law, in its integrated form, is written as $R(t) = kt^{1/n}$, with the rate constant k and the growth exponent n, indicative of the growth mechanism. Concentrations of precursors and nanoparticles were fitted assuming a first-order reaction mechanism as $c(t) = 10^k \cdot c_0$.

The growth rate of the particles is proportional to the pH and increases from 0.059 $\mathrm{nm\,s^{-1}}$, 0.14 $\mathrm{nm\,s^{-1}}$, to 0.23 $\mathrm{nm\,s^{-1}}$ for pH 10, 10.75 and 11, respectively. While the growth rate is highly dependent on pH, we find a growth exponent of 2.6 consistently, implying a uniform growth mechanism for all pH values, even though the morphology of the final particles diverges drastically. The concentration of the precursor particles increases exponentially with a rate constant of $\mathrm{k_{i,pre}}$≈0.4 $\mathrm{mm^{-1}\,s^{-1}}$ within the first 300 s after which it flattens off to a rate of $\mathrm{k_{gr,pre}}$≈0.0002 $\mathrm{mm^{-1}\,s^{-1}}$. Both these rate constants remain unaltered by a change in pH. Concomitant with the retardation of the rate of formation of precursor particles, a scattering contribution of solid nanoparticles emerges. Based on this temporal correlation, we conclude, that the nanoparticles emerge and grow by consumption of the precursor particles. Due to the monotonic increase in nanoparticle number density REFERENCE SI and precursor particle volume fraction, we conclude that new nanoparticles, as well as new precursor particles, are persistently produced. Even though the growing nanoparticles consume precursor particles, their concentration increases over time, indicating that the rate of precursor formation is higher than their consumption rate. The rate constants for the increase in nanoparticle concentration ($\mathrm{k_{gr,NP}}$=0.00019 $\mathrm{min^{-1}}$) from Figure 5.4 d) is surprisingly consistent with the rates obtained for the increase in precursor particle concentration. All kinetic parameters are summarized in Table 5.1

Table 5.1: Kinetic parameters fitted at different pH values for the growth ($\mathrm{k_R}$) and increase of number density ($\mathrm{k_{gr,NP}}$) of the magnetite nanoparticles. The initial and final increase precursor concentration ($\mathrm{k_{i,pre}}$,$\mathrm{k_{gr,pre}}$) are also shown.

pH	$\mathbf{k_R}$	$\mathbf{k_{i,pre}}$ [$\mathrm{mm^{-1}\,s^{-1}}$]	$\mathbf{k_{gr,pre}}$ [$\mathrm{mm^{-1}\,s^{-1}}$]	$\mathbf{k_{gr,NP}}$ [$\mathrm{s^{-1}}$]
10	0.341±0.0015	0.00516±0.00041	0.00022±0.000006	0.00018±0.000007
10.75	0.478±0.0044	0.00277±0.00008	0.00015±0.000008	0.00022±0.000005
11	0.580±0.0029	0.00251±0.00009	0.00019±0.000004	0.00018±0.000007

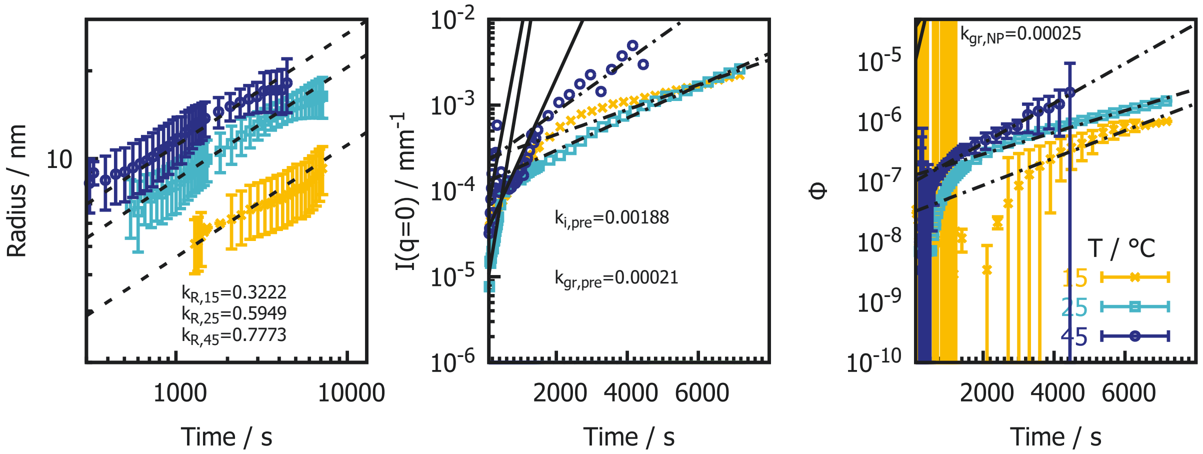

Figure 5.5: Time dependent parameters from synthesis conducted at 15°C, 25°C and 45°C. From the temperature dependence of radial nanoparticle growth in a) increasing with increasing temperature from k_{15}=0.05,k_{25}=0.25, to k_{45}=0.50 we later obtain the activation energy. The evolution of precursor and nanoparticle concentration are shown in b) and c) showing the precursor forward scattering and the nanoparticle volume fraction Φ, respectively. The corresponding kinetic constants are summarized in Table 5.2

5.4.2 Influence of Temperature

From the temperature dependence of magnetite formation, energetic clues about the nucleation mechanism can be inferred. Widdrat et al.[113] modeled the temperature dependence of the monomer addition rate of primary particles to growing nanoparticles, discriminating between a diffusion-limited and a reaction-limited growth model. Comparing the parameterized growth kinetics, to particle sizes obtained from PXRD measurements, it was concluded, that the growth of magnetite is likely limited by the reaction. Following this example, we studied the effect of temperature (15°C, 25°C, 45°C) for poly-L-arginine/magnetite particles at pH 11 by *in situ* SAXS.

The parameters obtained from fitting of the SAXS data are shown in Figure 5.5. Growth rates have been calculated using models introduced earlier in Section 5.4.1 to obtain the rate constant of the growth of the nanoparticle's radius (k_R) and number density ($k_{gr,NP}$) as well as the evolution of the precursor particle's concentration. All kinetic parameters obtained are summarized in Table 5.2. As for the pH dependence, the growth exponent was fixed to be 2.6 and best fit results where

Table 5.2: Kinetic parameters fitted at different temperatures for the growth of mesocrystals (k_R). The increase of number density ($k_{gr,NP}$) of the magnetite nanoparticles and the initial and final increase precursor concentration ($k_{i,pre}$,$k_{gr,pre}$) are also shown.

T [°C]	$\mathbf{k_R}$	$\mathbf{k_{i,pre}}$ [mm^{-1} s^{-1}]	$\mathbf{k_{gr,pre}}$ [mm^{-1} s^{-1}]	$\mathbf{k_{gr,NP}}$ [s^{-1}]
15	0.322 ± 0.0007	0.000034 ± 0.00003	0.00014±0.000008	0.00023±0.000014
25	0.594 ± 0.002	0.000097 ± 0.00001	0.00019±0.000004	0.00018±0.000007
45	0.777 ± 0.01	0.001010 ± 0.00004	0.00030±0.00003	0.00033±0.000011

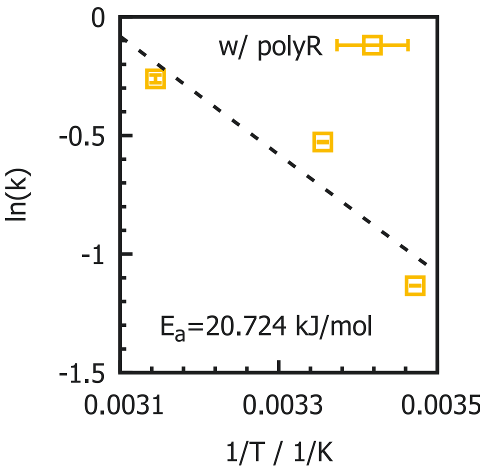

Figure 5.6: Arrhenius plot of the temperature dependence of mesocrystal growth rate. The activation energy of the precursor attachment is calculated from the slope of the linear regression divided by the gas constant. We find an activation energy of 20.72 kJ/mol, which is slightly lower compared to Widdrat et al.[113] that found an activation barrier for magnetite nucleation in the absence of any additives and at pH 9 of 24 kJ/mol.

obtained fixing the final size and fractal dimension of the precursor particles to ∼5 nm and a fractal dimension of 2.2, respectively. However, looking at the size evolution of the precursor particle at 15°C, an increase within the first 1500 s is apparent, as shown in the Appendix in Figure 5. This increase in size was taken into account and thus the radius of gyration of the precursor particles not fixed in the fitting routine of SAXS data recorded at 15°C. This precursor growth could not be temporally resolved for data collected at standard temperature and higher, due to the temperature-dependent increase in reaction rate, quantified by the growth rate $k_{R,15}$=0.322, $k_{R,25}$=0.594 and $k_{R,45}$=0.777, respectively. From the temperature dependence of the rate constants, we obtain the activation energy, E_A, of 20.72 kJ/mol of the reaction using the linearized Arrhenius equation $lnk = lnk_o - E_a/(RT)$, with the pre-exponential factor k_0. The corresponding Arrhenius plot is shown in Figure 5.6. This activation energy is slightly lower compared to Widdrat et al.[113] that found an activation barrier for magnetite nucleation in the absence of any additives and at pH 9 of 24 kJ/mol. The increase in the number density of the precursor structures as well as for the nanoparticles may be present as observed in other experiments. The fitting results, however, suffer from a strong scattering background and the from large errorbars of the fitted parameters.

5.4.3 Influence of Molecular Weight

From the study of the influence of molecular weight we can clearly refute alternative formation mechanisms. We assume that any mechanism that is based on the immobilization of either primary particles or matured magnetite nanoparticles, as proposed earlier in Figure 5.1, should be intimately

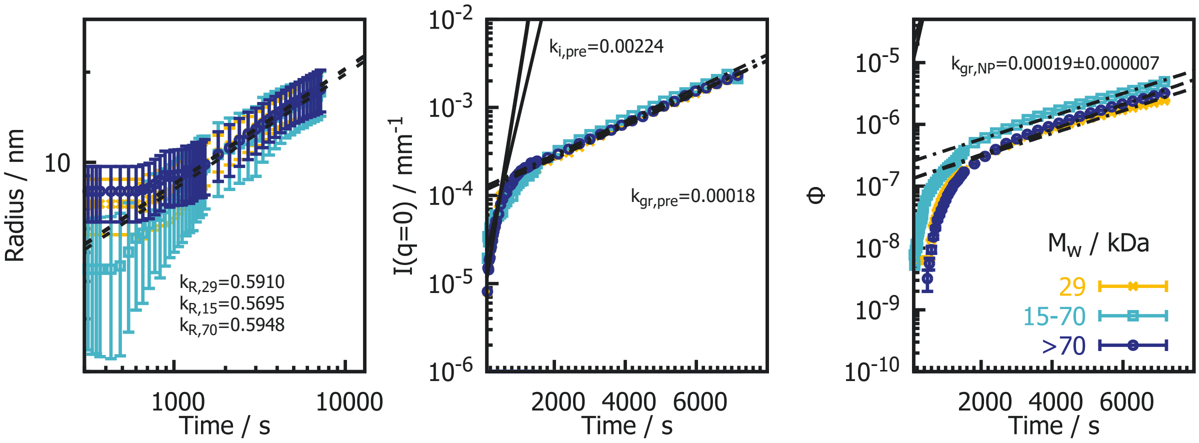

Figure 5.7: Parameters obtained from fitting SAXS data obtained for synthesis, where different molecular weights (29 kDa, 15–75 kDa, 70–150 kDa) of poly-L-arginine were used to produce mesocrystals at pH 11. Kinetic constants fitted to the growth of nanoparticles and the increase in the number density of the precursor structures and the nanoparticles are close to identical. The molecular weight of poly-L-arginine is thus assumed not to affect the formation of magnetite mesocrystals.

influenced by the chain length of the polymer resulting in either a change of precursor or nanoparticle size or both. We thus prepared mesocrystals at pH 11 using 29 kDa, 15–75 kDa and 70–150 kDa poly-L-arginine with corresponding monomer numbers of 185, 100-480 and 450-960 respectively. The time evolution of the parameters obtained from SAXS data fitting is shown in Figure 5.7. Precursor size and fractal dimension of ∼5 nm and 2.2 respectively resulted again in best fitting results for all molecular weights. Kinetic constants were fitted according to equations in Section 5.4.1. Respective growth constants for all molecular weights can be found in 5.3. It is striking, how preposterously identical the results for different molecular weights are. A significant effect of poly-L-arginine's molecular weight in these size ranges on the formation of magnetite is thus precluded.

Table 5.3: Kinetic parameters fitted to time dependent parameters obtained from *in situ* SAXS data. The growth (k_R) and increase of number density ($k_{gr,NP}$) of the magnetite nanoparticles, as well as the initial and final increase in precursor concentration ($k_{i,pre}$,$k_{gr,pre}$) are shown.

$\mathbf{M_w}$ [kDa]	$\mathbf{k_R}$	$\mathbf{k_{i,pre}}$ [mm^{-1} s^{-1}]	$\mathbf{k_{gr,pre}}$ [mm^{-1} s^{-1}]	$\mathbf{k_{gr,NP}}$ [s^{-1}]
29	0.591±0.002	0.0024±0.0001	0.00018±0.000002	0.00018±0.000008
15-70	0.569±0.003	0.0017±0.0002	0.00019±0.000003	0.00018±0.000006
>70	0.594±0.001	0.0025±0.0001	0.00018±0.000002	0.00020±0.000008

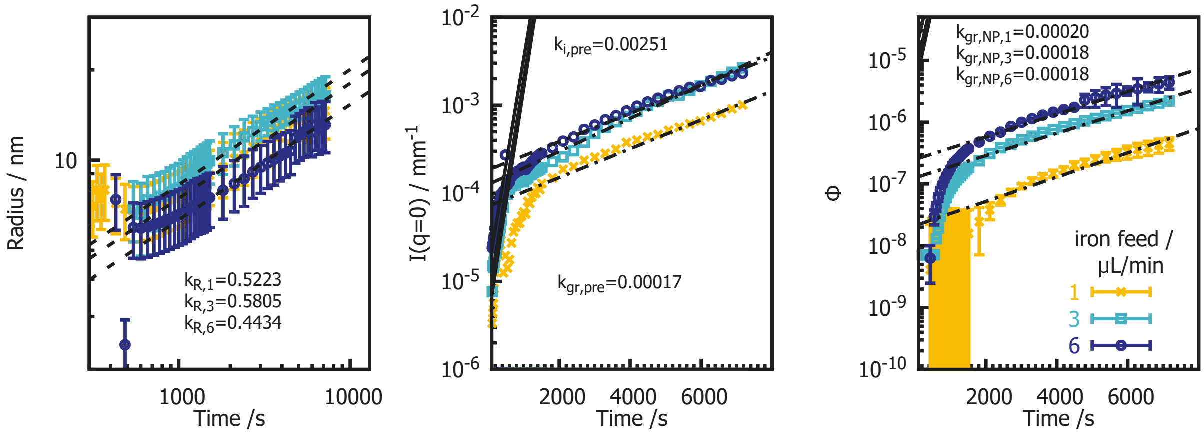

Figure 5.8: Parameters obtained from fitting *in situ* SAXS data collected at different time points of magnetite co-precipitation comparing different addition rates of iron solution. From left to right we plot the radial growth of nanoparticles, the increase in precursor concentration and the volume fraction, Φ of solid nanoparticles. An increase of the particle growth rate a) with an increase in feeding rate was predicted, but could not be confirmed, as the growth rate does not follow the iron addition rate uniformly. To accelerate the nanoparticle growth, we find an optimal feeding rate of 3 µL/ min under the given conditions. Fitted kinetic parameters are summarized in Table 5.4.

5.4.4 Influence of Iron Feeding Rate

Following the argumentation by Baumgartner et al.[59] that the growth rate of pure magnetite is proportional to the iron reservoir available per growing particle, we expect increased growth kinetics, when more iron is supplied from which the nanoparticles can grow. We thus investigated the effect of the feeding rate of the iron solution into the synthesis. poly-L-arginine/magnetite mesocrystals were prepared at pH 11 and a constant polymer concentration of 1 mg mL^{-1}, while the addition rate of the iron solution was varied to be 1 µL/ min, 3 µL/ min (standard addition rate) and 6 µL/ min. *In situ* SAXS data was fitted according to Section 5.3 and the time-dependent fitting parameters plotted in Figure 5.8. Best fits were obtained using a precursor particle size of ∼5 nm and a fractal dimension of 2.2. We obtained kinetic constants according to models proposed

Table 5.4: Kinetic parameters obtained from fitting time dependent scattering parameters obtained from *in situ* SAXS data for different feeding rates of iron solution. The growth (k_R) and increase of number density ($k_{gr,NP}$) of the magnetite nanoparticles, as well as the initial and final increase in precursor concentration ($k_{i,pre}$,$k_{gr,pre}$) are shown.

iron feed [µL/ min]	$\mathbf{k_R}$	$\mathbf{k_{i,pre}}$ [mm^{-1} s^{-1}]	$\mathbf{k_{gr,pre}}$ [mm^{-1} s^{-1}]	$\mathbf{k_{gr,NP}}$ [s^{-1}]
1	0.522±0.003	0.00261±0.00033	0.00016±0.000006	0.00020±0.000010
3	0.581±0.005	0.00251±0.00009	0.00019±0.000004	0.00018±0.000007
6	0.443±0.002	0.00242±0.00008	0.00016±0.000005	0.00018±0.000007

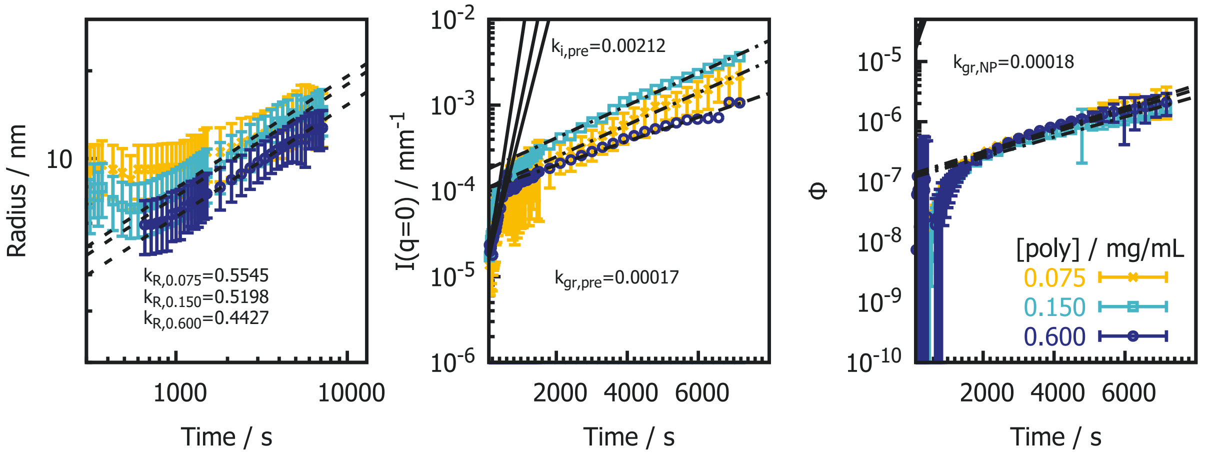

Figure 5.9: Time dependent fitting parameters obtained from *in situ* SAXS data taken for different concentrations of poly-L-arginine for mesocrystals prepared at pH 11 and an iron feeding rate of 3µL min^{-1}. a) shows the radial growth of the nanoparticles. In b) and c) the respective evolution of the concentration of precursor particles and the volume fraction of mesocrystals is shown. The radial growth rate decreases with increasing polymer concentration. Fitted kinetic parameters are summarized in Table 5.5.

in 5.4.1 assuming a mechanism that corresponds to a growth exponent of 2.6. Growth rates for different iron feeding rates are summarized in Table 5.4. The expected dependence of an increase in growth kinetics with an increased iron feeding rate cannot be confirmed. There is no continuous trend of the feeding rate with the growth kinetics of the mesocrystals. We rather find an optimal feeding rate of 3 µL/ min to optimize the particles growth rate under given conditions. Again, the growth rates of the concentration of the nanoparticles are close to identical. Total concentrations and volume fractions, however, are proportional to the feeding rate.

5.4.5 Influence of Polymer Concentration

To investigate the influence of polymer on the nucleation of magnetite, we imagined that any effect the polymer has on the nucleation of magnetite may be amplified, when more polymer is present. Further, following the initial thought of a polymer stabilized precursor iron phases, we may expect an effect on the polymorph selection, as it has been reported in literature for amorphous $CaCO_3$.[92,114] We thus synthesized mesocrystals at pH 11 while adapting the concentration of poly-L-arginine to be 0.075 mg mL^{-1}, 0.1 mg mL^{-1} and 0.3 mg mL^{-1}. The parameters obtained from *in situ* SAXS measurements are shown in Figure 5.9. Best to the SAXS data fitting analytical description was obtained fixing the radius of gyration and the fractal dimension of the precursor particles to ∼5 nm and 2.2, respectively. The fitted kinetic parameters are summarized in Table 5.5.

Table 5.5: Kinetic parameters obtained from fitting time dependent scattering parameters obtained from *in situ* SAXS data obtained for polyR concentrations. Mesocrystal growth (k_R) and increase of number density ($k_{gr,NP}$) of the nanoparticles, the initial and final increase precursor concentration ($k_{i,pre}$,$k_{gr,pre}$) are summarized.

$\mathbf{c_{polyR}}$ [mg mL^{-1}]	$\mathbf{k_R}$	$\mathbf{k_{i,pre}}$ [mm^{-1} s^{-1}]	$\mathbf{k_{gr,pre}}$ [mm^{-1} s^{-1}]	$\mathbf{k_{gr,NP}}$ [s^{-1}]
0.075	0.554±0.010	0.0020±0.0002	0.00019±0.000003	0.00018±0.000009
0.150	0.519±0.003	0.0026±0.0001	0.00019±0.000004	0.00017±0.000008
0.600	0.442±0.001	0.0016±0.0001	0.00014±0.000005	0.00018±0.000011

5.4.6 Summary Results

Summarizing *in situ* SAXS data, we find a radial growth exponent for the nanoparticles of 2.6 independent of the parameters tested. Except for the temperature-dependent measurements, the same rate of concentration increase of the precursor structures and the nanoparticles is prevalent in all parameters tested. Consistently for all measurements, an initial increase of precursor concentration is retarded concomitant with the appearance of nanoparticles. For a maximum radial growth rate of nanoparticles, we find an optimal iron feeding rate of 3 µL min^{-1} and polymer concentration of 0.1 mg mL^{-1}. We find an inversion of the growth rate in dependence of pH, compared to the formation of magnetite in the absence of any additives. The highest growth rate measure in was achieved for pH 11, where mesocrystals are obtained. Independent of the parameters tested, we could not identify a change of the structure of the precursor particles. We find no significance influences of poly-L-arginine's molecular weight on the growth rate of nanoparticles, nor the structure and size of the precursor particles.

5.5 Discussion

5.5.1 Growth Mechanism

The growth exponent, n, is a characteristic parameter to decipher the reaction mechanism. We expect a growth exponent of n=1 for reaction, n=2 for diffusion-limited growth and n=3 for grain ripening based on Ostwald's mechanism.[115] However, we find a growth exponent of 2.6 consistently, indicating a rather slow growth, compared to the reaction- and diffusion-limited growth. We can thus not simply classify our reaction and can thus not simply proceed with kinetic description developed for either of them. Not only the growth model does not fit existing theories but also the increase in monodispersity of the formed nanoparticles with time is surprising. For a purely stochastic nucleation process, with newly formed nanoparticles and nonpreferential adsorption of precursor particles, self-similarity[116] of the formed particles is expected, as it was also shown for pure magnetite[59], predicting an n-fold increase in particles size distribution with an n-fold increase in particle size. Thus a progressing polydispersity with nanoparticle growth is suggested, which is in harsh contrast to what we observe in our system. Classical theories may fail to predict our observation as they have been developed for closed systems. The consecutive addition of iron and thus, the constant supply with freshly formed precursor particles and nanoparticles, as we observe it in SAXS, may induce a complexity of the resulting structural data that exceeds our current capabilities to predict a complete and comprehensive formation mechanism. However, pivotal conclusions are still concealed in the SAXS data.

5.5.2 Shifting from Thermodynamic Control to Kinetic Control

In 1.1 we have learned that the overall kinetics of phase separation or nucleation can be described as the product of a thermodynamic term $e^{-\Delta G/k_BT}$ and a second term describing kinetic barriers with energy E_A (such as ion dissolution and structural rearrangements)e^{-E_A/k_BT}.[72] While we have demonstrated in section Section 4.1 that thermodynamic considerations were not sufficient to describe static dependence of nanoparticle size on pH, *in situ* SAXS data now elucidates that, correlative to the static properties, the growth rate, k_R, of the nanoparticles is proportional to pH, opposed to magnetite precipitated in the absence of additives.[72]

We thus propose that, by the addition of poly-L-arginine, the thermodynamically controlled formation mechanism of pure magnetite is shifted to a kinetic one so that the kinetic term $e^{-\Delta G/k_BT}$ essentially drives the formation of nanoparticles. Especially the observed low density of the precursor structures supports this hypothesis. In agreement with the Ostwald step rule introduced in section Section 1.2, a less dense and thus thermodynamically less stable amorphous phase will form more readily compared to a dense, crystalline polymorph. A cascade of solid-state transitions will then form the final crystalline phase. The proposed low density for precursors fits well the proposed precursor structure observed by SAXS. Processes governed by these successive transformations of phases are also well known in biomineralization and are considered to be kinetically controlled. Involvement in this process of charged macromolecules has been reported for *in vivo* and *in vitro* systems that are considered to kinetically stabilize metastable polymorphs.[51,114] [cite more, amorphous polymorphs in vitro and in situ]

We postulate that poly-L-arginine kinetically stabilizes the low-density precursor particles, arguably a metastable polymorph of magnetite, and thus alters the successive phase transformation involved in the nucleation process of magnetite. We thus suggest a formation mechanism for poly-L-arginine/magnetite involving the insinuated sequential structural transitions schematically shown in Figure 5.10, including the corresponding energy landscape of the reaction, as well as a qualitative theromodynamic stability of the proposed structures and corresponding activation energies of foreseen transformations. The schematic reactions a) and this energy diagram will be the bases of the mechanistic discussion in following paragraphs. The numbers in Figure 5.10, correspond to a reaction step and will be referenced in the headings of the consecutive chapters. We do not guarantee that this pathway includes all structures involved in the formation of magnetite in the presence of poly-L-arginine. However, a majority of the observations from *in situ* SAXS measurements can be explained based on the predicted structures.

5.5.3 Step 1 and 2: Formation of Precursor Particles

Step 1 in Figure 5.10 describes the formation of the 5 nm, low-density precursor structures from solution. If we assume that these structures were formed by accretion of ion from solution, classical nucleation theory should be applicable, stating that the formation is driven by supersaturation, which in turn is dependent on the precipitation pH and hence is the thermodynamic activation energy. Congruent to magnetite formation in the absence of additive, we should thus find an anti-proportionality of pH and the gyration radius of the precursor particles. Another possibility is the inversion of precursor size with pH, which would hint to a similar formation mechanism for the precursor particles, compared to the nanoparticles. We could not find clear evidence for a change in precursor size with a changing pH in the*in situ* SAXS data. The structure, size, and intra-particle dynamics will be subject of an upcoming cryo-XANES/EXAFS beamtime, which will provide us with data to answer these questions.

Mechanistic conclusions, however, can also be obtained from the structure of the precursor particles. Following Schäfer[117] we find that a fractal dimension of 2.2 can be attributed to structures formed in a reaction-limited cluster-cluster aggregation process. Following literature[71,108,109] we imagine the building blocks of the precursor particles to be low-molecular ferric oligomers of di-or tri-mer iron complexes. Due to its lower solubility at alkaline conditions, we assume a prevalence of ferric iron in the precursor particles. This suggests that the dominant iron phase in the early nucleation steps is a disordered, non-crystalline ferric oxyhydroxide, like ferrihydrite. Structures similar to our precursor particles have been reported previously for iron oxide formation from ferric salts in systems with low driving force for phase separation (low pH)[109,118–120], also exhibiting low fractal dimension between 2.2 and 2.5[121–123] and sizes ranging from 4 to 9 nm. These structures are, under standard conditions, not know to be thermodynamically stable at high alkalinity, which further supports the idea of an increase of the kinetic barrier for phase transformation when poly-L-arginine interacts with the low-density precursor particles.

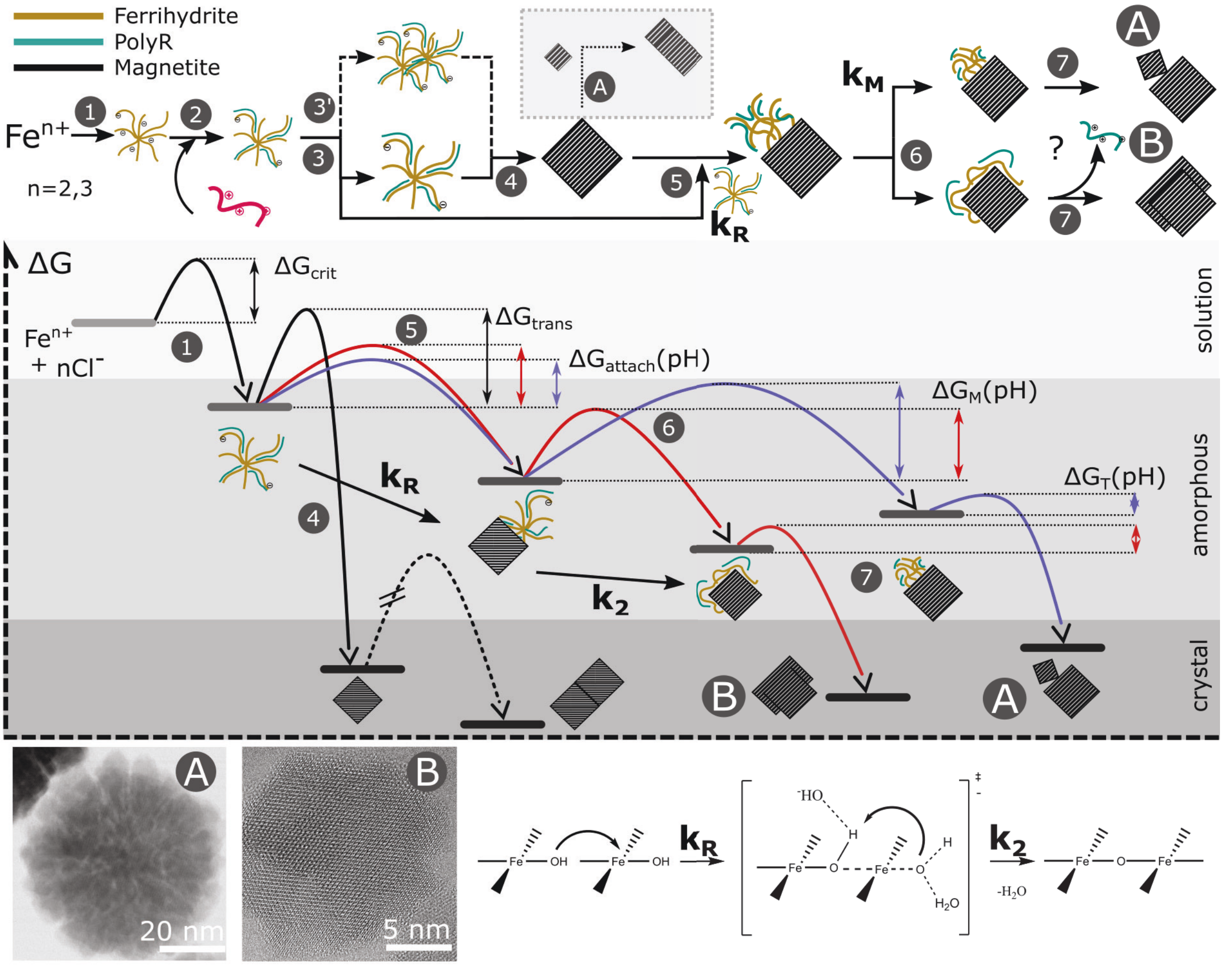

Figure 5.10: Scheme of the proposed final mechanism. Main reaction steps are indicated by solid arrows and numbers, while numbers indicating possible side or alternative reactions are marked with ánd dotted arrows. Capital letters indicate the final nanoparticle morphology that can be either substructured mesocrystalline (A) above pH 11 or spherically dense (B) below pH 11. We have qualitatively defined the free energy of proposed species and the corresponding energy barriers. Density, degree of hydration and atomic ordering, classify the proposed structures as either a solute (light gray), an amorphous, metastable precursor (gray) or thermodynamically stable, crystalline magnetite (dark grey). In order to explain the effect of pH, we have colored affected activation barriers in red (low pH) and blue (high pH). Energie barriers proposed to exist are the critical barrier of seed/precursor formation, ΔG_{crit}, the energy barrier associated with the self condensation of precursor particles to form magnetite nanoparticle seeds, ΔG_{trans}, that competes with the attachment of precursors to growing nanoparticles, $\Delta G_{attach}(pH)$. We identify this step to determine the nanoparticle growth rate, $\mathrm{k_R}$, which is catalyzed at high pH, consistent with the first step of the oxolation reaction (bottom left). After the attachment, precursors need to migrate over the nanoparticle surface in order to attach,$\Delta G_M(pH)$, which is retarded at high pH in the second oxolation reaction step, $\mathrm{k_M}$. The solid-state transformation from the low-density precursor particle to magnetite, $\Delta G_T(pH)$, is accelerated at high pH, leaving the attached precursor particle less time to migrate over the nanoparticle surface, inducing the substructuring. From the *in situ* SAXS data, we cannot unambiguously determine the fate of the polymer, that may be consumed during nanoparticle growth or released during the crystallization of the precursor particles. We identify step 1, the electrostatic stabilization of the precursor through the polymer, as the critical step, shifting magnetite nucleation from thermodynamic to kinetic control. We do not guarantee, that this scheme includes all structures present in the formation of magnetite nanoparticles in the presence of poly-L-arginine, also, pH-dependent energy barriers, that we identified to be responsible for the solid-to-mesocrystalline transition are colored, which must not imply that other energy barriers are not affected by pH.

5.5.4 Step 3 and 4: Nucleation of Magnetite Seeds

The retardation of the increase in concentration of the precursor structures, visible in all figures showing the evolution of the forward scattering, which temporally correlates with the appearance of solid nanoparticles, suggests that magnetite is formed via a solid-state phase transition from ferrihydrite precursor particles to magnetite seeds. We propose, that this transition is induced when the precursor particles grow to certain maximum size reducing their surface to volume ratio. Below a given S/V ratio ferrihydrite can be considered ase thermodynamically unstable, with respect magnetite thus inducing the solid state transformation.[1] [124] We can envision two mechanisms by which this maximum size is reached: i) step 3 growth of the precursor particles by accretion of ferric oligomers or ii) step 3' aggregation of two precursor particles. While for measurements at 25°C the growth process is to fast to be temporally resolved, *in situ* SAXS measurements performed at 15°C, slow down the reaction to the extent that growth of the precursor a continuous particle is suggested. Due to the ultra-low iron concentration at early stages of the synthesis, we suffer from low scattering intensity, and we thus lack reliable data. We thus abstain from an unambiguous evaluation of this growth step.

5.5.5 Step 5: pH Dependent Nanoparticle Growth

Consecutively to the seeding phase, we observe the growth of magnetite nanoparticles and presume, that the retardation of the increase in precursor concentration is not only due to the formation of seeds, but also due to their consumption by the growing magnetite nanoparticles.

From the temperature-dependent *in situ* SAXS measurements we determined the activation energy for the growth step to be 20.7 kJ/mol, which is on the order of the activation energy found for the formation of magnetite in the absence of additives at pH 9.[113] As the growth of the naked nanoparticles with similar activation energy was reported to be kinetically controlled, we proceed to model our particle growth according to literature.[113] Assuming an isotropic growth, the evolution of particle size via the attachment of monomers of volume, V_0, and concentration, $c(t)_0$, can be quantified by,

$$\frac{dr}{dt} = \frac{V_0 c_0 k(r,T)}{4\pi r^2} = \frac{V_0 c(t) k(r,T)}{4\pi r^2} \tag{5.5.1}$$

where $k(r,T)$ is the reaction rate. Envisioning the attachment step of a precursor particle to the growing nanoparticle surface as a 2 step process, we identify two rate limiting factors. Either the diffusion,k_{diff}, of the precursor particle to the nanoparticle may be the rate limiting step, or the reaction at the attachment site, k_{reac}. In the case of reaction limited growth, we will find

---

[1] No data available for magnetite. We assume that activation energies are in the order of maghemite and hematite. Due to addition of polymer a theoretical quantification remains difficult

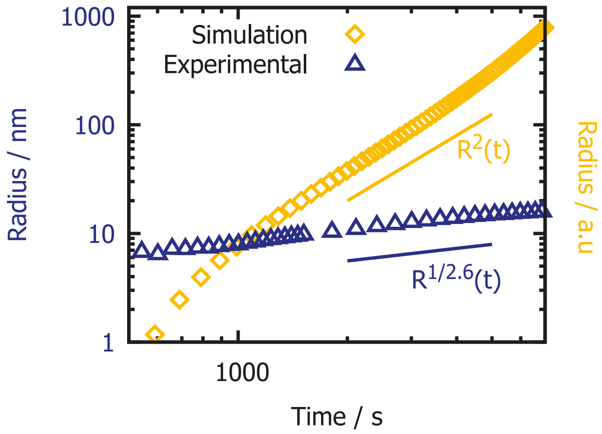

Figure 5.11: Experimentally determined radial growth of magnetite nanoparticles in the presence of poly-L-arginine compared to a reaction limited growth that has been simulated based on experimentally obtained parameters. We find that the simulation –even though not in absolute numbers– exhibits a much faster growth compared to the experiment.

$k_{reac} << k_{diff}$. Concluding that the nanoparticle growth is likely reaction limited, we thus substitute $k(r, T)$ into Equation (5.5.1) with:

$$k_{reac} = 4\pi(r + r_0)^2 k_o e^{-E_A/k_B T} \tag{5.5.2}$$

We assume a homogeneous distribution of precursor particles that bind to the growing nanoparticles with a frequency, $c(t)k_0$, where c(t) is the precursor concentration, incrementing the nanoparticle size by $V_0 \approx \sqrt[3]{R_G^{D_{f,pre}}} = \sqrt[3]{5\text{nm}^{2.2}} = 3.2 \ \ \text{nm}^3$ corresponding to a condensed ($D_f = 3$), crystallized precursor particle. As the pre-exponential factor, k_0, cannot be quantified, we also abstain from a precise quantification of the precursor concentration and use the experimentally obtained forward scattering instead. This justifiable for a constant volume of precursor particles and a constant scattering length density contrast for the precursor particles. We thus model the particle growth in arbitrary units of size in Figure 5.11 and find, that the simulated growth exponent exceeds the experimentally obtained one by a factor 6, indicative of much faster growth, then experimentally observed. There must hence be other effects, or further growth steps additional to the simple description of diffusion and reaction, that retards the nanoparticle growth, decreasing the experimentally observed growth mechanism. Taking a step back and looking at the reaction limited growth rate, we find that we have excluded the pre-exponential factor, k_0, from any quantitative evaluation. It reflects the temperature-independent entropic contribution to the activation barrier, ΔG_{crit} as

$$e^{\frac{-\Delta G}{k_B T}} = e^{\frac{-\Delta H}{k_B T}} \cdot e^{\frac{\Delta S}{k_B}} = k_0 \cdot e^{\frac{-\Delta H}{k_B T}} \tag{5.5.3}$$

we thus propose, that the limitation of the nanoparticle growth does not necessarily come from the enthalpic contribution to the free energy activation barrier, but may be limited by entropy. Similarly to the aggregation of charged solutes[125], we infer, that the nucleation of precursor particles at the nanoparticle interface is driven the gain in entropy associated with the release of hydration water and polymer upon crystallization of the precursor, similar to what has been reported for aggregation of calcium phosphate.[126] Thus, numerous effects, including counter ion concentration, polymer persistence length, and surface charge density of the polymer and the nanoparticles should significantly influence the energy landscape of our reaction. With the intention the explain the effect of pH on the nucleation rate, we envision that at higher pH precursor are more strongly hydrated and thus release more hydration water upon crystallization, which, in turn, drives nucleation. Therefore one possible explanation for the increase in reaction rates at high alklalinity is the increased release of hydration water at high pH.

Following the line of thought of a reaction limited growth process, another explanation for the pH-dependent kinetics may be possible. We identify the oxolation reaction, shown in the bottom right of Figure 5.10, as the paramount reaction involved in the attachment step. In the following we want to elucidate, how this reaction may be responsible for the inverted dependence of the growth rate on pH and, in parts, the single- to mesocrystal transformation can be explained based on this reaction mechanism. The first step, k_R in Figure 5.10, in this nucleophilic two-step associative (presence of transition state) reaction mechanism (S_N2) controls the kinetics of the precursor attachment and thus the rate of nanoparticle growth. The first step involves the formation of a hrydroxo bridge via the nucleophilic attack of a hydroxy-oxygen to a partially positively charged iron. The presence of hydroxide ions increases the nucleophilicity of the oxygen (see transition state Figure 5.10 bottom right) and thus the addition step, k_1, is increasingly catalyzed at higher alkalinity. We suggest this to be the pivotal step explaining the inversion of k with increasing pH. In the absence of additives, thermodynamics governs the nucleation, while kinetics takes over when poly-L-arginine is added. As introduced earlier, the thermodynamic and the kinetic energy barrier, governing the growth rate, are unequally proportional to the pH, thus explaining the effect of size inversion with pH.

The second step of the oxolation mechanism, however, is not favored by an increase in pH. For the final oxo bridge to be formed, an aquo leaving group in the ligand field of iron is required. With an increase in pH the deprotonation equilibrium constant favors the existence of hydroxy over aquo ligands. In the balance of the reaction, we need one aquo leaving group for each oxo bridge formed, thus even though the first addition step is heavily catalyzed at alkaline conditions, the number of further bonds that can be formed within some time interval decreases. Let us keep this in mind for the final step of nanoparticle formation, which conceptualizes the transition from spherical single crystals to sub-structured mesocrystals between pH 10 and 11.

5.5.6 Step 6 and 7: pH Dependent Wetting Behavior and Crystallization Kinetics Induce Mesocrystal Formation

After the first bond formation between the growing nanoparticle and the precursors in the attachment step, we necessarily need the formation of additional bonds and an inherent creation of a new interface between precursor- and nanoparticles.

If we assume the precursor particle to be a liquid, which approximately holds due to its high dynamics and solute like nature[120], we can regard step 6 of the precursor/nanoparticle interaction as a surface wetting process by the liquid-like precursor. We can thus define the interaction as a balance between cohesive and adhesive forces that may be affected by the surrounding pH, using the simplified Young's equation for planar surfaces:

$$\Delta\gamma_{Mt,H_2O}(pH) = \Delta\gamma_{Mt,pre}(pH) + \Delta\gamma_{H_2O,pre}(pH)cos(\theta(pH) \tag{5.5.4}$$

The surface energies of the precursors and the magnetite nanoparticle, are doubtlessly different and experimentally not accessible, therefore the surface tension between water and magnetite (γ_{Mt,H_2O}), water and precursor ($\gamma_{H_2O,pre}$) and magnetite precursor ($\gamma_{Mt,pre}$) not quantifiable and thus we cannot obtain an absolute value for contact angle,θ:

$$\theta = cos^{-1}\left(\frac{\gamma_{Mt,H_2O} - \gamma_{Mt,pre}}{\gamma_{H_2O,pre}}\right) \tag{5.5.5}$$

However, postulating that an effect of pH would equivalently effect the surface energy of magnetite and ferrihydrite but not the one of water, the dependence of the contact angle with pH,$\theta(pH)$, simplifies to:

$$\theta(ph) \approx cos^{-1}\left(1 - \frac{\Delta\gamma_{Mt,pre}(pH)}{\Delta\gamma_{H_2O,pre}(pH)}\right) \tag{5.5.6}$$

Considering, that an increase in pH would equally deprotonate surface hydroxl groups of magnetite and ferrihydrite, we can deduce an increase in surface tension between the progressively equally charged magnetite and ferrihydrite, while the surface tension between magnetite and water decreases.[127] We thus find an increase in the contact angle between magnetite and precursor particles with an increase in pH. In its limits, we thus propose complete surface wetting for the interaction at low pH and no surface wetting at high pH, as schematically shown in Figure 5.12. Following this concept of increasing interfacial energy with increasing pH we predict, that the surface tension and thus the contact angle at pH 12 is increased to an extent, that no magnetite/precursor addition will take place. Thus precursor particles condense upon themselves, resulting in $\approx \sqrt[3]{R_G^{D_{f,pre}}} = \sqrt[3]{5\text{nm}^{2.2}} \approx 3.2\text{nm}^3$ sized, discrete magnetite nanoparticles.

Additionally, we find the solid phase transition kinetics in step 7 to accelerate with increasing pH, while bond formation via oxolation is hampered. This results in reduced time for the precursor par-

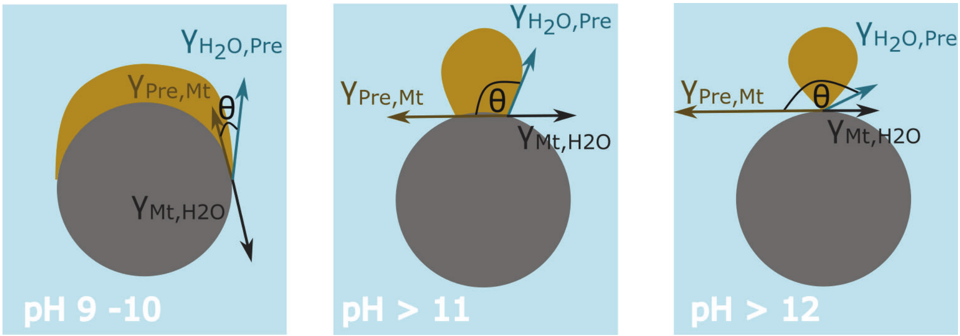

Figure 5.12: Scheme of the proposed influence of precipitation pH on the wetting behavior of precursor particles on a magnetite surface. With an increase in pH surface tension between water and magnetite ,(γ_{Mt,H_2O}), as well as water and precursor, (γ_{Pre,H_2O}) decrease, while the tension between precursor and magnetite increases ($\gamma_{Mt,Pre}$), resulting in a higher contact angle at increased pH. We thus propose a high wetting at pH 9 and 10 and low wetting at pH 11, while non-wetting behavior at pH 12 inhibits the growth of nanoparticles.

ticles to equilibrate at the surface of the growing nanoparticle and together with the proposed high contact angle induces the formation of a substructured mesocrystal (Structure A in Figure 5.10). In contrast, the high wetting at pH 9 and 10 in combination with the slow solid-state transformation, leave enough time for the precursor particle to equilibrate around the growing crystal, forming spherical, solid crystals. As this solid-state transformation can be characterized as a homoepitaxial growth, meaning that the newly formed crystal adapts its crystallographic register with respect to the substrate, we obtain single crystals, with single crystal properties at all precipitation pH.

5.5.6.1 The Proposed Mechanism Explains a Majority of Observations

Additionally to the inverted growth rate with respect to pH as well as the solid-to-mesocrystal phase transition, we are confident, that the above-proposed mechanism can also explain the existence of an -under the given conditions- ideal feeding rate and ideal polymer concentration, while the molecular weight does not have any significant influence on the structure of the precursor particles nor the final morphology of the nanoparticles.

The size of the precursor particles is persistent during all experiments and thus may only be determined by the precursor's thermodynamic stability[128]. As the polymer is only present to stabilize but not necessarily scaffold this structure, there is no influence of the polymers molecular weight, above a certain size threshold of 16 monomers, shown later in section Section 5.9. The number of precursor particles will thus be determined by the feeding rate and the amount of polymer present to stabilize them. However, if too much polymer is present, we could assume that attachment sites at the surface of the nanoparticles will be blocked, retarding, in turn, nanoparticle growth. Thus there should be an ideal ratio of the concentration of polymer and feeding rate of iron.

Proposing the multistep growth mechanism, including attachment, wetting, and a solid-state phase transition, we assume that this cascade of reactions to must be completed for further growth to appear. The growth exponent of 2.6, which is slow compared to reaction and diffusion-limited growth, may be the quantification of this growth retarding multi-step process.

5.6 STEM Tomography for Structural Investigation

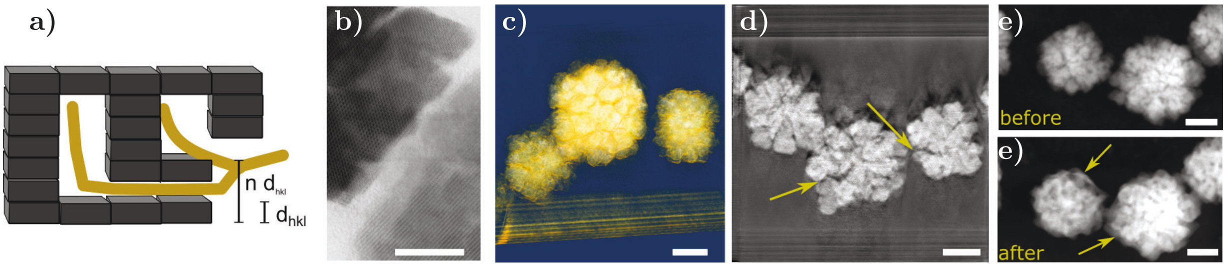

Figure 5.13: a) Schematically shows how mesocrystals can still exhibit single crystal coherent diffraction throughout the particle volume, even though physical gaps are present. When the gap width is a multiple n of d_{hkl}, coherent diffraction is not significantly affected. Particles imaged solely in transmission mode, appear to be made out off small platelets, while the volume rendered 3D view c) shows bulges on the surface of the nanoparticle. The excerpt of the calculated z-stack through the mesocrystals in d) reveals gaps (yellow arrow) that reach as far as into the center of the mesocrytal (green arrow) and give the impression that the solid magnetite is grown from the center, as predicted by our mechanism. In an attempt to locate the polymer via nitrogens characteristic x-ray emission using STEM EDX tomography, the particles suffered severe beam damage during the 8 h measurement, indicated by the yellow arrows in the before e) and after f) STEM image.

An important question left to answer concerns the fate of the polymer. Especially in the case of the mesocrystal one may wonder if the polymer is internalized or released after the attachment step of the precursor. This will have important implications for the function of the polymer ranging from scaffolding, structural support, if internalized, to a catalytic functionality, where the polymer is only necessary to stabilize the precursor and is released after the attachment. We were thus aiming to localize the polymer in 3D within the mesocrystal using STEM EDX tomography, discriminating the polymer from the nanoparticles by its characteristic nitrogen x-ray emission.

We thus set up STEM measurements from 0° to -65° and from 0° to +63° including STEM and EDX measurements at each angle with separate drift correction for the respective measurement. This resulted in a consecutive beam exposure of the sample for more than 8 hours, inducing strong beam damage as indicated by the arrows in Figure 5.13 c) and d). Long exposure for the EDX measurements was especially necessary as the N K-tα edge was overshadowed by the dominant intensities of the O K-α and C K-α. Due to these limitations we did not succeed to obtain an elementally resolved tomogram.

We thus retrieved and decided to obtain manually focused STEM tomograms to reduce beam exposure. A volume-rendered three-dimensional reconstruction of the magnetite mesocrystals is shown in Figure 5.13 a). We see that the often platelet like looking, Figure 5.13 b), outer parts of the mesocrystal appear now, in the volume-rendered view, as bulges of magnetite. The virtual slice trough the mesocrystal obtained from a reconstructed z-stack of images, shows that these bulges seem to grow from the center of the mesocrystals to the outside leaving gaps between separate bulges, indicated by the yellow arrows in Figure 5.13 b)

5.6.0.1 Discussion

Unfortunately, we were not able to unambiguously locate poly-L-arginine by its characteristic X-ray emission within the particles. However, the 3D volume-rendered reconstruction gives us valuable information about the shape and morphology of the particles, exceeding the possibilities of conventional STEM/TEM, where a 2D projected image is recorded.
Looking virtually inside the particles reveals a centrosymmetric growth and may even reveal the high contact angles of the earlier proposed dewetting of the precursor particles (see Figure 5.13 b)). We find that this morphology fits well into the above-proposed formation mechanism.

5.7 Salt Induced Growth Retardation

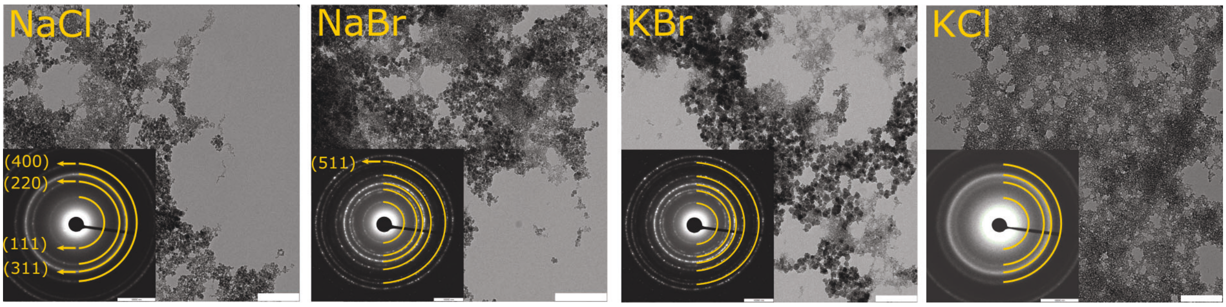

Figure 5.14: TEM images and SAED patterns in the insets of magnetite prepared at pH 11 in the presence of an additional 10 mM salt. Different salts, as indicated in the top of each TEM micrograph, have been added. Scale bars in all images are 100 nm.

All nanoparticle's growth kinetics show slight retardation for late time points. We can only assume that this growth retardation may have been the cause, why Reichel et al. could not resolve the progressing nanoparticle growth based on XRPD measurements of hourly taken samples. Consecutively, no further growth was foreseen in these earlier models after the agglomeration step and particles were thought only to increase their number density. However, concerning the presented *in situ* SAXS data a continuous and continuously progressing nanoparticle growth is undeniably apparent. The growth retardation after approximately two hours, however, can be explained looking at the results obtained from synthesizing magnetite mesocrystals at pH 11 in the presence of an additional 10 mM NaCl, NaBr, KBr or KCl. TEM micrographs with corresponding SAED patterns in the inset can are shown in Figure 5.14. The addition of salt inhibits mesocrystal formation, independent of the kind of salt already when the total electrolyte concentration is increased by 10 mM. All SAED patterns show diffraction rings of an inverse spinel structure with crystal plane spacings of magnetite. However, the strong broadening of the rings for particles prepared in the presence of KCl and NaCl suggest tiny grain sizes, as it is also evident in the TEM micrographs.

5.7.0.1 Discussion

Co-precipitating ferrous and ferric chloride we obtain 8/3 mol of NaCl for each mol of Fe_3O_4 formed. Under perfect conditions, a reaction volume of 10 mL and an iron solution addition rate of 1 µL/ min we thus increase the total NaCl concentration in the reaction by 1.6 mM per hour and are thus, after 2 h of synthesis (or *in situ* SAXS measurement), at 30 % of the salt concentration known to completely inhibit mesocrystal formation. As this process will be continuous, we propose that the slight growth depression observed in the SAXS data can already be accounted to the increased concentration of NaCl. This may also explain, why it has not been possible to obtain magnetite mesocrystals at pH 12. Here, compared to pH 11, the Na^+ concentration is already 10 mM higher due to the increase in pH. We further point out that different salts inhibit Fe_3O_4 formation more or less strongly. Based on visual evaluation of the TEM images and diffraction patterns in Figure 5.14 we find, that the ability of the salts to inhibit mesocrystal formation complies with the Hofmeister series[129,130] and we can sort the salts by increasing retardation ability as NaBr<KBr<NaCl<KCl. This effect suggests that the retardation in mesocrystal (and any other poly-L-arginine/magnetite particle) formation can be attributed to a hindered interaction of the precursor iron phase with the polyelectrolyte. Thus, the polyelectrolyte fails to stabilize the precursor phase, and ”standard” magnetite, similar to magnetite precipitated in the absence of any additive, is formed.

5.8 Improving Synthesis by Rational Design

Using the knowledge on the formation of the poly-L-arginine/magnetite mesocrystals, we strive to advance the properties of our system by rational design. We now know that the mesocrystal growth is continuous and mediated via polymer-stabilized precursor iron phases and we know that this stabilization is inhibited at an elevated concentration of counter-ions. We thus propose that an infinite crystal growth can be achieved, when the critical salt concentration will not be exceeded. Thus in order to extend the time until the threshold counter ion concentration is reached we could i) increase the reaction volume ii) decrease the addition rate of iron solution, iii) decrease the concentration of the added iron solution and iv) increase the temperature. However, a decrease of the iron concentration below a threshold value will inhibit magnetite formation and favor the formation

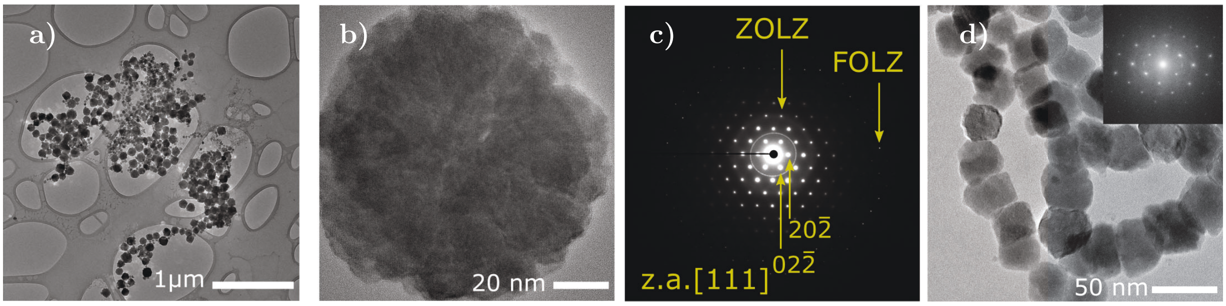

Figure 5.15: a) Overview of magnetite/poly-L-arginine grown for 24 h at altered synthesis conditions. The HRTEM image of a single particle in b) shows substructured morphology even at a size of ≈140 nm. c) Electron diffraction along the [111] zone axis of the individual particle indicate single crystallinity. The intersection of the Ewald sphere with the zero$^{\text{th}}$ (ZOLZ) and first (FOLZ) order Laue zone are visible and marked by the yellow arrows. Similarly, particles can be grown at pH 10 for 24 h at altered conditions d) obtaining particles with diameters of up to 50 nm, with a solid, single crytalline (FFT upper left) morphology.

of less dense and more hydrated iron phases.[2]

Figure 5.15 a) and b) shows TEM micorgraphs of poly-L-arginine/magnetite particles grown for 24 h at pH 11 and pH 10, Figure 5.15 d). We increased the total reactor volume to 60 mL, and the concentration of the added iron solution decreased to 0.5 mmol. The addition rate of 1 µL/ min is the lower limit of the dosing unit and was thus kept. An overview of the synthesized particles shows that a significant particle population with an average diameter above 100 nm for pH 11 and around 50 nm at pH 10 can be obtained. An HRTEM image of a single particle shows that substructured morphology is retained even at larger sizes. Single crystal electron diffraction along the mesocrystals [111] zone axis in Figure 5.15 c) and FFT's of a single nanoparticle Figure 5.15 d) top rights confirms single crystallinity of both mesocrystals and solid, spherical nanoparticles obtained at pH 10.

The exact physico-chemical conditions at which magnetotactic bacteria produce magnetite nanoparticles are unknown. It is, however, certain that the precipitation pH inside the bacterium is only slightly alkaline, still, they produce large particles above the stable single domain threshold. Pursuing the initial objective to biomimitically mimic the nanoparticle growth, we synthesize magnetite nanoparticles at pH 9 using the adapted synthesis protocol. TEM images of the synthesized particles, shown in Figure 5.16, show individual, spherical particles well beyond the size threshold for stable single domain magnetite (20 nm).

5.8.0.1 Discussion

Our ability to grow mesocrystals beyond the previously reported size threshold of 40 nm[65], further supports the idea that both meso-and single crystals are formed by the consecutive addition of non-crystalline precursor iron phases. We anticipate that any particle size could be synthesized if

---

[2] unpublished work J. Baumgarnter

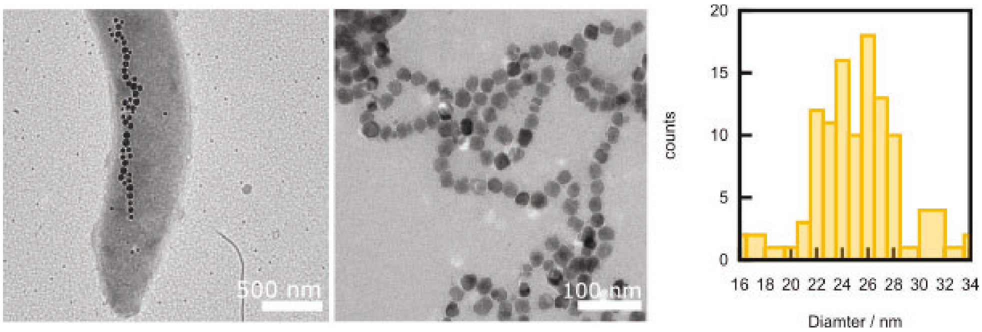

Figure 5.16: TEM image of MSR-1 that uses stable single domain magnetite nanoparticles aligned along a protein filament for magnetotaxis. Using the adapted synthesis protocol, particles above the size threshold for stable single domain particles were synthesized at conditions (pH=9) similar to the growth conditions prevalent inside the bacteria.

the precipitation volume was further increased. However, switching from the cone-shaped reactor geometry used by the Metrohm to a cylindrical beaker, we were not able to precipitate magnetite, but yielded goethite, an oxidized polymorph of magnetite.

We assume that either the level of oxygen was too high or that fluid dynamics around the iron solution inlet plays an important rule on local iron concentration, having a significant impact on the iron phase formed.

5.9 Molecular Weight Dependence

As mentioned in section Section 4.2.1 any adsorption comes with a gross entropic penalty.[131,132] Together with an enthalpic contribution, this energy balances the poly-L-arginine/pre-nucleation cluster interaction and can be expected to crucially depend on the poly-L-arginine's polymerization degree. We thus hypothesize that, equally, the ability to stabilize precursor structures, and thus to interfere in magnetite nucleation, depends crucially on the polymer length. Also, the persistence length of a polymer is expected to influence the energetic landscape of adsorption equally.[133] However, since tuning the chain length of a polymer is more easily accessible then a consistent change in persistence length, we prepared magnetite mesocrystals at pH 11 in the presence of short and defined poly-L-arginine with monomer numbers of 2, 4, 8, 16 and 32.

An excerpt of the x-ray reflectometry measurements (D8 diffractometer) showing the 311 reflection is shown in Figure 5.17. Due to an unknown instrumental peak broadening, we refrain of calculating particle sizes and pursue in a qualitative discussion of the peak broadening assuming a constant instrumental peak broadening for all measurements. The full width at half maximum (FWHM) for all molecular weights were determined using a pseudo Voigt function and are listed for the different numbers of monomer units in Figure 5.17 a). As reference sample magnetite prepared in the absence of any additive at identical conditions was used (# mono = 0).

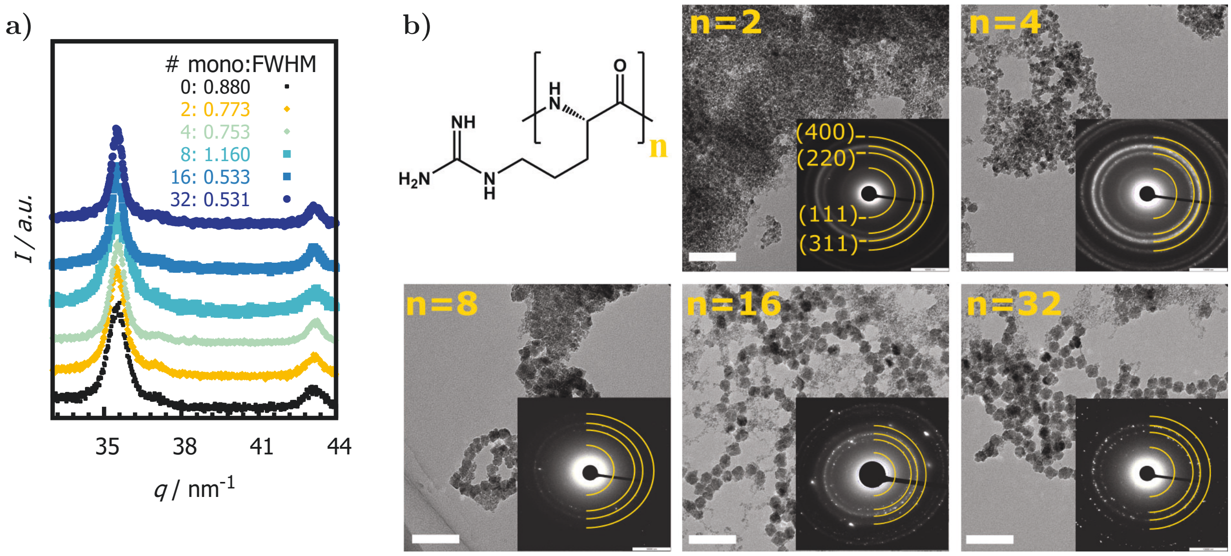

Figure 5.17: a) Excerpt from azimuthally integrated XRDP measurements of particles prepared in the presence of poly-L-arginine of with different number n of monomer units. The full width at half maximum (FWHM) of the 311 reflection was obtained from a pseudo Voigt peak fit. With the increasing number of monomer units (except for n=8), the FWHM decreases, indicating an increase in particle size. This trend is also well visible in the TEM images, where additionally the presence of mesocrystals for n≤16 is apparent. SAED measurements, seen in the lower right inset of each TEM micrograph, indicate that Fe_3O_4 is formed for all n, except for n=8.

With an increasing molecular weight of poly-L-arginine (except for n=8) we find a decrease in the FWHM of the crystallites and can thus infer an increase in particle size with increasing molecular weight following an exponential decay as shown in Figure 5.18. Complementary TEM measurements show representative images of the formed particles. From visual evaluation, we find that measocrystals are only formed for polymer length longer than n=16 monomers. The SAED patterns shown in the bottom left inset of each micrograph confirm the existence of an inverse spinel structure with lattice springs complementary to magnetite.

5.9.0.1 Discussion

From *in situ* SAXS measurements we have learned that the crucial impact of poly-L-arginine on the formation of magnetite is the stabilization of transient, metastable iron precursors. Intuitively, the polymer needs to adsorb to the precursor's interface for the stabilization to occur. Any adsorption results in a loss of degrees of freedom of the adsorbate which, in turn, goes in handy with adsorption opposing loss in entropy. Comparing now the degrees of freedom of n x m monomers and with a polymer of n monomers dissolved in a unit volume, we find an intrinsic loss of degrees of freedom for the polymer. In turn, we have thus a smaller entropic penalty for the adsorption of a m_n polymer compared to the adsorption of n monomers. Following that thought, we also propose that the

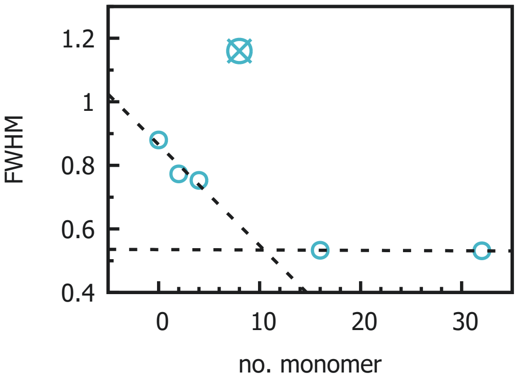

Figure 5.18: Full width at half maximum of the 311 magnetite reflection plotted as a function of the number of monomers per oligomer. The decrease of the FWHM with an increasing number of monomers is evidencing an increase in particle size.

adsorption of x m_n polymers is less favored compared to the adsorption of a $m_{n \cdot x}$ polymer. We thus propose that longer polymers should be more suitable to stabilize the metastable precursors, thus shifting more and more the formation of magnetite from a classical to a non-classical mechanism, which increases the growth rate.

These results may have important implications for biomineralization, where many processes are controlled through the stabilization of meta-stable precursor phases from charged bio-macromolecules, proteins and trans-membrane proteins. How their ability to change conformation and thus loose degrees of freedom may influence biomineralization processes, has not been debated so far but may play an important role.

5.10 Conclusion

Using *in situ* small angle X-ray scattering, we followed the co-precipitation of ferrous and ferric chloride in the presence of poly-L-arginine. Due to the ultra-low iron concentration in the initial stages of the synthesis a 3$^{\text{rd}}$ generation high brilliance synchrotron X-ray source was necessary to obtain a sufficiently high scattering signal. However, the ultra-low concentration also ensured that any species involved in the reaction would not correlate in space with any other species so that we were able to separate their scattering contributions based on an analytical scattering model. Based on this model, we were able to identify a low-density iron species with a gyration radius of 5 nm from which the magnetite nanoparticles grow. Further, we were able to extract the radial growth, the concentration of the nanoparticles, and that of the precursor structures. Kinetic approaches to determine the growth mechanism failed, as neither reaction or diffusion limited growth, nor a growth based on Ostwald ripening could be identified as the prevalent mechanism of nanoparticle formation.

Referencing the existing theories of biomineralization, charged macromolecules or counterions can shift nucleation mechanisms from a thermodynamic to a kinetic control, we developed a comprehensive mechanism that is able to explain: i) the phase transition from spherical to substructured mesocrystals, due to a decrease in wettability with increasing pH and a retardation of the second step step in the addition oxolation reaction; ii) the inversion of the effect of pH on the nanoparticle growth rate, compared to magnetite formed in absence of additives due to the catalytic effect of hydroxide ions on the first step of the oxolation reaction and iii) the existence of an ideal polymer concentration and feeding rate to increase the growth rate of nanoparticles. We have further identified the kinetic stabilization of the low-density, metastable iron precursors by poly-L-arginine to be the pivotal step in the fundamental alteration of the co-precipitaion of ferrous and ferric chloride.

Realizing that the nanoparticle growth is continuous and continuing, and only retarded by a threshold counter-ion concentration, we altered the synthesis parameters to obtain single crystal magnetite mesocrystals with sizes beyond 150 nm.

Chapter 6

Substituting poly-L-arginine

Summary Using *in situ* SAXS to study the co-precipitation of ferrous and ferric chloride in the presence of poly-L-arginine we demonstrated how the formation mechanism is shifted from thermodynamic to kinetic control. This mechanistic shift enables us to prepare magnetically advanced, colloidally stable magnetite nanoparticles. Precise knowledge about the mechanism gave us exceptional control over particle size, size distribution, and particle morphology. Identifying the electrostatic stabilization of metastable iron precursors particles as the crucial tool, we demonstrate here, how more sustainable and renewable strong polycations can substitute poly-L-arginine. We employ HR(TEM) and synchrotron XRPD to determine size and morphology of magnetite nanoparticles prepared at different pH in the presence of such strong polycations and compare the results to particles prepared in the presence of poly-L-arginine. Time-resolved XRPD studies suggest a consistent formation mechanism distinct to all charged polycations at the pH of magnetite precipitation. Unraveling that polycations can generically be used to alter the nucleation pathway of the co-precipitation of ferrous and ferric chloride, we have additionally improved the sustainability of the synthesis, using cheaper and renewable polymers, that can be produced on a metric ton scale, to obtain advanced magnetic nanomaterials.

6.1 Introduction

Nanomaterials bridge, due to their size, the transition between atoms and their bulk material counterparts. As a consequence, their properties are neither that of the bulk materials nor that of single atoms but could be best described as a collective atomistic behavior, constrained by the size of the particle. Due to this constraint, properties of nanoparticles are thus heavily dependent on their size and can, in turn, be controlled through the control of the particle dimension and morphology. Classic examples of this phenomenon are the tunable localized surface plasmon resonance in noble metal nanoparticles[134–136] or the quantum size effect in semi-conductors[137]. Analogously, we learned that the properties of magnetite change from superparamagnetic to single domain or multidomain ferrimagnetic with an increase in size.

We have demonstrated how to exert control over magnetite nanoparticle's morphology and size at ambient pressure and temperature merely by changing the precipitation pH with the addition of poly-L-arginine.[138] We have concluded in chapter Chapter 5 that this control was possible, by shifting the nucleation of magnetite from a thermodynamically to a kinetically controlled mechanism.

Acknowledging the environmentally friendly conditions of our synthesis protocol, the use of poly-L-arginine as an additive is, however, somewhat costly. In order to find cheaper alternatives, we turned our attention to strong polycations. While exploring the ability to reduce the price and ameliorate the ecological footprint of our synthesis, we concurrently pursue the question, if the ability of poly-L-arginine to intervene in magnetite nucleation is specific to this polymer or can if it can be generalized to all polycations.

Therefore we aim to substitute polyarginine by other strong polycations and reproduce the effect on magnetite's growth kinetics, the dependence of the size on pH, the morphological transition at strongly alkaline conditions.

6.2 Strong Polycations

Intending to find alternatives for the rather expensive polymer, poly-L-arginine, we identified the positive charge of poly-L-arginine as the main factor necessary to be present in any substitute. With an unusually high $\mathrm{pK_a}$ that has been reported to be between 12 and 13.8[139] for monomeric arginine, the polymer is completely charged even at the highest precipitation pH of 11. There are only few other monomers (to our knowledge) that exhibit a similarly high $\mathrm{pK_a}$. We thus turn our attention to strong polycations that are positively charged independently of the pH. A residue that

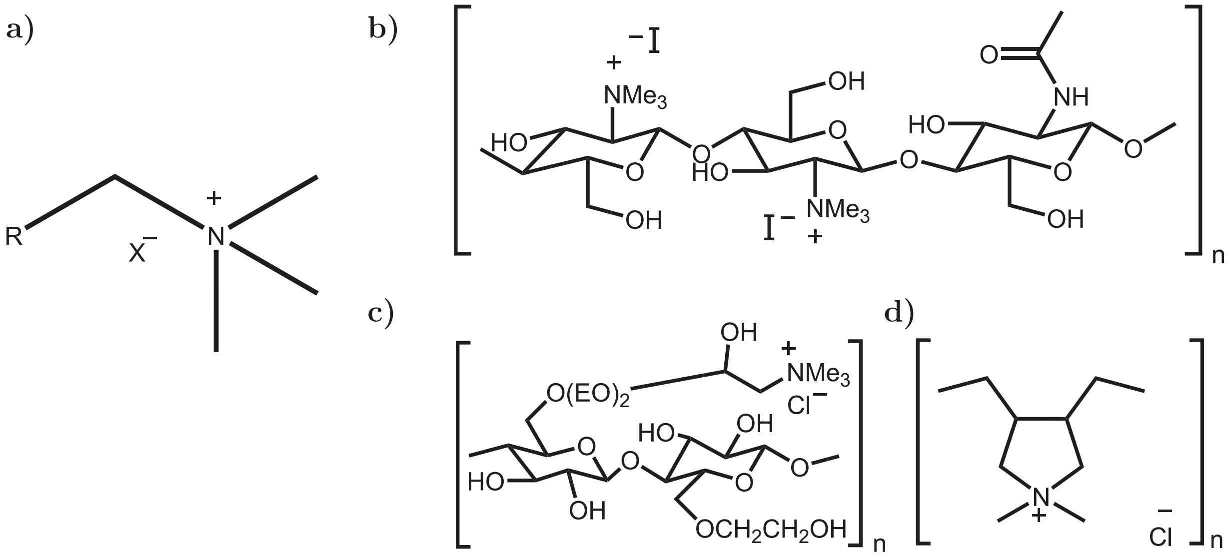

Figure 6.1: Structural motive for strong polycations based on quaternary amines a). Following this motive JR-400 b), quaternized chitosan c) and d) Polydiallyldimethylammonium chloride (PDADMAC) where used to substitute poly-L-arginine in the co-precipitaion of magnetite.

can impart this pH-independent charge is a quaternary amine, shown in Figure 6.1 a). They are synthetically accessible via the quaternaryzation of ternary amines using MeI at high pH and low temperatures, following the protocol by Menshutkin. [cite] Based on this reaction JR-400 Figure 6.1 b) and quaternaized chitosan Figure 6.1 c) were obtained. In contrast to the post quaternization of JR-400 and chitosan the monomer diallyldimethylammonium chloride (DADMAC) from which PDADMAC Figure 6.1 is polymerized, is in itself a strong cation. There are numerous advantages of these substitutes compared to poly-L-arginine. The low costs for PDADMAC, a regularly used polycation[140,141], is approximately a millionth of that of poly-L-arginine, while JR-400 is an industrially produced hair conditioner and thus even cheaper. Chitosan, in turn, is extracted from crustacean waste and has thus the best ecological footprint of the polymers used in this study.

6.3 Results

6.3.1 Quaternized Chitosan

We here show the effect of these polymers on the final size and morphology of magnetite prepared in the co-precipitation of ferrous and ferric chloride in an identical fashion to the protocol used for poly-L-arginine. Using synchrotron-based XRPD, we explore the effect of pH on the final particle size for pH 9–11.5 in increments of 0.5. We grew particles in the presence of 0.1 $\mathrm{mg\,mL^{-1}}$ polymer

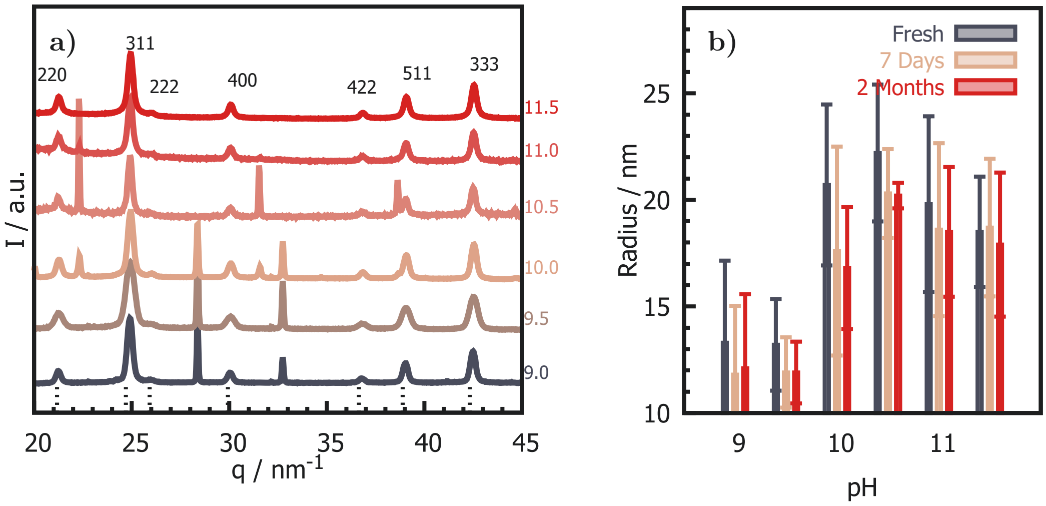

Figure 6.2: a) Azimuthally integrated XRDP measurements of particles prepared between pH 9 and 11.5 in increments of 0.5 in the presence of 0.1 $\mathrm{mg\,mL^{-1}}$ chitosan. Reflections were indexed according to the crystallographic structure of magnetite. Additional reflections that cannot be attributed to magnetite originate from residual NaCl crystals. Particle sizes in b) were calculated from the FWHM of the magnetite 311 reflection. Errorbars were calculated from the mean of triplicates. To elucidate ageing effects, samples were taken freshly after the synthesis, 7 days and 2 months stored under anoxic conditions. A non-significant reduction in particle size due to ageing may be present.

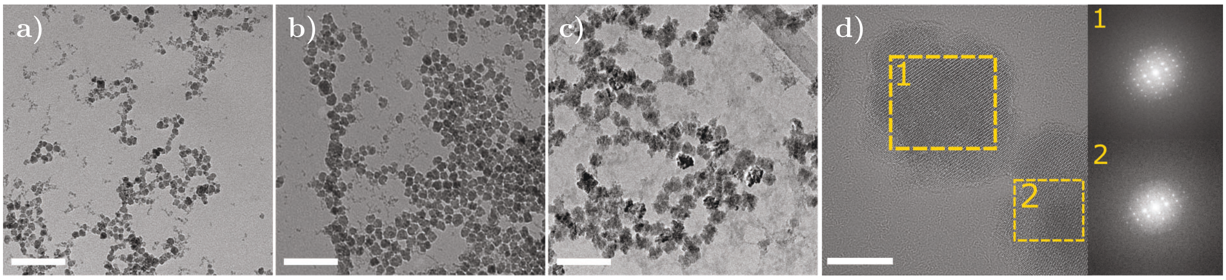

Figure 6.3: TEM images of particles prepared at pH 11 in the presence of 0.1 $\mathrm{mg\,mL^{-1}}$ chitosan show similar chain formation as poly-L-arginine/magnetite and a narrow particle size distribution (scale bar 100 nm). HRTEM images in d) show, consistent with poly-L-arginine/magnetite, a substructured morphology, and single-crystalline coherent diffraction, evidenced by the FFT spot pattern in 1. Crystalline bridges seem to be able to connect particles and induce a correlation in the crystallographic orientation (FFTs 2).

for 2 hours. TEM images were taken from twice magnetically separated and washed aliquots. We calculated particle sizes from the peak broadening of the 311 magnetite reflection using the Scherrer equation and obtained particle size distributions from mean sizes of triplicates. Additionally, XRPD samples were prepared freshly after 2h of synthesis, after seven days and two months of aging under anoxic conditions in order to study their stability.

Figure 6.2 a) shows azimuthally integrated XRPD data of magnetite prepared in the presence of chitosan and aged for two months. We indexed the reflections according to the inverse spinel structure of magnetite. Additional reflections that cannot be attributed to the presence of magnetite, origin from NaCl crystals that are a side product of the co-precipitation of ferrous and ferric chloride in the aqueous sodium hydroxide. Calculated particle sizes in dependence of pH are shown in Figure 6.2 b). Similarly to poly-L-arginine we find an increase in particle size with increasing pH until 10.5 after which the final particle size is not affected by a further increase in pH. The size distribution within triplicates is –compared to poly-L-arginine– significantly increased. We attribute this to difficulties with the synthesis setup prevalent during this experiment. A repetition, however, was not possible due to the unavailability of the XRPD synchrotron beamline. Figure 6.3 a) to c) provides representative TEM images of particles prepared at pH 9, 10 and 11, respectively. Similar to poly-L-arginine/magnetite particle morphologies change from a spherical single-crystalline particle, obtained at pH values below 11, to mesocrystalline, substructured particles at more alkaline conditions. This equally sudden change in morphology hints at a similar mechanism for the formation of magnetite in the presence of quaternized chitosan compared to poly-L-arginine.

6.3.2 JR-400

Magnetite in the presence of JR-400 –the industrially synthesized hair conditioner– was prepared according to the protocol described above. Azimuthally integrated XRPD diffractograms in Figure 6.4 were indexed in agreement with the inverse spinel structure of Fe_3O_4. Residual reflection can be attributed to the existence of small sodium chloride crystals. Particle sizes are shown in dependence of precipitation pH in Figure 6.4 b). Again, size distributions were calculated from the mean size of triplicates of aliquots taken after the synthesis and seven days or two months after the synthesis, while the product was stored under anoxic conditions in the fridge. For most pH values (except for 11) no significant effect of aging time on the particle size can be detected. We can identify a slight increase in average particle size with pH, consistent -but not as significant- with particles prepared in the presence of poly-L-arginine. This increase is only visible in the pH range between 9 and 10.5. For pH 11 we find particles that significantly decrease in size over 2 months and thus are not stable against aging. Particles prepared at ph 11.5 show high standard deviations in mean particle size. It thus seems that the synthesis of magnetite in the presence of JR-400 only yields stable particles in a reproducible synthesis below a pH of 10.5.

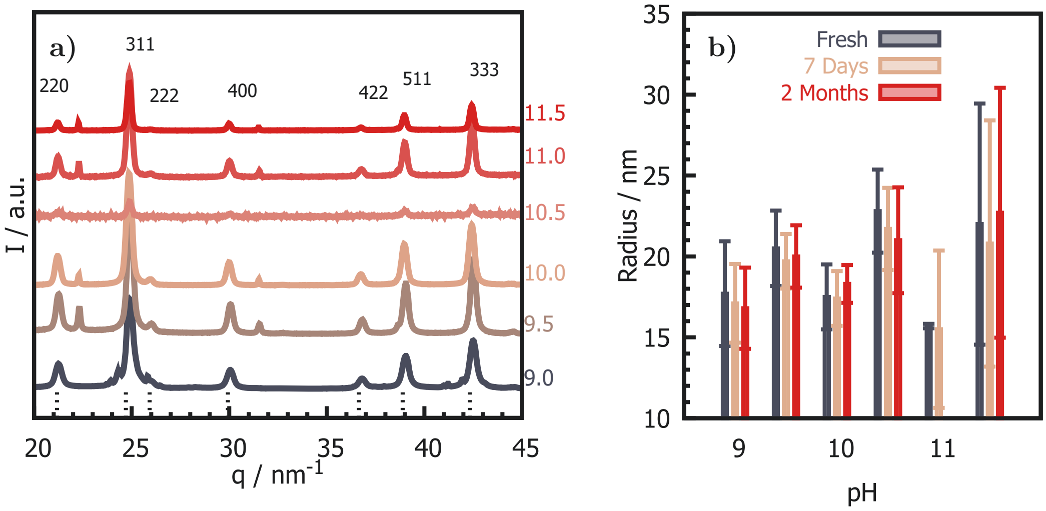

Figure 6.4: a) Azimuthally integrated XRPD patterns of magnetite prepared in the presence of 0.1 $\text{mg}\,\text{mL}^{-1}$ JR-400 at various pH values. Diffraction peaks were integrated according to an inverse spinel magnetite structure. Additional reflections originate from NaCl, a side product of Fe_3O_4 synthesis. Particle sizes b) were calculated from the 311 magnetite reflection from samples that were taken freshly after the synthesis, 7 days and 2 months after the synthesis. Particle size slightly increase with increasing pH. The effect, however, is not as apparent as in poly-L-arginine/magnetite. Particle sizes remain stable over a course of 2 months.

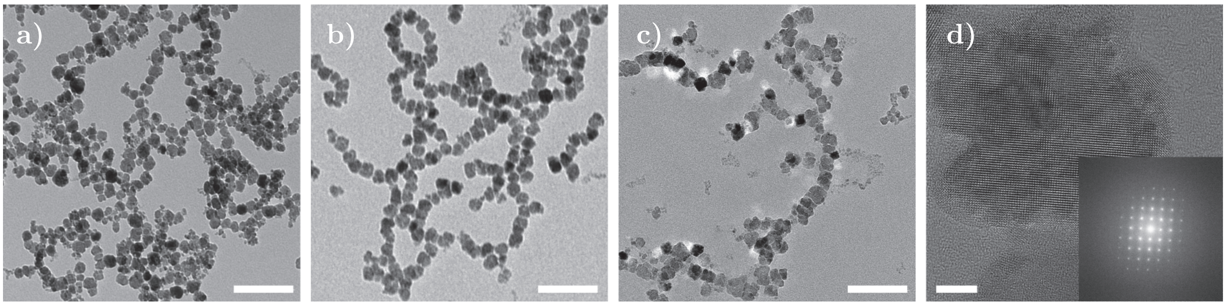

Figure 6.5: Representative low magnification (scale bar 100 nm) TEM micrographs a) to c) of magnetite prepared in the presence of 1 $\text{mg}\,\text{mL}^{-1}$ JR 400 at pH 9, 10 and 11, respectively. HRTEM image (scale bar 5 nm) of particles prepared at pH 11 show a similar substructured morphology as does magnetite prepared in the presence of poly-L-arginine. Single crystallinity throughout the particle is conserved and apparent in the FFT spot pattern (bottom right).

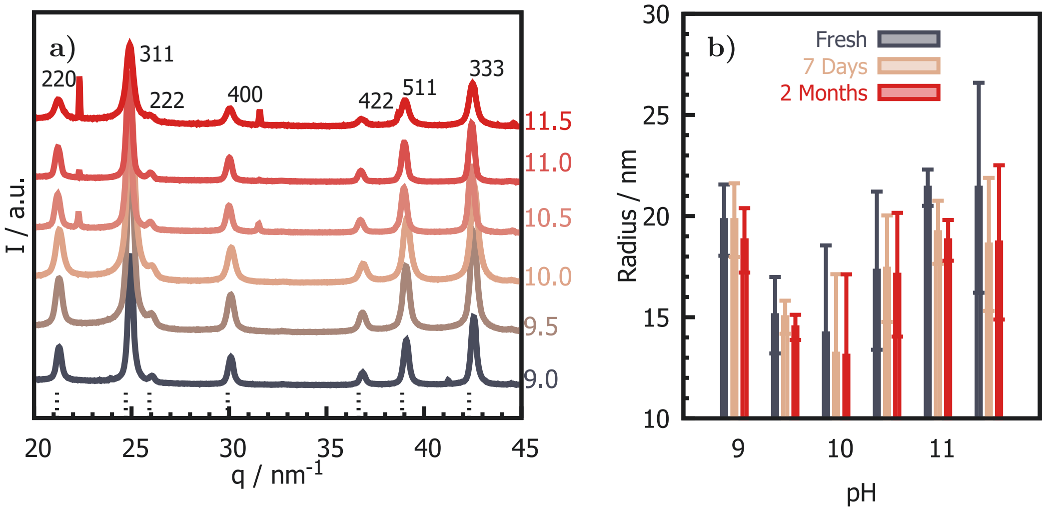

Figure 6.6: a) Azimuthally integrated XRDP measurements of particles prepared in the presence of $0.1\ \mathrm{mg\,mL^{-1}}$ PDADMAC at different pH values ranging from 9 to 11.5 in increamemnts of 0.5. Reflections were indexed according to the crystal structure of magnetite. Particle sizes calculated from the FWHM of the 311 magnetite reflection are shown in b). Particle size distributions were calculated from the mean size of triplicates for samples taken freshly after the synthesis and for samples aged for 7 days and 2 months. Again, non-significant particle size reductions maybe present in the course of 2 months. The particle size follows the pH in a non-monotonic fashion, in contrast to poly-L-arginine/magnetite nanoparticles.

Representative TEM images of particles prepared at pH 9, 10 and 11 are shown in Figure 6.5 a) to c) and reveal –similar to poly-L-arginine/magnetite– a morphological change between pH 10 and 11 from spherical single crystals to substructured mesocrystals. However, similar to chitosan, particles seem to be more strongly substructured revealing larger gaps and a less defined spherical shape. HRTEM images of a particle synthesized at pH 11 in Figure 6.5 d) highlight the rugged morphology. Still, the FFT in the bottom right corner of d) indicates that the crystallographic order is not hampered by the increase in nanoscopic disorder.

6.3.3 PDADMAC

The last polycation tested is PDADMAC. In line with chitosan and JR-400 we measured XRPD -indexed in agreement with the magnetite structure- from which mean particle sizes were determined, both shown in Figure 6.6 a) and b). Size distributions –calculated from the mean size of triplicates– have increased, as compared to polyarginine. Again, this trend is prevalent for all polycations tested. In contrast to magnetite precipitated in the presence of polyarginine mean particle sizes are not consistently increasing with pH. It is visible in Figure 6.6 b) that at pH 9 already comparably large particles of 20 nm are found that decrease to 14 nm when precipitated at pH 10. Between pH 10 and 11.5 the previously reported proportionality of particle size with pH is recognizable and mean sizes increase when the precipitation pH is increased. This non-monotonic pH dependence

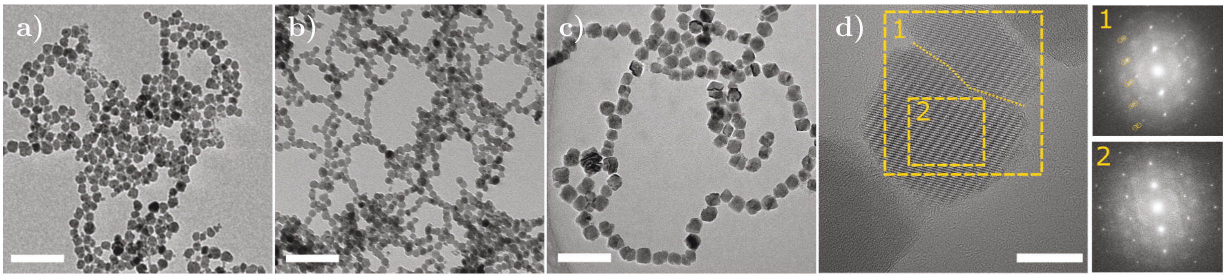

Figure 6.7: Representative TEM micrographs taken from samples prepared at pH 9, 10 and 11 a)-c) in the presence of PDADMAC showing a narrow particle size distribution (scale bar 100 nm). HRTEM image (scale bar 5 nm) of a selected particle show no mesocrystalline, substructured morphology, as compared to poly-L-arginine/magnetite. While most of the particles are solid single-crystals, twinning can occur as indicated by the arrows in FFT 1.

is confirmed visually in TEM for particles prepared at pH 9, 10 and 11 in Figure 6.7 a) to c). Similar to other polycations tested, TEM micrographs of particle prepared at pH 9 and 10 show spherical, single crystalline morphology of magnetite nanoparticles. Remarkably, we do not find substructured, mesocrystalline particles in the co-precipitation of ferrous and ferric chloride at pH 11 in the presence of PDADMAC. Similar to pH 9 and 10 particles are primarily single crystals with a spherical shape. Only few particles are visible, that exhibit a substructure. A HRTEM image of a substrcutured particle is shown in Figure 6.7 d). FFTs of the single crystalline looking particle suggest that twinning has occurred within the particle, indicated by the two arrows emphasizing the splitting of diffraction spots. The twin boundary is indicated by the dotted line in Figure 6.7.

6.3.4 Growth in the Presence of Polycations

In section 5.4.1 we have extensively studied the formation mechanism of magnetite precipitation in the presence of poly-L-arginine using *in situ* SAXS, describing the obtained time-dependent parameters with appropriate kinetic growth models. Not having the possibility of regularly accessing a 3rd generation synchrotron SAXS beamline, we turned to study the mean size of magnetite precipitated in the presence PDADMAC, JR-400 and chitosan at different pH on dried samples using synchrotron XRPD. Mean particle sizes in dependence of time for different precipitation pH are plotted in Figure 6.8. To compare the growth obtained from XRPD with *in situ* SAXS measurements, a power law of 2.6 consistent with the growth exponent of n=2.6 obtained from the kinetic analysis of the SAXS, is plotted as a reference in each plot. Precipitation of magnetite in the presence of PDADMAC at ph 9 and 10, of chitosan at pH 10 and of JR-400 at pH 9 can be considered to comply with the growth exponent. However, chitosan prepared at pH 9 and 11 shows an unexpected decrease in particle size with time. An irrevocable proportionality of the growth rate with pH, as it has been established for polyarginine, however, could not be confirmed. Eager to apply the ability to grow large mesocrytals to PDADMAC, JR-400 and chitosan, we followed the

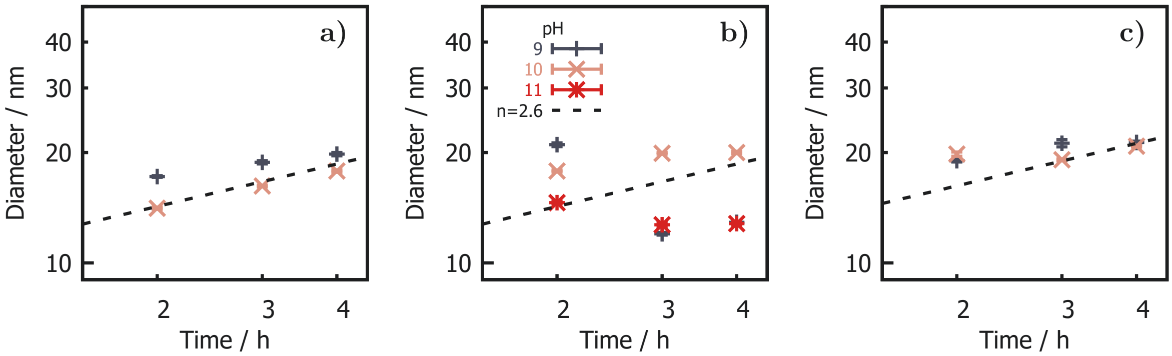

Figure 6.8: XRPD measurements to obtain particle growth for different pH as indicated in the plots for a) PDADMAC, b) chitosan and c) JR-400. The solid line indicates the growth exponent obtained from the kinetic analysis of the *in situ* SAXS data, fitting acceptably well to most of the datasets. This suggests that the mechanistic distortion of magnetite nucleation can be universally attributed to the presence of a polycation.

protocol established in paragraph Section 5.8. In short, we co-precipitated ferrous and ferric chloride at molar ratio of 1:2 and a total concentration of 0.5 M at pH of 11 in the presence of 0.1 $\text{mg}\,\text{mL}^{-1}$ of the respective polycation for 24 h. For the investigation in TEM we magnetically precipitated the aliquots for 1 min and cleaned all samples twice using Milli-Q water. HRTEM images with single crystal electron diffractograms in the bottom right inset are shown in Figure 6.9. As for polyarginine we were able to produce substructured, individual magnetite nanoparticles with sizes of up to 150 nm with by the addition of chitosan or JR-400. In the presence of PDADMAC, however, we yield large, single crystals, that do not exhibit substructuring, but seem to form octahedrally shaped magnetite nanoparticles with a size of around 80 nm. Overview TEM images, Figure 3, are added in the Appendix.

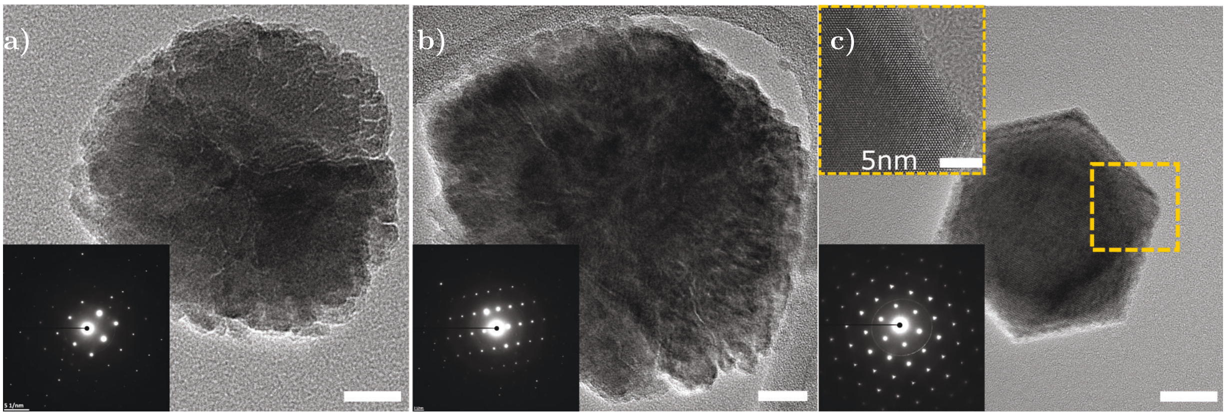

Figure 6.9: TEM images of particles prepared in the presence of 0.1 $\text{mg}\,\text{mL}^{-1}$ a) chitosan, b) JR-400 and c) PDADMAC for 24 h using the adapted synthesis protocol. Electron diffractograms of single particles are shown in the bottom left inset and indicate single crystallinity for b) and c). While in the presence of chitosan and JR-400 substructured particles are formed, we obtain octahedral shaped particles in the presence of PDADMAC. Scale bar 20 nm.

6.3.5 Magnetic Properties

For particles prepared at pH 11 in the presence of 0.1 $\mathrm{mg\,mL^{-1}}$ PDADMAC, JR-400 or chitosan, we measured the magnetization as a response to an externally applied magnetic field on bulk samples after 2 h of synthesis, complementary to previous measurements for polyarginine shown in paragraph Section 4.2.2. As for poly-L-arginine, the aliquot size was too small to normalize the maximum magnetization by the sample mass. For better comparability of the measured curves, the magnetization as a function of the applied magnetic field is normalized by the magnetization of particles at the maximum field applied. Particles prepared with JR-400 exhibit a very weak magnetization and no saturation at the maximum field of 1 T indicative of either the existence of hematite or the presence of particles with a sub 3 nm size that do not magnetically saturate. The chitosan and PDADMAC sample are both saturated at high fields. The chitosan sample shows a wasp-waisted loop suggesting the presence of a broader particle size distribution around 22 nm of SP and SSD particles leading to an opening of the hysteresis loop at higher fields induced by the larger particles.[94] Magnetite prepared in the presence of PDADMAC at pH 11 shows an open hysteresis loop indicating that the particles have grown beyond the SSD particle size threshold.

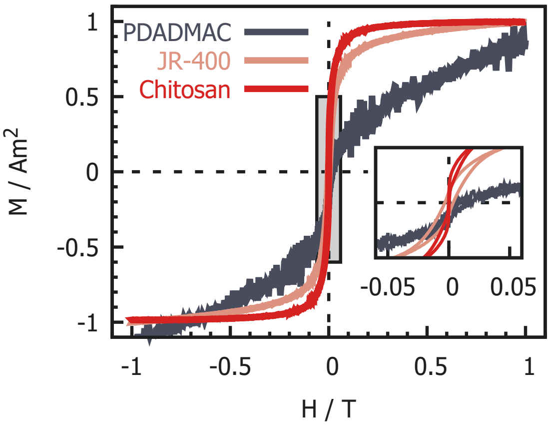

Figure 6.10: Magnetic measurement of immobilized magnetite nanoparticles prepared in the presence of 0.1 $\mathrm{mg\,mL^{-1}}$ PDADMAC, JR-400 or chitosan. From the opening of the hysteresis loop for particles prepared in the presence of PDADMAC and chitosan the presence of SSD particles is suggested. Chitosan, however, exhibits a wasp-waisted hysteresis loop, indicative of a particle size distribution around 22 nm.

6.3.6 Discussion

This chapter aimed to elucidate the possibility to substitute poly-L-arginine with other strong polycations and investigate their influence on the co-precipitation of ferrous and ferric chloride under alkaline conditions. We have shown in the previous chapters, that the addition of poly-L-arginine has a pivotal impact on the formation of magnetite, manifesting itself in the reversal of the dependence of the growth rate on pH (Section 5.4.1) and the induction of a transition from a spherical to a substructured morphology (Section 4.2.1). However, we want to foreclose that deviations from the behavior of polyarginine can have a multitude of reasons. We want to especially stress here, that quaternized chitosan and JR-400 are polymers that have not been synthesized under ideal laboratory conditions but extracted from natural sources (chitosan) or synthesized industrially (JR-400) on a metric ton scale.

We can confirm a morphological transition from spherical to substructured magnetite nanoparticles when JR-400 or chitosan is added to the synthesis. Surprisingly, PDADMAC does not induce such a transition, even though particle sizes are comparable with sizes obtained for all other polycations. Also for particles grown for 24 h at pH 11, we do not observe a substructured morphology for PDADMAC, again in contrast to samples prepared in the presence of chitosan or JR-400. Lacking characterization of the polycations we can here only speculate about this discrepancy. We have argued in chapter INSERT that a considerable entropic contribution to the free energy of particle formation may govern the formation of magnetite nanoparticles formation. Thus, on the one hand, the release of hydration water upon crystallization will drive this synthesis, but on the other hand, the release of the polymer will add to the net entropy of the system. We thus suggest, that the polycation charge density, as well as the persistence length, will have an impact on the energy landscape of the synthesis. In the case of PDADMAC we expect a higher charge density, and thus the release of the polymer may be retarded. This retardation may give the precursor particles more time to cover the surface of the nanoparticles so that we observe no substructuring. For all polycations tested, the size distribution from triplicates, and thus the reproducibility seems to have decreased compared to magnetite formed in the presence of polyarginine. Size distribution measured using TEM from triplicates, shown in the Appendix Figure 2, demonstrate –in contrast to the results from XRPD– that the synthesis of magnetite in the presence of PDADMAC is highly reproducible. This result suggests that this may also be the case for the other polycations. Due to a miss-function of the μ-spot beamline a replication of the XRPD measurements to reexamine reproducibility of the synthesis, was not possible.

The inversion of the dependence of the growth rate on pH is, a strong indication for the interference of poly-L-arginine in the mechanism of magnetite nucleation. We could show that this trend is also prevalent for JR-400 as well as for chitosan. The non-monotonic behavior of the final size with pH for PDADMAC, however, was surprising. Further, no substructured mesocrystals were formed at pH 11 when PDADMAC was present. Based on the current knowledge of the formation of magnetite in the presence of polycations, we are not able to fully explain this behavior. In order to induce this non-monotonic behavior, we predict an interaction of the polymer with the existing iron phases, that does not change monotonically with pH.

6.4 Conclusion

Using the strong polycations PDADMAC, quaternized chitosan and JR-400 as a substitute for poly-L-arginine we were able to reproduce a majority of the effects that poly-L-arginine has on co-precipitation of magnetite, including i) the effect of pH on the morphological transition between spherical, solid particles, to substructured mesocrystals, ii) the inversion of the growth rate and thus the final size of magnetite with respect to the precipitation pH, iii) the ability to grow large single crystals at extended precipitation time and iv) the growth exponent of 2.6 obtained from time dependent XRPD measurements. In showing how to substitute poly-L-arginine, we have not only established a strong mechanistic correlation for strong polycations and polycations with a high isoelectric point, but have simultaneously developed a protocol how to produce advanced, functional magnetic materials[138] using cheaper, renewable and more sustainable polymers that, even when produced at a metric ton scale, can still be employed in our system. Due to the decrease in cost of the precursors and the high availability of the used polymers, we envision that up-scaling may now be more economical and could thus be the focus of future research.

While the slight deviation from the reported mechanism (section 5) for PDADMAC may give new insights into the formation mechanism, we find that the strong correlation of properties obtained for JR-400, chitosan and PDADMAC compared to polyarginine, strongly suggests that the interference of poly-L-arginine with the nucleation mechanism of magnetite is non-specific to polyarginine but rather a generic phenomenon distinct to strong polycations.

Chapter 7

General Conclusion and Outlook

While the influence of polyanions on the nucleation of magnetite in biological and synthetic systems has been thoroughly studied, the influence of polycations has not. We demonstrate in this thesis, however, how the presence of polycations in the co-precipitation of ferrous and ferric chloride can pivotally influence the energy landscape of crystal nucleation. Exploring the effects of poly-L-arginine, of cationic polysaccharides, and of PDADMAC, we were able to produce highly advanced magnetite nanoparticles in a sustainable process at ambient pressure and temperatures in an aqueous environment using renewable polymer sources. Exploring the effect of pH, we were able to change the morphology of the synthesized magnetite from solid spherical nanoparticles at a pH below 11 to sub-structured mesocrystals at a pH of above 11. Depending on growth times, we were able to obtain solid nanoparticles with diameters of between 10 and 50 nm, while the sub-structured mesocrystal size could be tuned to between 40 and 180 nm. All particles show narrow size distributions and are colloidally stable for an extended time period. While exploring the synthetic capabilities, we realized that the addition of polycations alters the nucleation mechanism of magnetite, exceeding the previously proposed capabilities of electrostatically aggregating small magnetite crystallites. A distinguishing feature of this alteration is the inversion of the pH-dependent growth rate of the nanoparticles and the morphological transition between spherical crystals and mesocrystals, both of which appear to conflict with classical notions of nucleation theory. Striving to elucidate this novel mechanism, we employed high-brilliance synchrotron SAXS to temporally resolve the nucleation of magnetite in the presence of poly-L-arginine *in situ*. We identified that the crucial step in the modification of magnetite nucleation was achieving electrostatic stabilization of 5 nm, low-density iron precursor particles through poly-L-arginine. Because of the existence of the precursor particles and the relatively low activation energy measured, we concluded that polycations shift the nucleation of magnetite from a thermodynamically controlled scenario to a kinetically controlled one. Considering the shift to kinetic control enabled us to explain the inversion of the pH-dependent growth rate, which is now governed by the alkaline catalyzed oxolation reaction. Based on theoretic considerations, our explanation for the pH-dependent morphological transition is contingent on the surface charge-dependent wetting behavior of the precursor particles at the nanoparticle surface. At low pH levels, we find small contact angles and thus strong wetting, leading to spherical crystals; while at high pH levels, wetting is energetically less favored, leading to larger contact angles and thus the formation of sub-structured nanoparticles. While poly-L-arginine /magnetite particles were developed using a biomimetic approach emulating magnetotactic bacteria's proteome, the stabilization of low-density, non-crystalline precursor particles by charged macro-molecules exhibits an obvious analogy to biomineralization. Numerous reports have suggested that the extraordinary single-crystal morphologies prevalent in nature are achieved precisely because organisms use metastable precursor phases that crystallize in a homoepitaxial manner. In conclusion, we have thus not only developed a system that is able to yield highly advanced magnetic nanoparticles, but by elucidating the formation mechanism, have also found a way to use kinetically controlled nanoparticle nucleation to form extraordinary crystal shapes in a process analogous to biomineralization. Our *in vitro* studies, in turn, may even help us to further research biomineralization processes in parameterized *ex vivo* studies.

In future experiments, we will strive to confirm and extend the formation mechanism presented in this work. Using XRPD to study the formation rate of magnetite in the presence and absence of poly-L-arginine at different temperatures, we will obtain activation energies for our predicted kinetically or thermodynamically controlled nucleation processes. We foresee a significant lowering of the activation energies for the nucleation of magnetite performed in the presence of poly-L-arginine or any other strong polycation. Further, we have presumed that the low-density iron precursor structure is a ferric (oxyhydr)oxide, which would render it metastable when compared to magnetite. Using cryo-XANES (X-ray absorption near edge structure) in combination with EXAFS (extended X-ray absorption fine structure), we will not only obtain information on the chemical environment of iron, from which its phase can be inferred, but also atomic radial distribution functions, from which coordination shells can be calculated. Fitting, for example, Fe-Fe distances, we will be able to obtain the ratio of corner- and edge-connected iron octahedrons, from which the dynamics within a precursor particle may be inferred. This dynamics, in turn, will have important ramifications for the proposed wetting process, which we have identified as inducing the transition from spherical to sub-structured magnetite nanoparticles. Preliminary measurements performed by Daniel Chevrier at the Advanced Photon Source show a shift of the white line to higher energies for particles present in the early stages of the synthesis compared to a reference magnetite sample. This shift is indicative of a higher oxidation state of the precursor particles and thus suggests the existence of ferric (oxy)hydroxide, affirming our assumption that polyR stabilizes metastable iron phases. The cryo-XANES data of the synthesis product that vitrified after 5 and 15 minutes following iron addition are attached in the Appendix as Figure 4.

We have demonstrated that the modification of the mechanism of magnetite nucleation can be generalized to electrostatic interaction of any strong polycation with metastable iron precursor phases. It seems intuitive to wonder whether this phenomenon is an even more generic one that can be applied to any oxide-forming nanoparticles. Knowing about this application would be of particular interest, as among these

oxides we find economically highly relevant semiconductors such as TiO2, ZrO, or ZnO. For these semiconductors, size and morphology play a pivotal role in determining the width of the gap between valence and conduction band. Thus, a fine tuning of electronic properties is possible, essential for exploiting their light-harvesting abilities or their catalytic activity.

We are intrigued by the beauty of the huge mesocrystals, that remain, despite their large dimensions, as single crystals. We think that this single crystallinity, in combination with the physically present gaps, may have a significant effect on the energy attributed to the formation of domain walls. While bulk measurements average the magnetic properties from the whole sample, it would be beneficial to obtain magnetic information (hysteresis curves, induction maps) from single particles. Advanced analytical tools offer the ability to combine magnetic measurements with spatial resolution. Among these tools are off-axis electron holography and X-ray magnetic circular dichroism (XMCD) in combination with a photoemission electron microscope (PEEM) or electron magnetic circular dichroism (EMCD).

We further postulate that the growth of magnetite in the presence of polyR can be sustained indefinitely until a critical counter-ion (with chloride showing the strongest retardation effect) concentration is reached. We should thus be able to obtain discrete magnetite nanoparticles as single crystals as well as in their mesocrystalline phase at any desired size if the reaction volume is increased. As co-precipitation so far fails to produce magnetite in reactors of modified geometry, more investigation must be done on the involved fluid dynamics, which may conclusively determine the success of the synthesis.

Bibliography

[1] H. Sun, L. Cao and L. Lu, *Nano Research*, 2011, **4**, 550–562.

[2] L. C. P. M. D. Smet, *Journal of Materials Chemistry A*, 2017, **5**, year.

[3] H. Zeng, J. Li, J. P. Liu, Z. L. Wang and S. Sun, *Nature*, 2002, **420**, 395–398.

[4] C. Ó Dálaigh, S. A. Corr, Y. Gun'ko and S. J. Connon, *Angewandte Chemie - International Edition*, 2007, **46**, 4329–4332.

[5] A. Hu, G. T. Yee and W. Lin, *Journal of the American Chemical Society*, 2005, **127**, 12486–12487.

[6] M. Kotani, T. Koike, K. Yamaguchi and N. Mizuno, *Green Chemistry*, 2006, **8**, 735–741.

[7] E. M. Anderson and J. B. Collip, *The Lancet*, 1934, **223**, 784–786.

[8] Y. Sahoo, A. Goodarzi, M. T. Swihart, T. Y. Ohulchanskyy, N. Kaur, E. P. Furlani and P. N. Prasad, *Journal of Physical Chemistry B*, 2005, **109**, 3879–3885.

[9] M. Lewin, N. Carlesso, C. H. Tung, X. W. Tang, D. Cory, D. T. Scadden and R. Weissleder, *Nature Biotechnology*, 2000, **18**, 410–414.

[10] S. Laurent, S. Dutz, U. O. Häfeli and M. Mahmoudi, *Advances in Colloid and Interface Science*, 2011, **166**, 8–23.

[11] E. Alphandéry, S. Faure, O. Seksek, F. Guyot and I. Chebbi, *ACS Nano*, 2011, **5**, 6279–6296.

[12] J. W. Bulte, T. Douglas, B. Witwer, S. C. Zhang, E. Strable, B. K. Lewis, H. Zywicke, B. Miller, P. Van Gelderen, B. M. Moskowitz, I. D. Duncan and J. A. Frank, *Nature Biotechnology*, 2001, **19**, 1141–1147.

[13] P. K. Gupta and H. Cheung-Tak, *International Journal of Pharmaceutics*, 1990, **59**, 57–67.

[14] S. Guo, D. Li, L. Zhang, J. Li and E. Wang, *Biomaterials*, 2009, **30**, 1881–1889.

[15] V. G. Roullin, J. R. Deverre, L. Lemaire, F. Hindré, M. C. Venier-Julienne, R. Vienet and J. P. Benoit, *European Journal of Pharmaceutics and Biopharmaceutics*, 2002, **53**, 293–299.

[16] U. Schwertmann and R. Cornell, *The Iron Oxides*, Wiley-VCH, 2004.

[17] G. Sherwood, *Mineralogical Magazine*, 2002, **66**, 232–232.

[18] Z. Wang, A. H. Tavabi, L. Jin, J. Rusz, D. Tyutyunnikov, H. Jiang, Y. Moritomo, J. Mayer, R. E. Dunin-borkowski, R. Yu and J. Zhu, *Nature Materials*, 2018, **17**, 221–226.

[19] A. R. Muxworthy and W. Williams, *Journal of Geophysical Research: Solid Earth*, 2006, **111**, 3–9.

[20] T. J. Daou, G. Pourroy, S. Bégin-Colin, J. M. Grenèche, C. Ulhaq-Bouillet, P. Legaré, P. Bernhardt, C. Leuvrey and G. Rogez, *Chemistry of Materials*, 2006, **18**, 4399–4404.

[21] Y. Lee, J. Lee, C. J. Bae, J. G. Park, H. J. Noh, J. H. Park and T. Hyeon, *Advanced Functional Materials*, 2005, **15**, 503–509.

[22] L. Shen, Y. Qiao, Y. Guo, S. Meng, G. Yang, M. Wu and J. Zhao, *Ceramics International*, 2014, **40**, 1519–1524.

[23] Y.-H. Zheng, Y. Cheng, F. Bao and Y.-S. Wang, *Materials Research Bulletin*, 2006, **41**, 525–529.

[24] X. Sun, C. Zheng, F. Zhang, Y. Yang, G. Wu, A. Yu and N. Guan, *Journal of Physical Chemistry C*, 2009, **113**, 16002–16008.

[25] Y. Liu, Y. Chen, Y. Zeng and S. Wang, *Science in China, Series B: Chemistry*, 2009, **52**, 916–923.

[26] J. Wang, J. Sun, Q. Sun and Q. Chen, *Materials Research Bulletin*, 2003, **38**, 1113–1118.

[27] P. A. Dresco, V. S. Zaitsev, R. J. Gambino and B. Chu, *Langmuir*, 1999, **15**, 1945–1951.

[28] H. S. Lee, W. C. Lee and T. Furubayashi, *Journal of Applied Physics*, 1999, **85**, 5231–5233.

[29] R. V. Kumar, Y. Koltypin, Y. S. Cohen, Y. Cohen, D. Aurbach, O. Palchik, I. Felner and A. Gedanken, *Journal of Materials Chemistry*, 2000, **10**, 1125–1129.

[30] G. Marchegiani, P. Imperatori, A. Mari, L. Pilloni, A. Chiolerio, P. Allia, P. Tiberto and L. Suber, *Ultrasonics Sonochemistry*, 2012, **19**, 877–882.

[31] Y. Mizukoshi, T. Shuto, N. Masahashi and S. Tanabe, *Ultrasonics Sonochemistry*, 2009, **16**, 525–531.

[32] S. Wang, H. Xin and Y. Qian, *Materials Letters*, 1997, **33**, 113–116.

[33] Y. B. Khollam, S. R. Dhage, H. S. Potdar, S. B. Deshpande, P. P. Bakare, S. D. Kulkarni and S. K. Date, *Materials Letters*, 2002, **56**, 571–577.

[34] W. W. Wang, Y. J. Zhu and M. L. Ruan, *Journal of Nanoparticle Research*, 2007, **9**, 419–426.

[35] S. Sun and H. Zeng, *Journal of the American Chemical Society*, 2002, **124**, 8204–8205.

[36] K. Woo, J. Hong and J. P. Ahn, *Journal of Magnetism and Magnetic Materials*, 2005, **293**, 177–181.

[37] N. Pinna, S. Grancharov, P. Beato, P. Bonville, M. Antonietti and M. Niederberger, *Chemistry of Materials*, 2005, **17**, 3044–3049.

[38] C. De Mello Donegá, P. Liljeroth and D. Vanmaekelbergh, *Small*, 2005, **1**, 1152–1162.

[39] W. Zhou, J. Wu and H. Yang, *Nano Letters*, 2013, **13**, 2870–2874.

[40] M. D. Sikirić and H. Füredi-Milhofer, *Advances in Colloid and Interface Science*, 2006, **128-130**, 135–158.

[41] F. Dumestre, B. Chaudret, C. Amiens, M. Respaud, P. Fejes, P. Renaud and P. Zurcher, *Angewandte Chemie - International Edition*, 2003, **42**, 5213–5216.

[42] A. H. Lu, E. L. Salabas and F. Schüth, *Angewandte Chemie - International Edition*, 2007, **46**, 1222–1244.

[43] L. Qiao, Z. Fu, J. Li, J. Ghosen, M. Zeng, J. Stebbins, P. N. Prasad and M. T. Swihart, *ACS Nano*, 2017, 6370—-6381.

[44] C. L. Altan, B. Gurten, R. Sadza, E. Yenigul, N. A. Sommerdijk and S. Bucak, *Journal of Magnetism and Magnetic Materials*, 2016, **416**, 366–372.

[45] S. Si, A. Kotal, T. K. Mandal, S. Giri, H. Nakamura and T. Kohara, *Chemistry of Materials*, 2004, **16**, 3489–3496.

[46] G. Mirabello, A. Keizer, P. H. H. Bomans, A. Kovács, R. E. Dunin-Borkowski, N. A. J. M. Sommerdijk and H. Friedrich, *Chemistry of Materials*, 2019, acs.chemmater.9b01836.

[47] C. L. Altan, J. J. Lenders, P. H. Bomans, G. De With, H. Friedrich, S. Bucak and N. A. Sommerdijk, *Chemistry - A European Journal*, 2015, **21**, 6150–6156.

[48] S. Sviben, A. Gal, M. A. Hood, L. Bertinetti, Y. Politi, M. Bennet, P. Krishnamoorthy, A. Schertel, R. Wirth, A. Sorrentino, E. Pereiro and D. Faivre, *Nature communications*, 2016, **7**, 1–9.

[49] M. A. Hood, H. Leemreize, A. Scheffel and D. Faivre, *Journal of Structural Biology*, 2016, **196**, 147–154.

[50] B. Y. S. Mann, N. H. C. Sparks, M. M. Walker and J. L. Kirschvink, *J.exp.Biol*, 1988, **49**, 35–49.

[51] H. Cölfen and S. Mann, *Angewandte Chemie - International Edition*, 2003, **42**, 2350–2365.

[52] M. Albéric, L. Bertinetti, Z. Zou, P. Fratzl, W. Habraken and Y. Politi, *Advanced Science*, 2018, **5**, year.

[53] E. Reich, V. Schoeppler, R. Lemanis, E. Lakin, E. Zolotoyabko, D. Zöllner and I. Zlotnikov, *Acta Biomaterialia*, 2019, **85**, 272–281.

[54] C. Y. Hsu and C. W. Li, *Science*, 1994, **265**, 95–97.

[55] J. L. Kirschvink, M. M. Walker and C. E. Diebel, *Current Opinion in Neurobiology*, 2001, 462–468.

[56] R. C. Beason and J. E. Nichols, *Nature*, 1984, **309**, 151–153.

[57] J. L. Kirschvink, A. Kobayashi-Kirschvink and B. J. Woodford, *Proceedings of the National Academy of Sciences of the United States of America*, 1992, **89**, 7683–7687.

[58] D. S. McKay, E. K. Gibson, K. L. Thomas-Keprta, H. Vali, C. S. Romanek, S. J. Clemett, X. D. Chillier, C. R. Maechling and R. N. Zare, *Science*, 1996, **273**, 924–930.

[59] J. Baumgartner, A. Dey, P. H. H. Bomans, C. Le Coadou, P. Fratzl, N. A. J. M. Sommerdijk and D. Faivre, *Nature materials*, 2013, **12**, 310–314.

[60] F. M. Michel, V. Barron, J. Torrent, M. P. Morales, C. J. Serna, J.-F. Boily, Q. Liu, A. Ambrosini, A. C. Cismasu and G. E. Brown, *Proceedings of the National Academy of Sciences*, 2010, **107**, 2787–2792.

[61] L. M. Gordon, J. K. Román, R. M. Everly, M. J. Cohen, J. J. Wilker and D. Joester, *Angewandte Chemie - International Edition*, 2014, **53**, 11506–11509.

[62] S. Mann, *Nature*, 1988, **332**, 119–124.

[63] A. Hajdú, E. Illés, E. Tombácz and I. Borbáth, *Colloids and Surfaces A: Physicochemical and Engineering Aspects*, 2009, **347**, 104–108.

[64] A. E. Rawlings, L. A. Somner, M. Fitzpatrick-milton, T. P. Roebuck, C. Gwyn, P. Liravi, V. Seville, T. J. Neal, O. O. Mykhaylyk, S. A. Baldwin and S. S. Staniland, *Nature Communications*, 2019, **10**, 1–9.

[65] V. Reichel, A. Kovács, M. Kumari, É. Bereczk-tompa, E. Schneck, P. Diehle, M. Pósfai, A. M. Hirt, M. Duchamp and R. E. Dunin-borkowski, *Scientific Reports*, 2017, 1–8.

[66] E. V. Sturm and H. Cölfen, *Chemical Society Reviews*, 2016, **45**, 5821–5833.

[67] L. Vayssières, C. Chanéac, E. Tronc and J. P. Jolivet, *Journal of colloid and interface science*, 1998, **205**, 205–212.

[68] S. Mann, N. H. Sparks, S. B. Couling, M. C. Larcombe and R. B. Frankel, *Journal of the Chemical Society, Faraday Transactions 1: Physical Chemistry in Condensed Phases*, 1989, **85**, 3033–3044.

[69] D. Faivre, P. Agrinier, N. Menguy, P. Zuddas, K. Pachana, A. Gloter, J. Y. Laval and F. Guyot, *Geochimica et Cosmochimica Acta*, 2004, **68**, 4395–4403.

[70] J. P. Jolivet, P. Belleville, E. Tronc and J. Livage, 1992, **40**, 531–539.

[71] E. Tronc, P. Belleville, J. P. Jolivet and J. Livage, *Langmuir*, 1992, **8**, 313–319.

[72] J. Baumgartner, A. Dey, P. H. H. Bomans, C. Le Coadou, P. Fratzl, N. A. J. M. Sommerdijk and D. Faivre, *Nature Materials*, 2013, **12**, 310–314.

[73] J. I. Langford and A. J. C. Wilson, *Journal of Applied Crystallography*, 1978, **11**, 102–113.

[74] P. Scherrer, *Nachr. Ges. Wiss. Göttingen*, 1918, 98–100.

[75] I. Zizak, *Journal of large-scale research facilities JLSRF*, 2016, **2**, A101.

[76] A. Fischer, M. Schmitz, B. Aichmayer, P. Fratzl and D. Faivre, *Journal of the Royal Society, Interface / the Royal Society*, 2011, **8**, 1011–1018.

[77] G. Benecke, W. Wagermaier, C. Li, M. Schwartzkopf, G. Flucke, R. Hoerth, I. Zizak, M. Burghammer, E. Metwalli, P. Müller-Buschbaum, M. Trebbin, S. Förster, O. Paris, S. V. Roth and P. Fratzl, *Journal of Applied Crystallography*, 2014, **47**, 1797–1803.

[78] D. S. Sivia, *Elementary Scattering Theory*, Oxford University Press, Oxford, 2011.

[79] T. Narayanan, M. Sztucki, P. Van Vaerenbergh, J. Léonardon, J. Gorini, L. Claustre, F. Sever, J. Morse and P. Boesecke, *Journal of Applied Crystallography*, 2018, **51**, 1511–1524.

[80] C. Hetherington, *Materials Today*, 2004, **7**, 50–55.

[81] J.-P. Jolivet, L. Vayssières, C. Chaneac and E. Tronc, *Mat. Res. Soc. Symp. Proc.*, 1997, **432**, 145–150.

[82] J. Baumgartner, L. Bertinetti, M. Widdrat, A. M. Hirt and D. Faivre, *PLoS ONE*, 2013, **8**, 1–6.

[83] J. Baumgartner, M. Antonietta Carillo, K. M. Eckes, P. Werner and D. Faivre, *Langmuir*, 2014, **30**, 2129–2136.

[84] E. F. Kneller and F. E. Luborsky, *Journal of Applied Physics*, 1963, **34**, 656–658.

[85] B. V. Derjaguin, *Acta Phys. Chim*, 1939, **10**, 333–346.

[86] B. V. Derjaguin and L. Landau, *Acta Physicochim. URSS*, 1941, **14**, 633.

[87] E. J. W. Verwey and J. T. G. Overbeek, *Theory of the Stability of Lyophobic Colloids*, Elsevier, Amsterdam, 1948.

[88] S. E. Ziemniak, M. E. Jones and K. E. Combs, *Journal of Solution Chemistry*, 1995, **24**, 837–877.

[89] L. Vayssieres, *International Journal of Nanotechnology*, 2005, **2**, 411.

[90] J.-P. Jolivet, C. Froidefond, A. Pottier, C. Chaneac, S. Cassaignon, E. Tronc and P. Euzen, *Journal of Materials Chemistry*, 2004, **14**, 3281.

[91] F. Jones, H. Cölfen and M. Antonietti, *Colloid and Polymer Science*, 2000, **278**, 491–501.

[92] Z. Zou, L. Bertinetti, Y. Politi, P. Fratzl and W. J. Habraken, *Small*, 2017, **13**, 1–11.

[93] D. Zahn, *ChemPhysChem*, 2015, **16**, 2069–2075.

[94] M. Kumari, M. Widdrat, É. Tompa, R. Uebe, D. Schüler, M. Pósfai, D. Faivre and A. M. Hirt, *Journal of Applied Physics*, 2014, **116**, year.

[95] J. Ge, Y. Hu, M. Biasini, W. P. Beyermann and Y. Yin, *Angewandte Chemie - International Edition*, 2007, **46**, 4342–4345.

[96] G. Gnanaprakash, S. Mahadevan, T. Jayakumar, P. Kalyanasundaram, J. Philip and B. Raj, *Materials Chemistry and Physics*, 2007, **103**, 168–175.

[97] K. Nishio, M. Ikeda, N. Gokon, S. Tsubouchi, H. Narimatsu, Y. Mochizuki, S. Sakamoto, A. Sandhu, M. Abe and H. Handa, *Journal of Magnetism and Magnetic Materials*, 2007, **310**, 2408–2410.

[98] A. Arakaki, F. Masuda, Y. Amemiya, T. Tanaka and T. Matsunaga, *Journal of Colloid and Interface Science*, 2010, **343**, 65–70.

[99] S. Sun, D. Gebauer and H. Cçlfen, *Angewandte Chemie - Communications*, 2017, 4042–4046.

[100] M. Takesue, T. Tomura, M. Yamada, K. Hata, S. Kuwamoto and T. Yonezawa, *Journal of the American Chemical Society*, 2011, **133**, 14164–14167.

[101] D. Pontoni, J. Bolze, N. Dingenouts, T. Narayanan, M. Ballauff and V. Uni, *Journal of Physical chemistry*, 2003, 5123–5125.

[102] I. Grillo, *Current Opinion in Colloid and Interface Science*, 2009, **14**, 402–408.

[103] M. Bremholm, M. Felicissimo and B. B. Iversen, *Angewandte Chemie - International Edition*, 2009, **48**, 4788–4791.

[104] B. Abécassis, C. Bouet, C. Garnero, D. Constantin, N. Lequeux, S. Ithurria, B. Dubertret, B. R. Pauw and D. Pontoni, *Nano Letters*, 2015, **15**, 2620–2626.

[105] A. Lassenberger, T. A. Grünewald, P. D. J. Van Oostrum, H. Rennhofer, H. Amenitsch, R. Zirbs, H. C. Lichtenegger and E. Reimhult, *Chemistry of Materials*, 2017, **29**, 4511–4522.

[106] A. P. Lagrow, M. O. Besenhard, A. Hodzic, A. Sergides, L. K. Bogart, A. Gavriilidis and N. T. K. Thanh, *Nanoscale*, 2019, **11**, 6620–6628.

[107] A. J. Hurd, *America Journal of Physics*, 2015, **969**, year.

[108] A. T. Cawley and U. Flenker, *Journal of mass spectrometry : JMS*, 2008, **43**, 854–864.

[109] J.-Y. Bottero, A. Manceau, F. Villieras and D. Tchoubars, *Langmuir*, 1994, **10**, 316–319.

[110] B. Hammouda, *Macromolecular Theory and Simulations*, 2012, **21**, 372–381.

[111] A. J. Hurd and W. L. Flower, *Journal of Colloid And Interface Science*, 1988, **122**, 178–192.

[112] M. Muthig, S. Prevost, R. Orglmeister and M. Gradzielski, *Journal of Applied Crystallography*, 2013, **46**, 1187–1195.

[113] M. Widdrat, E. Schneck, V. Reichel, J. Baumgartner, L. Bertinetti, W. Habraken, K. Bente, P. Fratzl and D. Faivre, *The Journal of Physical Chemistry Letters*, 2017, 1132–1136.

[114] A. W. Xu, W. F. Dong, M. Antonietti and H. Cölfen, *Advanced Functional Materials*, 2008, **18**, 1307–1313.

[115] N. T. K. Thanh, N. Maclean and S. Mahiddine, *Chemical Reviews*, 2014, **114**, 7610–7630.

[116] P. Fratzl, J. Lebowitz, O. Penrose and J. Amar, *Physical Review B*, 1991, **44**, year.

[117] D. W. Schaefer, **4**, year.

[118] A. L. Rose, M. W. Bligh, R. N. Collins and T. D. Waite, *Langmuir*, 2014, **30**, 3548–3556.

[119] A. L. Rose and T. David Waite, *Geochimica et Cosmochimica Acta*, 2007, **71**, 5605–5619.

[120] J. Scheck, M. Drechsler, X. Ma, M. T. Stöckl, J. Konsek, J. B. Schwaderer, S. M. Stadler, J. J. De Yoreo and D. Gebauer, *Journal of Chemical Physics*, 2016, **145**, year.

[121] B. Gilbert, G. Lu and C. S. Kim, *Journal of Colloid and Interface Science*, 2007, **313**, 152–159.

[122] D. Tchoubars, J.-Y. Bottero, P. Qienne and M. Arnaud, *Langmuir*, 1991, 398–402.

[123] Y. Sun, X. Zuo, S. K. R. S. Sankaranarayanan, S. Peng, B. Narayanan and G. Kamath, 2017, **307**, 303–307.

[124] A. Navrotsky, L. Mazeina and J. Majzlan, *Science*, 2008, **319**, 1635–1638.

[125] C. Tanford, *The hydrophobic effect: formation of micelles and biological mambranes*, Wiley, 1980, p. 233.

[126] W. J. Habraken, J. Tao, L. J. Brylka, H. Friedrich, L. Bertinetti, A. S. Schenk, A. Verch, V. Dmitrovic, P. H. Bomans, P. M. Frederik, J. Laven, P. Van Der Schoot, B. Aichmayer, G. De With, J. J. DeYoreo and N. A. Sommerdijk, *Nature Communications*, 2013, **4**, 1507–1512.

[127] L. Vayssieres, *The Journal of Physical Chemistry Letters C*, 2009, **12**, 4733–4736.

[128] A. Navrotsky, C. Ma, K. Lilova and N. Birkner, *Science (New York, N.Y.)*, 2010, **330**, 199–201.

[129] Y. Zhang and P. S. Cremer, *Current Opinion in Chemical Biology*, 2006, **10**, 658–663.

[130] R. V. Klitzing, J. E. Wong, W. Jaeger and R. Steitz, *Current Opinion in Colloid and Interface Science*, 2004, **9**, 158–162.

[131] Z. Ou and M. Muthukumar, *Journal of Chemical Physics*, 2006, **124**, year.

[132] V. Malinova and C. Wandrey, *Polymer News*, 2005, **30**, 378–380.

[133] R. R. Netz and J. F. Joanny, *Macromolecules*, 1999, **32**, 9013–9025.

[134] P. Jorge, I. Pastoriza-santos, L. M. Liz-marz and P. Mulvaney, *Coordination Chemistry Reviews*, 2005, **249**, 1870–1901.

[135] L. Vigderman, B. P. Khanal and E. R. Zubarev, *Advance Materials*, 2012, 4811–4841.

[136] R. Sardar, A. M. Funston, P. Mulvaney and R. W. Murray, *Langmuir*, 2009, **25**, 13840–13851.

[137] A. P. Alivisatos, *Alivisatos1996.pdf*, 1996.

[138] N. V. Tarakina, A. M. Hirt, L. Kuhrts, E. Mac and D. Faivre, *Journal of Physical Chemistry Letters*, 2019, **10**, 5514–5518.

[139] C. A. Fitch, G. Platzer, M. Okon, B. E. Garcia-Moreno and L. P. McIntosh, *Protein Science*, 2015, **24**, 752–761.

[140] F. Caruso, H. Lichtenfeld, M. Giersig and H. Mohwald, *Journal of the American Chemical Society*, 1998, **120**, 8523–8524.

[141] F. Caruso, R. A. Caruso and H. Möhwald, *Science*, 1998, **282**, 1111–1114.

Appendices

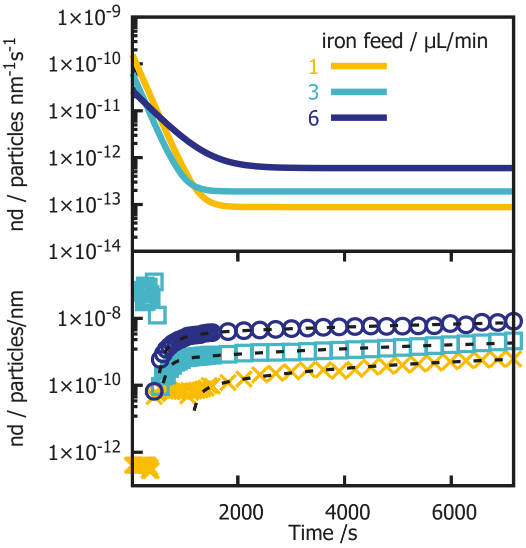

Figure 1: Calculated number density for particles prepared at different feeding rates of iron solution. From the fits (dashed lines) we calculated nucleation rate as the time derivative of the particles concentration.

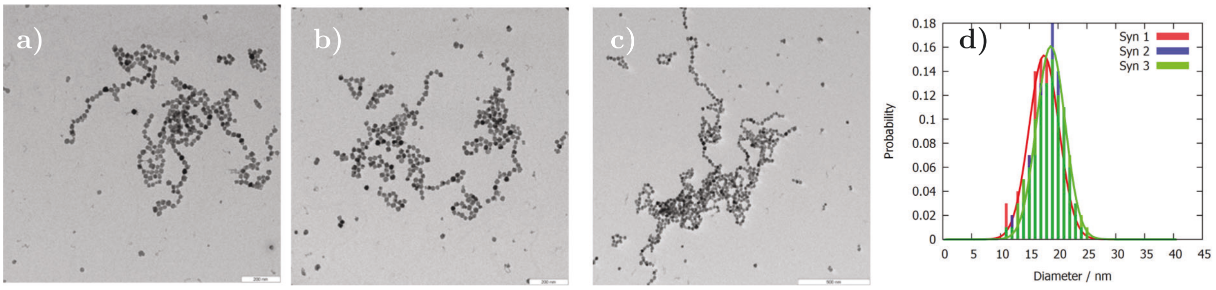

Figure 2: Magnetite nanoparticles synthesized in the presence of PDADMAC at pH 11. TEM images a) to c) are taken from triplicates. Calculated size distributions, d), of at least 200 particles show good reproducibility of the synthesis, in contrast to the XRD results obtained from particles prepared under same conditions. This suggests, that the problems with reproducibility seen in Figure 6.6 can be attributed to problems with the experimental setup, rather then intrinsic problems using alternative polymers. Further this may suggest, that equally Chitosan and JR–400 results suffered from similar problems with the setup.
left

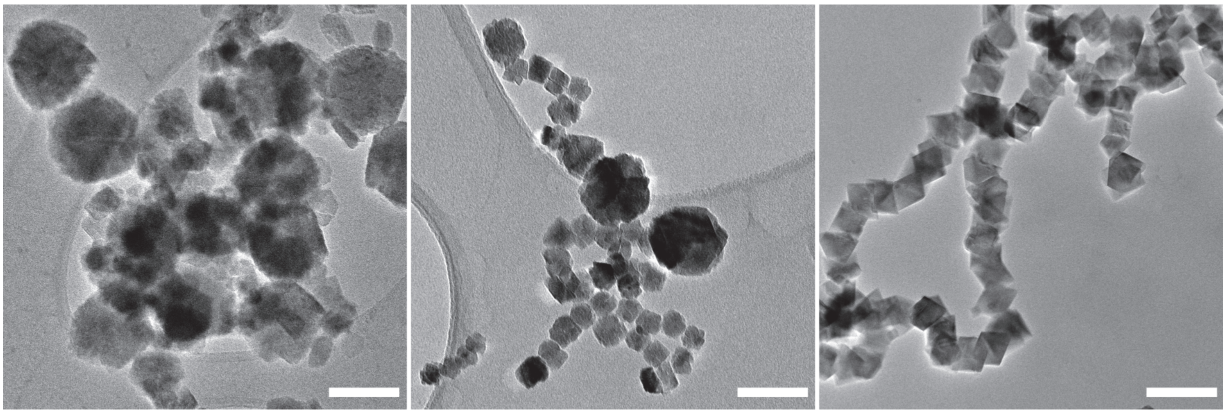

Figure 3: TEM micrograph of magnetite grown in the presence of 0.1 mg mL^{-1} a) JR–400, b) chitosan and c) PDADMAC for 24 h using the adapted synthesis protocol. Scale bar 100 nm.

Preliminary cryo–XANES measurements

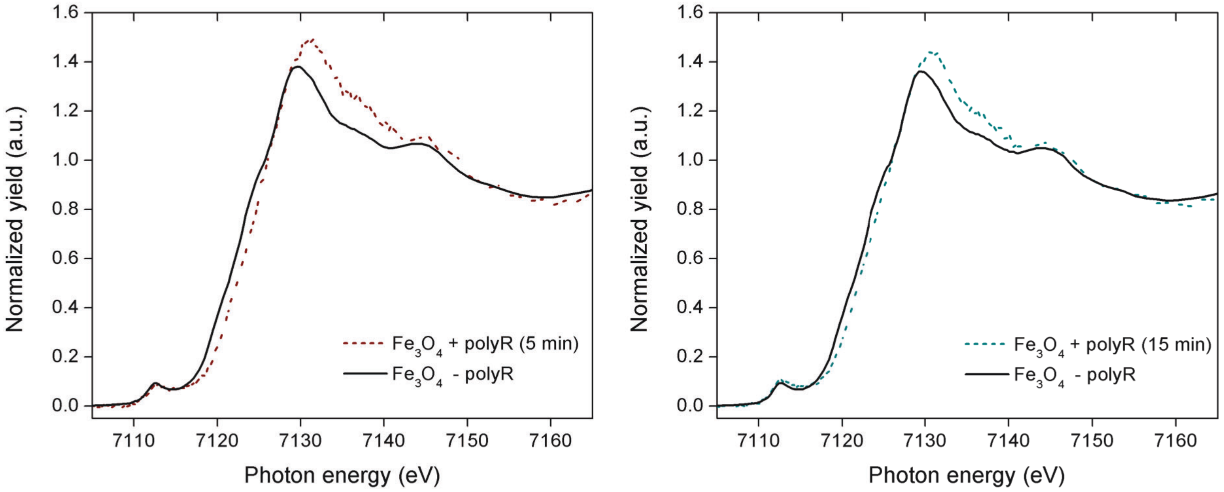

Figure 4: Preliminary cryo–XANES measurements of magnetite co–precipitated in the presence of polyR. Samples were taken 5 min and 15 min into the synthesis. The reference spectrum of magnetite shows a shift in the white line of samples prepared in the presence of polyR indicating a higher oxidation state of the early particles. We thus feel affirmed, that the upcoming cryo–XANES beamtime will unravel the low–density precursor iron phase to be a metastable iron(oxy)hydroxide.

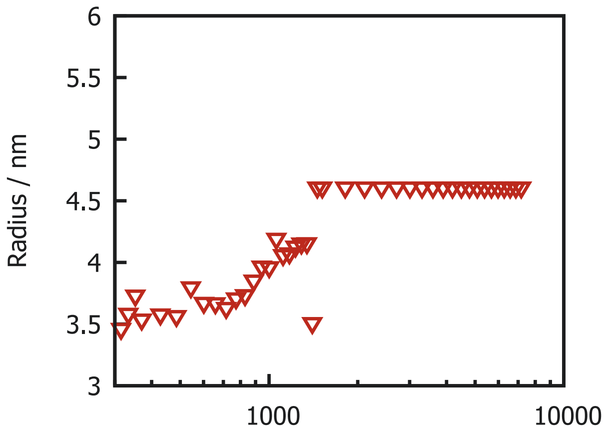

Figure 5: Evolution of gyration radius of precursor particles obtained from analysis *in situ* SAXS data of particles prepared at 15°C. The overall growth rate of NP and precursors seems to be slowed down, so that scattering of precursors is only later dominated by scattering from NP so that their growth can be temporally and structurally resolved.

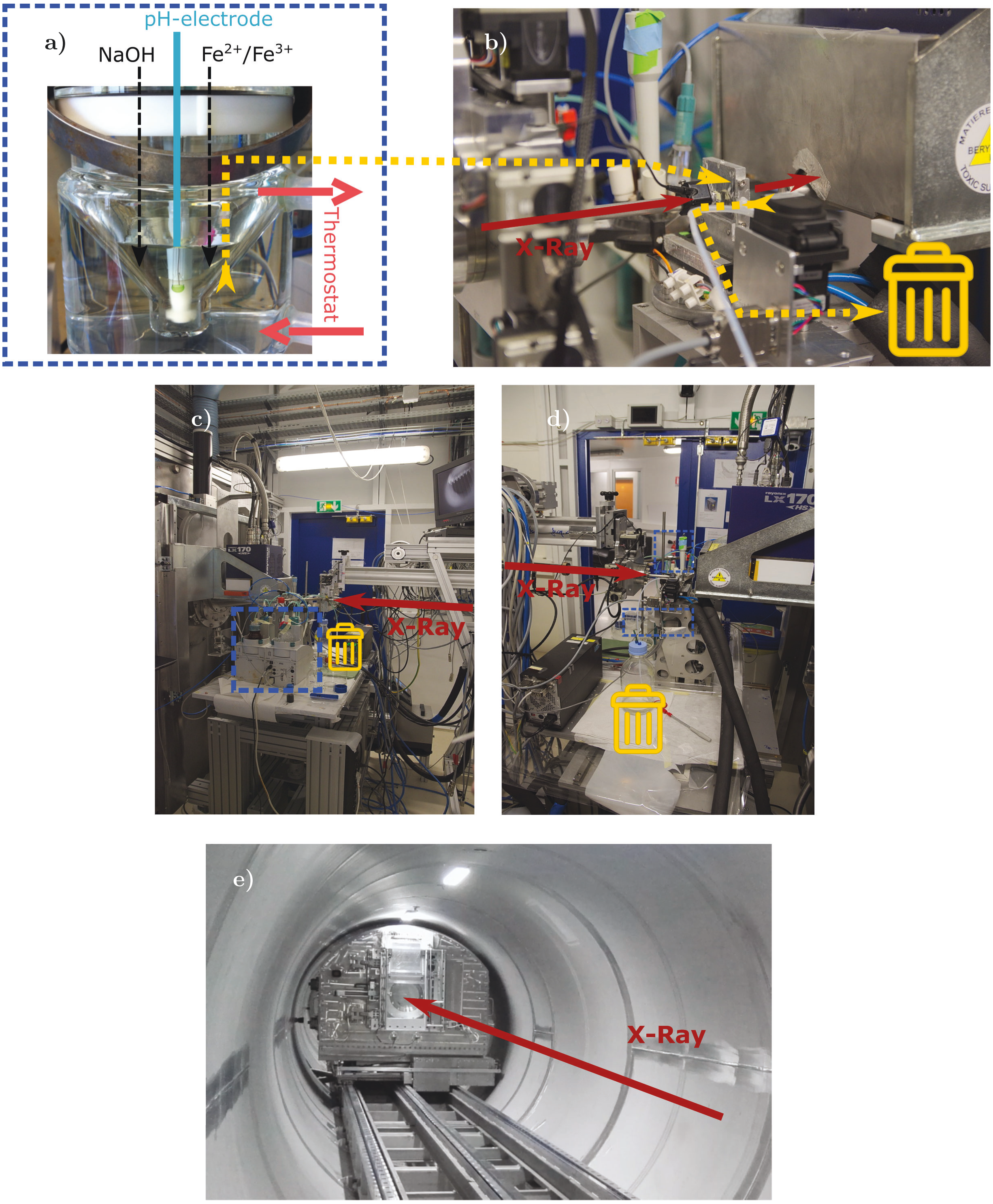

Figure 6: a) Schematic of the setup of the co–precipitation reaction. For the *in situ* SAXS measurments the setup was brought to the ESRF ID02 beamline c) and d). b) Sample were automatically taken from the synthesis using a step–motor peristaltic pump with a stopped flow configuration. The flow inside the capillary was made turbulent using a flow breaker to ensure exchange of liquid. As the detectors at ID02 are placed inside a vacuum tube e) we were able to measure at 3 sample to detector distances.

Equilibrium Constants NP growth

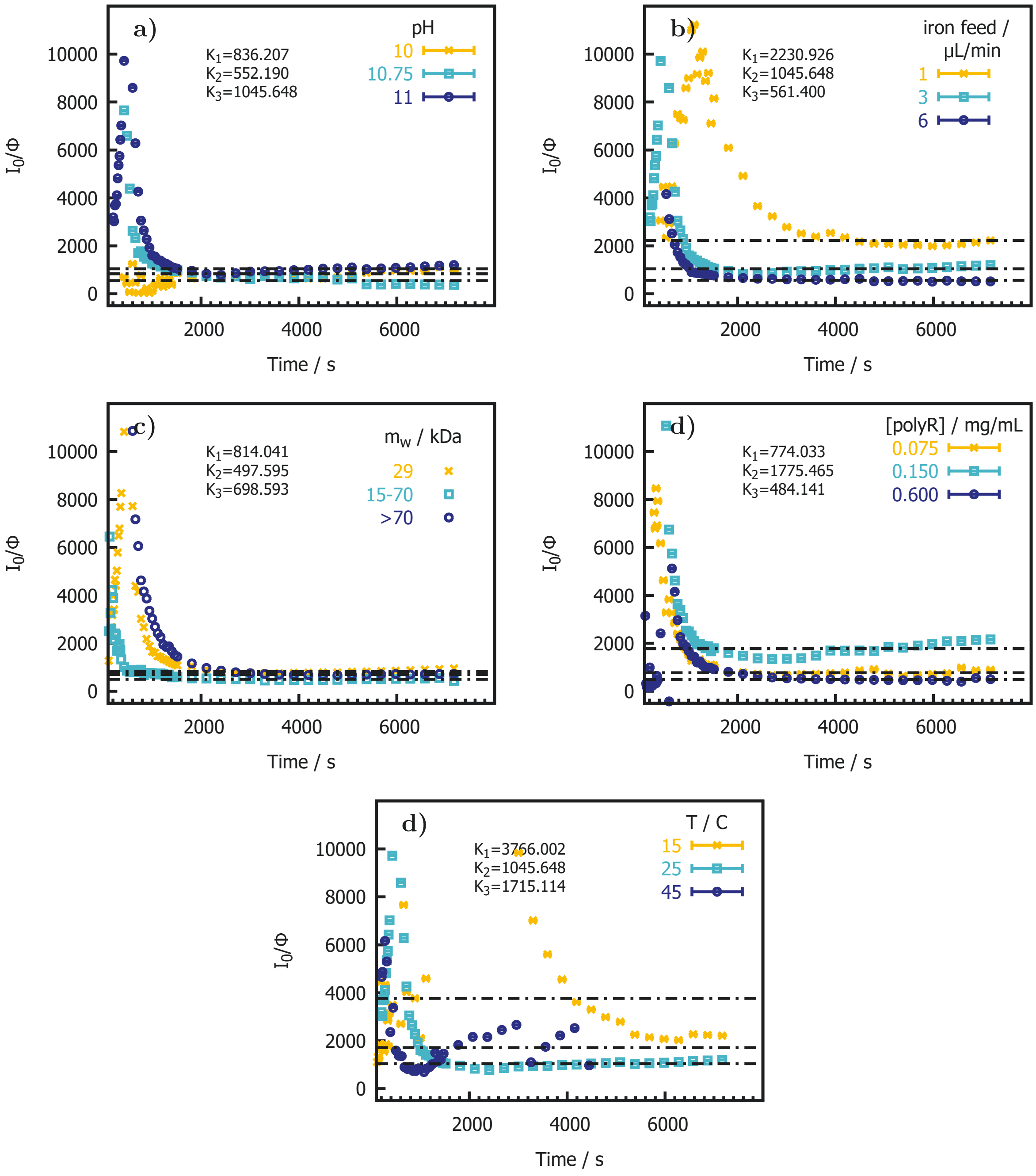

Figure 7: Forward scattering of precursor particles divided by volume fraction of nanoparticles

Fits SAXS data

Table 1: Sample IDs of all synthesis measured during ID02 beamtime MA37

ID	**M_W** [**kDa**]	**c(polyR)** [**mg/mL**]	**pH**	**SDD** [**m**]	**Temperature** [°C]	**Iron Feeding** [$\mathrm{mg\,mL^{-1}}$]
1	15-70	0.3	11	1	25	3
1_2	15-70	0.3	11	1	25	3
2	15-70	0.3	11	6	25	3
3	15-70	0.3	11	30	25	3
5	5-15	0.15	10	6	25	3
6	5-15	0.3	12	6	25	3
7	5-15	0.3	9	6	25	3
8	5-15	0.3	10.75	6	25	3
9	5-15	0.15	11	6	25	3
11	70	0.3	0.3	11	25	3
12	5-15	0.3	10	1	25	3
12_2	5-15	0.3	10	6	25	3
13	29	0.3	11	6	25	3
14	5-15	0.3	12	6	25	3
15	5-15	0.6	10	6	25	3
16	15-70	0.3	11	6	15	3
17	15-70	0.3	11	6	45	3
19	15-70	0.075	11	6	25	3
20	15-70	0.6	11	6	25	3
21	15-70	0.15	11	6	25	3
22	15-70	0.1	11	6	25	1
23	15-70	0.6	11	6	25	6

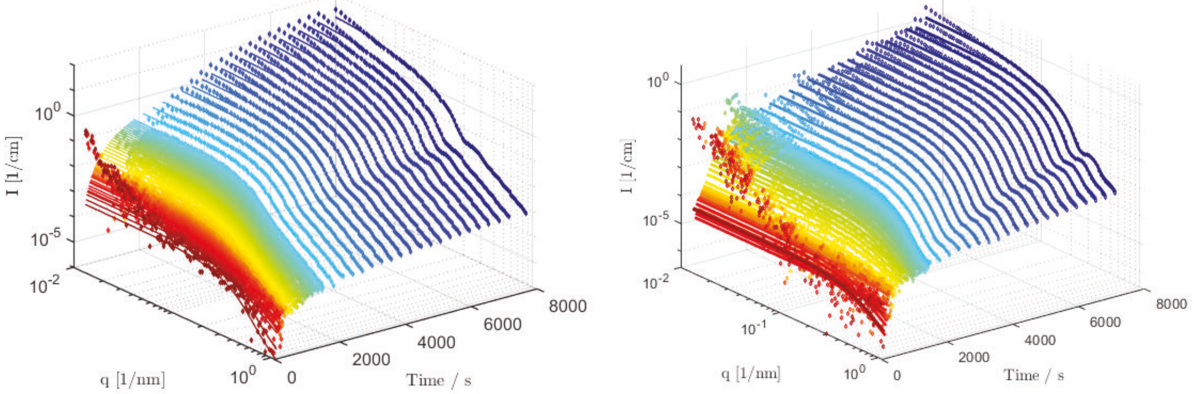

Figure 8: Fits for left sample ID: 2 right sample ID: 5

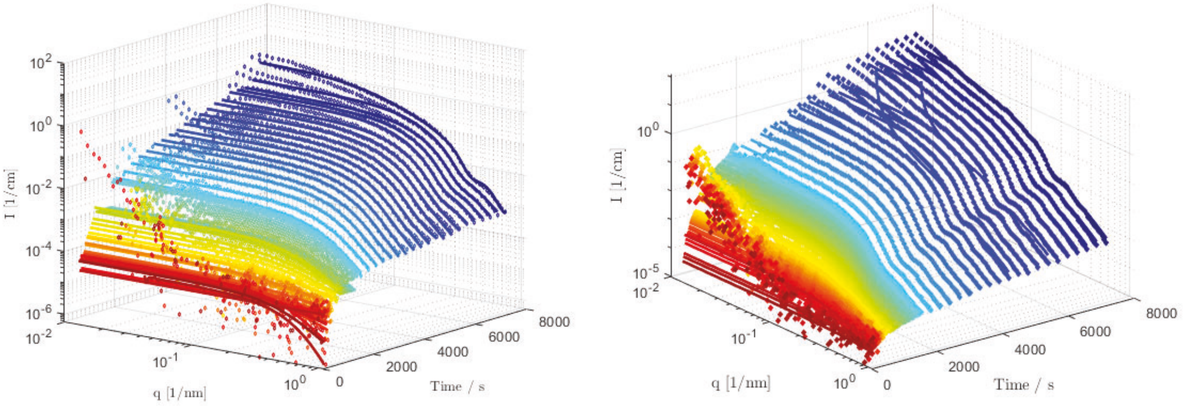

Figure 9: Fits for left sample ID: 7 right sample ID: 8

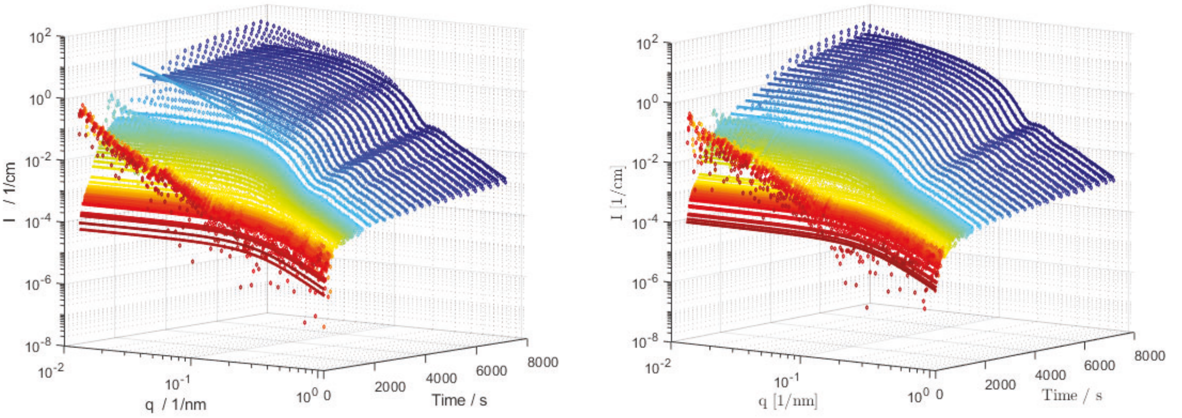

Figure 10: Fits for left sample ID: 9 right sample ID: 11

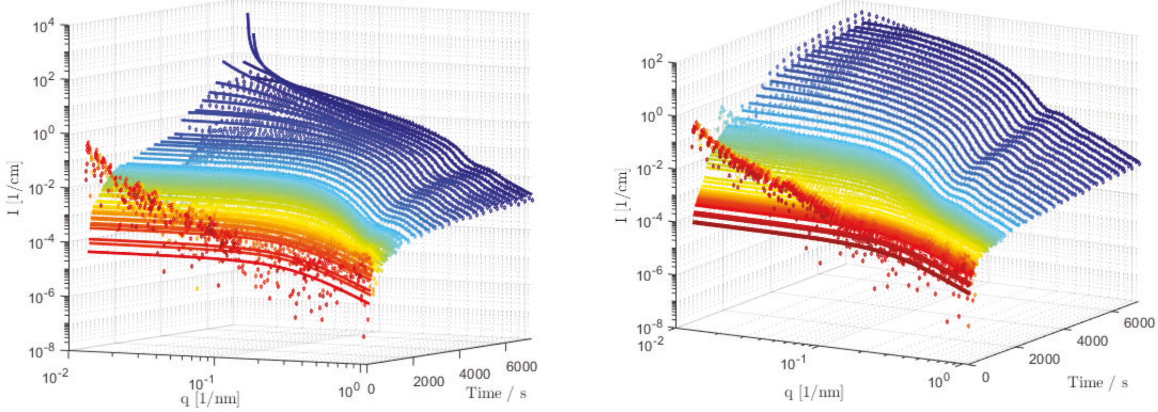

Figure 11: Fits for left sample ID: 12 right sample ID: 13

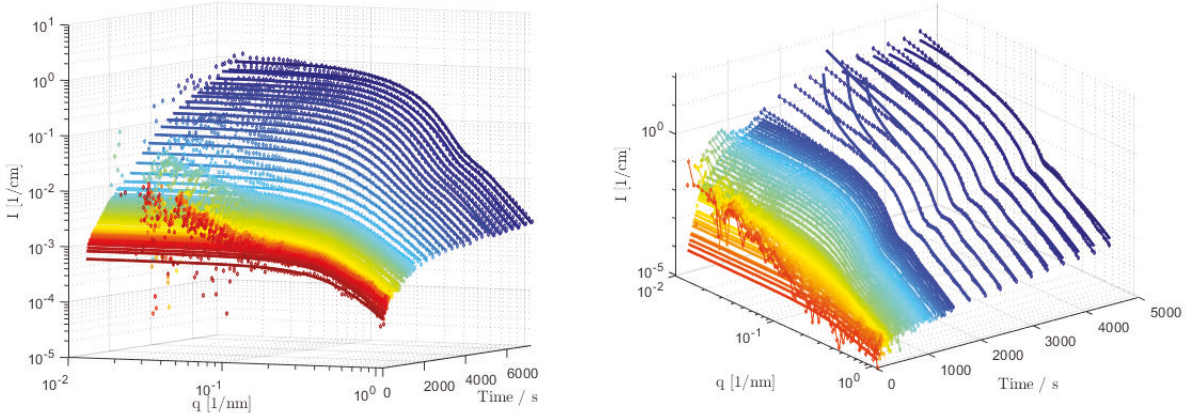

Figure 12: Fits for left sample ID: 16 right sample ID: 17

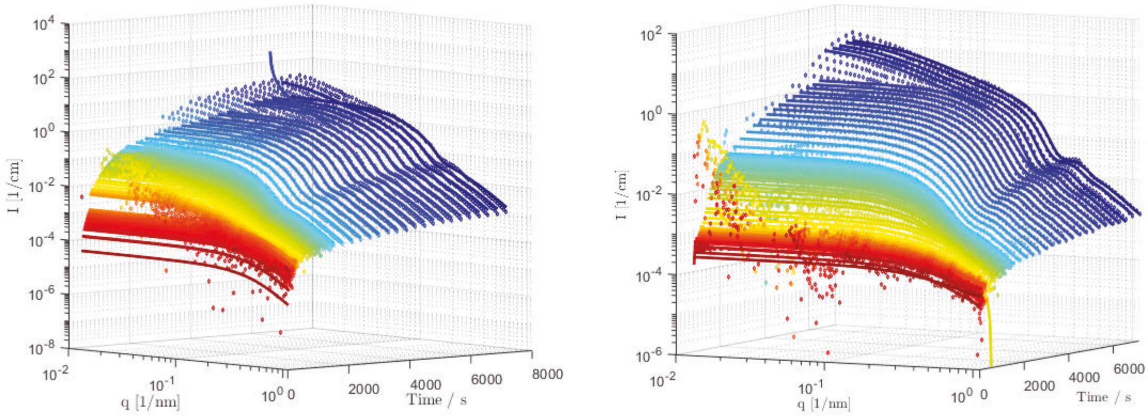

Figure 13: Fits for left sample ID: 19 right sample ID: 20

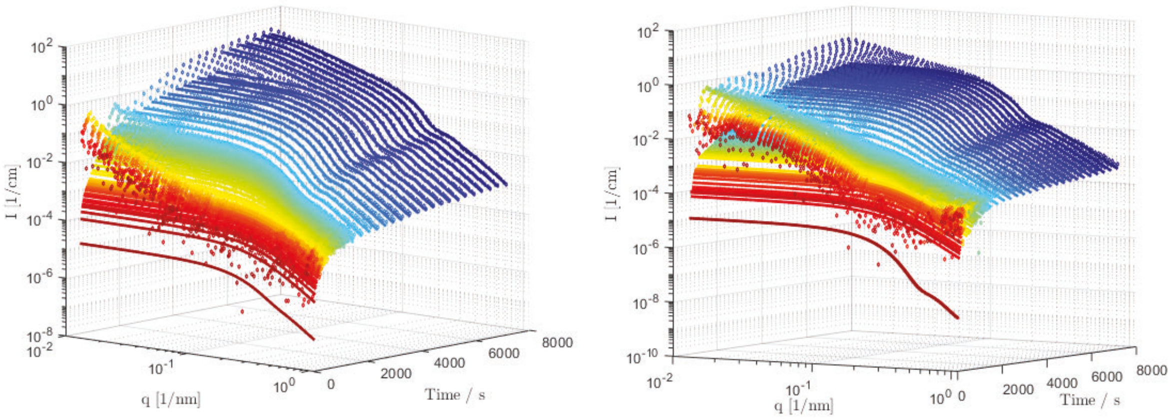

Figure 14: Fits for left sample ID: 21 right sample ID: 22

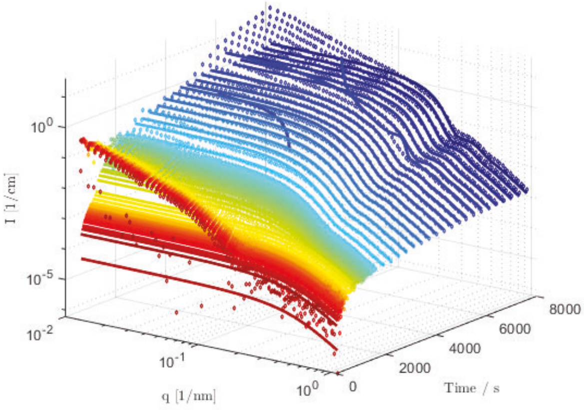

Figure 15: Fits for sample ID: 23

Analytical Scattering Model: SASET SCRIPT

```
%% LuKu generalized coil plus spheres
function [val] = LuKU_coil_20190225(q,a)
%% Parameters
R = a(1);           % average radius cluster [nm]                % default = 17.3; aFixed = 0; lb = 1; ub = 30;
rsd = a(2);         % relative st-dev of radius                  % default = 0.15; lb = 0; ub = 0.21;
dsld = a(3);        % contrast                                   % default = 32.4e-4; aFixed = 1;
scale = a(4);       % forward scattering scaling [1/nm > 1/mm]   % default = 1e6; aFixed = 1;  lb = 0;
IBkg = a(5);        % constant background [1/mm]                 % default = 0; aFixed = 1;
fnp = a(6);         % vol frac                                   % default = 7e-5; aFixed = 0; lb = 0; ub = Inf;
feff = a(7);        % effective hard sphere volume fraction      % default = 0.15; aFixed = 0; lb = 0; ub = 0.67;
rg = a(8);          % gyration radius monomer [nm]               % default = 3.6; aFixed = 1; lb = 0;
i0 = a(9);          % forward scattering fluc [1/mm]             % default = 2e-2; aFixed = 0; lb = 0;
nu = a(10);         % power law flux                             % default = 0.32; aFixed = 1; lb = 0;
d = a(11);          % well width [nm]                            % default = 1.25; aFixed = 0; lb = 0;
e = a(12);          % well depth in k_B T                        % default = 3;  aFixed = 0; lb = 0;

%% Calculation

f = [i0 rg nu 0 1];
gg = generalizedGaussianCoil(q,f);
if ~isreal(gg)
    error('generalizedGaussianCoil has an imaginary part')
end

if (R == 0 || fnp == 0)
    val = gg + IBkg;
```

```
else
    z = 1/rsd^2 - 1;
    alpha = (z+1)./(q*R);

    VpAve = 4*pi/3*R^3*(z+3)*(z+2)/(z+1)^2;
    n = fnp/VpAve;

    G1TildeTerm1 = alpha.^6;
    G1TildeTerm2 = -exp(6*log(alpha)-(z+1)/2*log(1+4./alpha.^2)) .* cos(g(z,alpha,1,2));
    G1TildeTerm3 = (z+1)*(z+2)*alpha.^4;
    G1TildeTerm4 = (z+2)*(z+1).*cos(g(z,alpha,3,2)).*exp(4*log(alpha)-(z+3)/2*log(1+4./alpha.^2));
    G1TildeTerm5 = -2*(z+1).*sin(g(z,alpha,2,2)).*exp(5*log(alpha)-(z+2)/2*log(1+4./alpha.^2));
    G1Tilde = G1TildeTerm1+G1TildeTerm2+G1TildeTerm3+G1TildeTerm4+G1TildeTerm5;
    pq = 8*pi^2*dsld^2*(R/(z+1))^6*G1Tilde;
    if ~isreal(pq)
        error('the Schulz-Zimm sphere form factor has an imaginary part')
    end

    if feff < 0.001
        sqeff = 1;
    else
        lnG1 = -(z+7)*log(alpha)+log(G1Tilde);
        G2Term1 = sin(g(z,alpha,1,1));
        G2Term2 = -(z+1)*cos(g(z,alpha,2,1))./sqrt(1+alpha.^2);
        G2 = G2Term1 + G2Term2;
        lnbetaTilde = log(2) + (z+1)*log(alpha./(1+alpha.^2)) - lnG1;
        beta = exp(lnbetaTilde) .* G2.^2;
%         if ~isreal(beta)
```

```
%      error('the decoupling approximation factor has an imaginary part')
%    end
    sqeff = 1 + real(beta).*(SSquareWell(q, [R feff d e 3])-1);
    if ~isreal(sqeff)
      error('the square well structure factor has an imaginary part')
    end
  end
  val = scale * (n * pq .* sqeff) + gg + IBkg;
end

end

%% Support functions
function val = g(z,alpha,l,c)
  val = (z+l).*atan(c./alpha);
end
```

Eidesstattliche Erklärung

Ich erkläre an Eides statt, dass ich die vorliegende Arbeit selbstständig und nur unter Verwendung der angegebenen Literatur und Hilfsmittel erarbeitet und verfasst habe.

Potsdam, den 02.10.2019

Lucas Kuhrts